

Quantum droplets in a mixture of ^{23}Na and ^{87}Rb Bose-Einstein condensates

GUO, Zhichao

A Thesis Submitted in Partial Fulfilment
of the Requirements for the Degree of
Doctor of Philosophy
in
Physics

The Chinese University of Hong Kong
October 2021

Thesis Assessment Committee

Professor XU, Lei (Chair)

Professor Wang, Dajun (Thesis Supervisor)

Associate Professor Yang, Seng (Committee Member)

Professor Yu, Zhenhua (External Examiner)

Abstract

of thesis entitled:

Quantum droplets in a mixture of ^{23}Na and ^{87}Rb Bose-Einstein condensates

Submitted by GUO, Zhichao

for the degree of Doctor of Philosophy

at The Chinese University of Hong Kong in October 2021

The mean-field theory of Bose-Einstein condensate, as a zero-order approximation, performs well under weaker interaction cases. However, when the interaction increases, we need to introduce the beyond-mean-field correction for further description, i.e. the Lee-Huang-Yang (LHY) correction. This thesis aims to experimentally study a new phase, quantum liquid droplet, formed by a two-component Bose-Einstein condensate; Correspondingly, we investigate the LHY correction, which is essential for liquid droplet formation. With the Feshbach resonance, the interspecies interaction between Na and Rb can be adjusted at will while keeping the intraspecies interaction unchanged. When the inter-species interaction is attractive enough to make the total average energy reach zero or even negative, the mixed condensate sample, instead of mean-field collapsing, stabilizes and forms a new quantum state by virtue of the LHY correction. The experiment observed a smoking-gun self-binding behaviour of the droplet state, i.e. maintaining a finite volume even without any confinement. Further experiments study the phase transition condition of the quantum

liquid droplet to a gaseous phase, which serves as a quantitative characterization of the LHY effect. Moreover, we explain the abnormal expansion velocity of the gaseous sample near-zero mean-field energy region as a complementary study to the liquid phase.

Because of quantum droplets' sensitivity to the inter-particle interactions, we required a precise map of the scattering length as a function of the magnetic field. Therefore, we measured the binding energy accurately by dissociating the Na-Rb Feshbach molecules. Then, fitting by the coupled-channel method, we achieved a highly accurate molecular potential curve. Finally, we obtained a refined map of the scattering length to the magnetic field. This calibration lay a solid foundation for further researches about the mixture of Na and Rb.

摘要

鈉銣超冷混合量子液滴的實驗研究

量子多體系統的平均場理作為描述體系的零階近似在相互作用較弱的態制下表現良好。但是，隨著相互作用的增強，我們就需要引入“超越平均場”的修正來做進一步的描述。本論文旨在實驗研究由鈉和銣組成的雙組分波色-愛因斯坦凝聚形成的新的量子相——量子液滴；同時研究了解釋其所需的超越平均場的修正——也稱為“李黃楊修正”。借住費什巴赫共振，鈉銣的種間相互作用可以隨意調節，同時保持種內相互作用維持不變。當種間相互作用足夠吸引從而使得總的平均能達到零甚至是負值時，混合凝聚體系統並沒有坍縮，而是借住超越平均場的李黃楊效應穩定下來並形成了一種新的量子態——量子液滴。實驗觀察到了液滴態明確的自束縛行為，即在無外界束縛時依然保持有限體積。進一步實驗研究了量子液滴轉變為氣態的相變條件，定量的研究了李黃楊效應產生的影響。並且對於氣態樣品的反常的擴散速度給與解釋，從而揭示了更多的關於李黃楊響應對於凝聚體的影響。

借住對量子液滴的研究，我們對於表征相互作用的散射長度有了更精確的需求。所以，我們實驗通過對於費什巴赫分子的束縛能進行精確測量，從而獲得更加精確的“束縛能-磁場”關係。然後，通過耦合軌道的計算和擬合使得分子勢能曲線更加精確。從而獲得非常精確的“散射長度-磁場”關係。這一部分的研究對於未來進一步研究鈉銣混合體系的其他新奇特性打下了堅實基礎。

Acknowledgement

Two roads diverged in a yellow wood,
And sorry I could not travel both...
I took the one less traveled by,
And that has made all the difference.

— Robert Frost, *The Road Not Taken*

First, I would like to thank Professor Dajun Wang for accepting me to CUHK as a postgraduate student. Without his admission, I could have already been working in the industry for five years and definitely have had no chance to see the fantastic world of physics. Dajun is a detailed-oriented professor. He can help us with any technical detail when we are freshmen in optics, electronics and mechanics. I learnt so much from him, from technique tricks to physics understanding and to the way of thinking and doing. When meeting a problem that no signal after one-day effort, I quote his word that "you cannot optimize zero." and try to change the direction to think. When seeing an unexpected signal, I always ask what he asked: "Is it a technique trick or physics?". Then I make a complete analysis instead of directly debugging instruments. After five years of training, I conclude the spirit as "always be honest to yourself".

Dr. Lintao Li is the first guy I met in the lab. He is proficient in electronics and is a geek who can build any fancy circuit. Without his effort, we could still struggle in fighting with the unstable magnetic field every day. We cooperated for more than four years, and I learned a lot from him, not only electronics but also the way of de-

bugging. He helps me conquer my fear of reading complex schematics and establish my confidence in solving any technical problem. Fan Jia is my close partner. We work together on almost all projects: quantum liquid droplet, Feshbach resonance calibration, detect Feshbach molecules and so on. Without his effort and company, I could not get all the things done. I thank all people working on the mixture experiment, including Shi Yu, Tong Pan, Zerong Huang, Rongzi Zhou and Chun Kit Wong.

Another lab in our group is working on the ground state molecule of Na-Rb. Mingyang Guo and Xin Ye taught me much basic knowledge on AMO physics. Two Junyu (Junyu he and Junyu Lin) taught me knowledge of molecule and optical lattice. It is always fun to talk with Junyu. He shares lots of inspirations with me. Our conversion always tries to imagine and conceive the future of AMO physics, new technology and science and technology as an institution. All though most are only imaginary, I sincerely hope to see them within my lifetime. Besides, I want to thank other members in this lab: Mucan Jin, Guanghua Chen and two new students Zhaopeng Shi and Bo Yang.

We work in the cold atom and molecule group as a family. I hope everyone finds their unique path and have a happy journey.

I want to thank our collaborators for their kindness and generous help. Thanks to Prof. Xiaoling Cui and Dr. Yinfeng Ma for their patient help on the theoretical support of our experiments. Also, many thanks to Prof. Jeremy Hutson for his general help with using MOLSCAT for re-calibrating the Feshbach resonance.

Besides working, I made many good friends. Their different backgrounds and insights open me to a new realm of world. They introduce me to geography, anthropology, political science, sociology and so on so forth. These different perspectives allow me to re-examine the position of my research in entire human history, which made me realize my insignificance and the greatness of humankind as a whole.

I learned from the five-year PhD career that *research* is an attitude to life. The

biggest challenge we face is fear, especially the fear of the unknown. At every moment, we are faced with choices. Whether it is a quiz or a career choice, we all need to give our own attitude. The so-called research attitude, in my opinion, is to choose boldly, then record faithfully and finally review and summarize. Such a cycle can help anyone face any problem and let you know yourself further. From a human point of view, it allows humans to further their understanding of themselves and nature. This is also the ultimate goal of mankind.

In addition to the attitude and methodology mentioned above, a qualified PhD should consciously discern which is important and which is not in a specific field. From a branch of the field to the entire discipline, this process marks the growth of a scholar. I hope this thesis can reflect my taste on this tiny branch – quantum droplet. Furthermore, I am still far from clear about the taste of Physics, Science, and Humankind. These become goals for me in the future of my life.

Dedicated to those who risked their lives fighting against COVID-19

Contents

Contents	viii
List of Figures	xii
List of Tables	xv
1 Introduction	1
1.1 Why quantum liquid droplets?	2
1.2 Quantum depletion and LHY correction	6
1.3 Thesis Outline	8
2 Theory	10
2.1 Quantum scattering: a short reminder	11
2.2 Quantum droplet	14
2.2.1 Dilute Bose system: Pseudo-Hamiltonian and Bogoliubov transformation	15
2.2.2 Ground state and LHY correction	20
2.2.3 Quantum Depletion and Mechanism of LHY Droplet	22
2.2.4 Mean-field theory of Double BEC	22
2.2.5 Ground state and LHY correction of double species BEC	25

3 Apparatus	29
3.1 Overview: Na-Rb machine I	30
3.1.1 Producing Na-Rb Bose-Einstein condensate mixtures	30
3.1.2 Producing Na-Rb Feshbach molecules	35
3.2 Image system upgrades	36
3.2.1 High resolution image system	37
3.2.2 High magnetic field absorption image	41
3.2.3 Atomic number calibration	45
3.3 CAMIMA: a multi-camera and image process platform	48
3.3.1 licensing, versions and updates	49
3.3.2 Using the software: a basic guide	50
3.3.3 Vision and outlooks	57
3.4 Fast magnetic field control	58
3.5 Other Technical Issues	61
3.5.1 Magnetic field gradient compensation	61
3.5.2 Microwave full-wave loop antenna	63
4 Precision characterisation of a Feshbach Resonance	73
4.1 Overview	73
4.2 Na-Rb Feshbach resonance at 347.64 G	78
4.2.1 Measurement of the Na-Rb Feshbach molecule binding energy	80
4.2.2 Coupled-channel modeling and FR parameters	83
4.3 Na-Rb, Na-Na and Rb-Rb scattering length summary	91
4.3.1 Na-Rb scattering length for different spin combination	93
4.3.2 Na-Na and Rb-Rb scattering length	100
5 Quantum droplet of hetero-nuclear Bose mixture	103
5.1 Quantum droplet with finite size	104

5.2	Variational calculation	107
5.2.1	Single species BEC in harmonic trap	109
5.2.2	Double BEC in harmonic trap with near zero-MF interaction	111
5.2.3	How magnetic field gradient affect droplet	113
5.3	extended GPE solution	116
5.3.1	Derivation of GPE for single species BEC	120
5.3.2	Derivation of extended GPE for double species	121
5.3.3	eGPE for GPELAB with Minardi approximation	123
5.4	Na-Rb Hetero-nuclear quantum droplet	125
5.4.1	Experiment method and time sequence	127
5.4.2	observing non-expansion signal	128
5.4.3	Characterization of liquid-gas phase transition	131
5.5	Lee-Huang-Yang gas	132
5.5.1	Expansion of gas phase sample and Release energy	133
5.6	Mode matching when producing droplet sample	136
5.6.1	In-trap vs. free-space sample	136
5.6.2	producing weak bound droplet by quenching B-field	137
5.7	producing Feshbach molecule from droplet	139
6	Conclusion and Outlooks	140
6.1	Conclusion	140
6.2	Thesis Overview	141
6.3	Outlooks	150
A	Mechanics and electronics schematic	153
A.1	Pair-Coil current driver with differential current pump	154
A.1.1	Simulation by Tina-TI	155
A.2	Up-Down Image system	159

B Camera comparison and absorption image SNR analysis	160
B.1 Absorption SNR analysis	160
Bibliography	163

List of Figures

1.1	Comparison between classical and quantum liquid droplet	4
2.1	Low energy scattering of finite range potential	13
2.2	This plot shows the dissipation relationship for attractive Bose system.	19
2.3	This plot shows the dissipation relationship for attractive Bose system.	20
2.4	Droplet density as a function of δg	28
3.1	Front and top view of overall Na-Rb machine	31
3.2	Temperature-current relationship of dispenser (Image from alfavakuo)	32
3.3	Na and Rb samples in 946 and 1070 nm ODT (image from [Li, 2021]) .	34
3.4	3x image system simulation by Zemax	38
3.5	New compact imaging system	39
3.6	Image resolution test of 15x image system	40
3.7	SNR of absorption image as a function of OD	42
3.8	image scheme for Na(Rb) $ F = 1, m_F = 1\rangle$ state under 350 G magnetic field	43
3.9	Partial pumping portion as function of pump duration	44
3.10	β -calibration of Rb 15x absorption image	47
3.11	CAMIMA main panel	50
3.12	CamTree: show all available cameras for acquiring images	52
3.13	CAMSET: a module of CAMIMA used to control and set cameras . .	53

3.14	VUIMA: a module of CAMIMA used to preview image	54
3.15	FITSET: a module of CAMIMA used to set arbitrary fitting function	56
3.16	Fast coil holder	59
3.17	Fast coil, main coil and environment	60
3.18	Method of compensating the magnetic field gradient	63
3.19	Method of searching the compensation point	64
3.20	Magnetic field spatial distribution at vertical direction after compensation	65
3.21	Electromagnetic field of a dipole antenna	66
3.22	Full loop antenna and Q-section for impedance matching	67
3.23	Impedance of full-wave loop antenna with different shapes	69
3.24	Test method of the return loss of the antenna	70
3.25	Test of the return loss by changing the lengths of the Q-sections	71
3.26	Test Rabi oscillation of Na $ 1, 1\rangle$ to $ 2, 2\rangle$ under 350 Gauss magnetic field	72
4.1	One example of loss spectrum of Feshbach resonance.	76
4.2	Association spectrum of Na and Rb near 347.64 G. (Image from [Wang et al., 2015a])	77
4.3	Time sequence for measuring binding energy of Feshbach molecules	79
4.4	Feshbach molecule dissociation spectrum	82
4.5	Binding energy of $^{23}\text{Na}^{87}\text{Rb}$ Feshbach molecules at 347.64 G	84
4.6	Scattering length as function of magnetic field	92
4.7	Loss spectroscopy of Feshbach resonance with different spin combinations	94
4.8	Scattering lengths of $\text{Na} 1\rangle + \text{Rb} 1\rangle$ and $\text{Na} -1\rangle + \text{Rb} -1\rangle$ elastic channels	95
4.9	Scattering lengths of $M_F = 1$ channels	97
4.10	Scattering lengths of $M_F = 0$ channels	98
4.11	Zeeman energy for $M_F = 1$ and $M_F = 0$ channels	99

4.12	Scattering lengths of $M_F = -1$ channels	100
4.13	$\text{Na} 1, 1\rangle + \text{Na} 1, 1\rangle$ scattering length as a function of magnetic field	101
5.1	Droplet density distribution and edge effect	106
5.2	Convergence test of $f(\gamma, x, y)$	119
5.3	Compare the numerical solution and Minardi's approximation of $f(\gamma, x, y)$	120
5.4	Creation and detection of Na-Rb mixtures for investigating LHY effects	126
5.5	Time sequence for producing quantum droplet	128
5.6	Evolution of the Na-Rb droplet in free space	130
5.7	Critical atom numbers for the liquid-to-gas phase transition as a function of $\tilde{\delta}g$	132
5.8	Measurement of the release energy as a function of $\tilde{\delta}g$	134
5.9	Droplet formation by directly releasing the trapped sample.	136
5.10	Producing long-lived droplet by magnetic field quench	138
6.1	ToF of Na-Rb BEC mixture under high magnetic field	143
6.2	Na-Rb BEC mixture with various inter-species interaction	144
6.3	Try to detect droplet signal by low field image	145
6.4	Two image schemes for Na(Rb) $ F = 1, m_F = 1\rangle$ state under 350 G	147
6.5	non-cycling absorption image for droplet signal	148
6.6	Droplet signal of number imbalanced case	149

List of Tables

3.1	Summary of image calibration	48
3.2	Parameter table of main coil and fast coil	60
4.1	Parameters of the two low-field <i>s</i> -wave Feshbach resonances for the entrance channel $\text{Na} 1, 1\rangle + \text{Rb} 1, 1\rangle$	90
4.2	Summary table of Na-Rb Feshbach resonances with different spin combinations	96
B.1	Cameras parameter table	162

Chapter 1

Introduction

What is a stupid question? If there is only one answer to the question instead of other possibilities, it is a stupid question. [Cheung, 1988]

— Steven N. S. Cheung
Way of thinking (1984)

The world is made up of various substances, and even the same substance can be in different *phases*. Besides finding new particles and materials, discovering new phases of matter is also an essential subject of physics. When discovered phases of matter accumulating, how to classify, explain and understand them from the perspective of microscopic theory gradually becomes the core topic of physics. This thesis will introduce a new quantum phase of ultracold atoms, i.e. the quantum liquid droplet. Correspondingly, the microscopic theory about the beyond mean-field effect, Lee-Huang-Yang (LHY) correction[Lee et al., 1957], will be discussed detailedly in the latter chapters. This chapter will introduce the history of the topic developed in recent years and its influence on other fields. I try to offer readers a broader picture for a better understanding of quantum liquid droplet.

This chapter is arranged as follows: section 1.1 introduces our research goal, the quantum droplet. By introducing some background knowledge and researches from

related fields, I try to discuss why we study the Na-Rb BEC-mixture droplet. Section 1.2 will discuss the core concepts of LHY correction and its history, as a precursor of Chapter 2. Finally, section 1.3 offers the arrangement of the whole thesis.

1.1 Why quantum liquid droplets?

Before answering the question on the title, i.e. about the *quantum* liquid droplet, we first draw some attention to the *classical* liquid-gas phase transition. As shown in Fig. 1.1, a classical gas can be regarded as a bunch of interacting particles. Typically, we use the Van der Waals interaction as a good approximation, i.e. a hard-core (repulsion) plus an attractive long-range potential. By adding this inter-particle interaction to the equation of state, we get the famous Van der Waals equation:

$$(P + a \frac{n^2}{V^2})(V - bn) = nRT \quad (1.1)$$

where the “ b ” factor represents the hardcore size, since the effective volume of sample is enlarged, and “ a ” shows the attractive interaction between particles which reduces the pressure of the sample. This equation implies the liquid-gas phase transition when the temperature is lowering down to a specific $T_C = \frac{8a}{27Rb}$. The detailed analysis could be found in the textbook [Cowan, 2005]. So, here we only focus on the physics picture. For a liquid phase sample, as shown in Fig. 1.1 right-top panel, the particles are squeezed to their hard-cores touching to each other. This features the incompressibility of a liquid sample. The kinetic energy of particles maintain their mobility, and due to easily exchange of particle position, we still have a fluid instead of a solid phase. In another perspective, the attractive range of particles overlapping with each other indicates a strong correlation. One particle could affect many other particles. We call this a long-range interaction system, which is typically hard to tackle. So, even with full knowledge of its microscopic equation, sometimes the behaviour of liquid can

still amaze us, such as Non-Newtonian fluid or liquid crystal.

Then, a question arises naturally for cold atom physicists: what about a quantum system? Is there any liquid phase for a Bose-Einstein condensate? A positive answer is made by Petrov in 2015 [Petrov, 2015]. For a dilute ultracold BEC mixture, we do have a liquid phase. However, this kind of liquid is dramatically different from the classical one. First, it is a zero-temperature sample, which means the thermal fluctuation is suppressed. Second, the sample is still dilute with an interparticle distance larger than 100 nm (interacting range typical around several nm). This indicates the system should be still in a weak-interacting case. Finally, quantum fluctuation shows its essential role. However, instead of serving as a driven force for mobility, the quantum fluctuation cures the sample's collapse or implosion. To study this sample, we could understand more profound the beyond mean-field correction of this many-body system.

As a new field in ultracold atoms, quantum liquid droplets originated from the deep understanding of the beyond mean-field theory of Bose-Einstein condensate (BEC) and from an innovative and careful extrapolation of textbook theory. In the past 25 years discovery of ultracold gases, mean-field theory (MF theory), as the zero-order solution of a many-body system, dominates the explanation of most phenomena. Especially for Bose-Einstein condensate, it explains plenty of interesting experiment observations, including the state of the equation for in-trap sample, excitation mode, dark soliton, bright solution, BEC collapse and so on. This zero-order approximation considers the condensates as a single wave-function Ψ , which is based on the observation that most atoms share the same ground state, i.e. the $k = 0$ state (for uniform case). However, particles from the condensate could be excited to a finite momentum state due to the interaction between particles. From the microscopic theory of condensate, these particles with $k > 0$ have a fraction of order of $\sqrt{na^3}$ compared to the condensate part, which occupies a tiny portion when the interaction

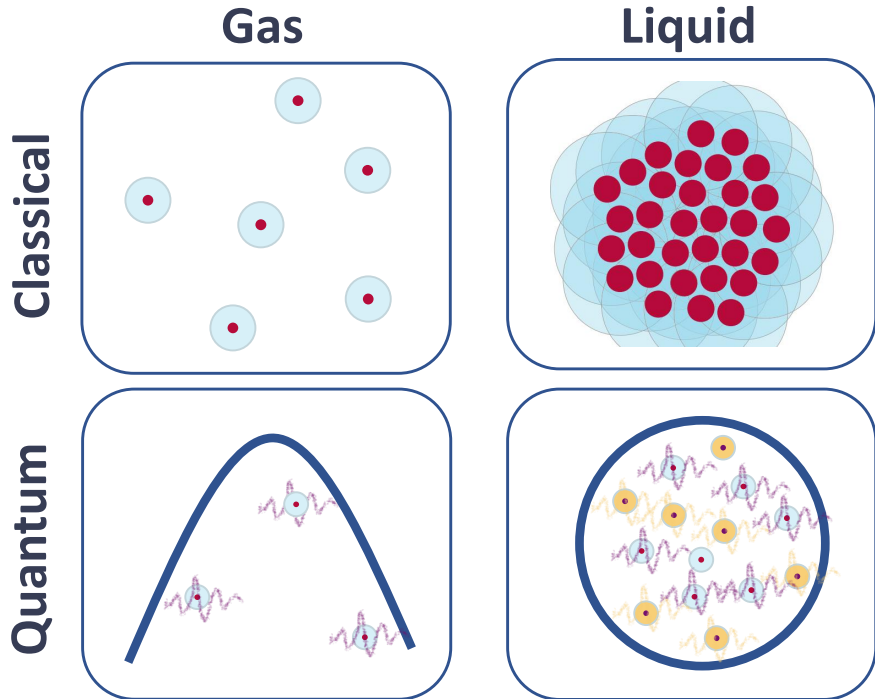


Figure 1.1: Classical and quantum Liquid-gas phase transition. The upper panel shows a classical liquid-gas phase transition, explained by the famous Van der Waals equation. With this theory, particles interact with short-range hardcore (red solid part) and long-range attraction (light-blue outer). When the temperature lowers to the critical temperature, the sample undergoes a phase transition to be a liquid. As shown in the upper-right block, particles stay close to each other with inter-particle distance around the size of its hardcore. Meanwhile, their long-range parts overlap, showing a strongly correlated feature. For the lower panel, we draw the quantum liquid-gas phase transition for a BEC mixture sample. The thick blue line represents the shared wave function for the condensate part. The particle with a de-Broglie wave-packet represents the quantum depletion due to interaction excitation from the condensate. The right-bottom one shows the BEC mixture liquid droplet, which is the main topic of this thesis.

is weak. Thus, we call it quantum depletion. This tiny portion brings only a tiny correction to its ground-state energy; so, people typically ignore its effect in most cases. However, things get incredibly different in the quantum liquid droplet; here, quantum depletion plays a vital role because the depletion part contributes a competitive energy scale to the mean-field energy.

Proposed by Petrov in 2015 [Petrov, 2015], a BEC mixture with overall negative mean-field energy could survive from collapsing and form a quantum droplet. Surprisingly, this theory was first used to explain the self-bound behaviour in the dipolar gas [Ferrier-Barbut et al., 2016b; Chomaz et al., 2016]. Then in 2018, Leticia group [Cabrera et al., 2018] discovered the first double BEC droplet in a spin mixture of ^{39}K . These two distinctive systems are related to the same theoretical explanation, showing the ubiquity that how important role for the LHY correction in ultracold atoms. For both cases, the mean-field energy approaches zero and is tuned by a Feshbach resonance for an inter-species s -wave contact interaction. Meanwhile, the LHY correction remains a positive value and grows even faster than the mean-field one when the density of the sample increasing. So, it cures the mean-field collapse. The difference between a dipolar droplet and a mixture BEC droplet is the inter-particle interaction type: for dipolar case, the interaction is anisotropic, which renders an anisotropic sample as well; however, for the BEC mixture case, thanks to the isotropic interaction, the sample shows a perfect spherical shape.

As mentioned before, Petrov's theory was first used to the dipolar droplet [Ferrier-Barbut et al., 2016b; Chomaz et al., 2016], which is made of magnetic atoms with anisotropic interaction. Then in 2018, two groups [Cabrera et al., 2018; Semeghini et al., 2018] produced the double BEC droplet exactly matching Petrov's original proposal. Latter, many works sprung up, in both experiment and theory. Leticia's group produce the droplet in a wave-guide [Cheiney et al., 2018], in which they study the bright soliton to the droplet phase transition. From the low-dimension

point of view, many theoretical proposals are developing, including [Petrov and Astrakharchik, 2016; Ilg et al., 2018; Cui and Ma, 2021]. In another point of view, i.e. the gas phase sample with near-zero mean-field energy, theory [Jørgensen et al., 2018], and experiment [Skov et al., 2021] study the changing of monopole mode of an LHY gas.

The initial purpose of our research was to make a heteronuclear droplet. With a rough calculation, we estimate its lifetime could reach about 100 ms, enabling us to do further research such as its excitation spectrum and the self evaporation. However, later we find the lifetime of the sample limited to 10 ms level. We attribute this to the large three-body loss between two species. Then, we have to turn our research goal to study the LHY effects in a double BEC of ^{23}Na and ^{87}Rb atoms in two different ways. First, we build the heteronuclear quantum liquid droplet in free space with more than 10^4 atoms when the interspecies Na-Rb scattering length is tuned into the mean-field collapse regime. Under optimized conditions, a low-number-density droplet with a lifetime exceeding the observation time is observed. We also investigate the liquid-to-gas phase transition and obtain the critical atom numbers at the phase boundary. Second, we measure the release energies of two types of gas-phase mixtures, the pure in-trap gas and the gas formed after a droplet crosses the liquid-to-gas transition, and observe their opposite dependence on the interaction strength. With calculations based on extended Gross-Pitaevskii equations (eGPEs), our results confirm the crucial contribution of E_{LHY} and its effects in stabilizing the heteronuclear double BEC far into the mean-field collapse region.

1.2 Quantum depletion and LHY correction

Back to the motivation of studying quantum droplets, the essential ingredient is the beyond-mean-field effect in a Bose condensate, i.e. the Lee-Huang-Yang (LHY) cor-

rection. LHY correction was first introduced by Lee, Huang and Yang in 1957 [Lee et al., 1957], as the first-order correction of the ground state of Bose-Einstein condensate. However, due to its mighty contribution, we typically can ignore it. However, when the zero-order mean-field energy is approaching zero, which means the LHY correction could compare to the MF energy or even dominant the sample, we need to treat it more seriously. This section introduces the quantum depletion and LHY correction as a precursor for the next chapter, which discusses the complete theory for the quantum droplet.

Let us consider a Bose-Einstein condensate, with its Hamiltonian as

$$H = \sum_k \epsilon_k \hat{a}_k^\dagger \hat{a}_k + \frac{g}{2V} \sum_{\{k_i\}} \hat{a}_{k_1}^\dagger \hat{a}_{k_2}^\dagger \hat{a}_{k_3} \hat{a}_{k_4} \quad (1.2)$$

By separating the condensate part and quantum fluctuation part, i.e. considering a_0 as \sqrt{N} and write it away from other creation operators (with $k > 0$), we have

$$\begin{aligned} H = & \frac{gN^2}{2V} + \sum_{k \neq 0} (\epsilon_k + gn_0) \hat{a}_k^\dagger \hat{a}_k + \frac{gN}{2V} \sum_{k \neq 0} (\hat{a}_k^\dagger \hat{a}_{-k}^\dagger + \hat{a}_k \hat{a}_{-k}) \\ & + \frac{g\sqrt{N}}{2V} \sum_{k_1+k_2+k_3=0} (\hat{a}_{k_1}^\dagger \hat{a}_{k_2}^\dagger \hat{a}_{k_3} + \hat{a}_{k_1}^\dagger \hat{a}_{k_2} \hat{a}_{k_3}) + \frac{g}{2V} \sum_{k_i \neq 0} \hat{a}_{k_1}^\dagger \hat{a}_{k_2}^\dagger \hat{a}_{k_3} \hat{a}_{k_4} \end{aligned} \quad (1.3)$$

Ignore the higher order parts and do the Bogoliubov transition, we can get the diagonalized Hamiltonian as

$$\begin{aligned} H \simeq & \frac{gN^2}{2V} - \frac{1}{2} \sum_{k \neq 0} \left(\epsilon_k + \frac{gN}{V} - E_k \right) + \sum_{k \neq 0} E_k \hat{a}_k^\dagger \hat{a}_k \\ E_k = & \sqrt{\epsilon_k \left(\epsilon_k + \frac{2gN}{V} \right)} = \sqrt{\frac{\hbar^2 k^2}{2m} \left(\frac{\hbar^2 k^2}{2m} + \frac{2gN}{V} \right)} \end{aligned} \quad (1.4)$$

The first part shows the energy shift (MF shift) for the condensate part. Second part

shows summation of the energy of all particles with $k > 0$, i.e. the quantum depletion. Third part shows the excitation spectrum of the sample and E_k offers the dispersion of the sample. Now, we only consider the ground state properties, i.e. only consider the first two terms of the Hamiltonian. The fraction of depleted particle is

$$\frac{n_{dp}}{n} = \frac{8}{3\sqrt{\pi}} \sqrt{na_S^3} \quad (1.5)$$

where, we can directly read that with increasing of na_S^3 , more particles get out of the condensate. Meanwhile, these particles will contribute the LHY correction to ground state energy, i.e.

$$\frac{E_{GS}^R}{V} = \frac{gn^2}{2} \left(1 + \frac{128}{15\pi^{1/2}} (na^3)^{1/2} \right) \quad (1.6)$$

where $a = |a_S|$. We can find the LHY correction is small when density is low and only get important when $na^3 \sim 1$. These correction has been experimentally verified in strongly interacting Bose System [Navon et al., 2011]. Thus, we find that this correction beyond mean-field theory increases the energy and increases “hot” particles. Moreover, considering the excitation spectrum for $g < 0$, we can explain that the high energy excitation (short-wave) cure the unstable system of long-wave-instability, which gives the formation of LHY droplet [Petrov, 2015].

1.3 Thesis Outline

Chapter 2 will discuss two fundamental conceptions: quantum scattering and the microscopic theory of a mixture of Bose condensate, which we will revisit many times in the following chapters. Chapter 3 will introduce the main upgrades of apparatus for the droplet experiment. Chapter 4 aims at achieving a precision mapping between scattering length and magnetic field, which is realized by a binding energy measurement of Feshbach molecules. After being armed with this accurate information of

interaction, we detailed demonstrate the production of a hetero-nuclear droplet in Chapter 5. Finally, we summarize the thesis with some outlooks for future directions.

End of chapter.

Chapter 2

Theory

Law of physicists II:

Without theorists, experimentalists tend to falter. [Lee, 1992]

— T. D. Lee

History of the weak interactions (1987)

This chapter mainly introduces the theory of the quantum droplet. Before that, we first briefly review the quantum scattering theory as the basis for theory of BEC and droplet. Also the scattering theory serves as basis for understanding the couple channel calculation in Chap. 4, where we fit the binding energy of the Feshbach molecule to calibrate Na-Rb molecular potential. We note here that the scattering properties play an essential role in understanding the behaviour of an ultracold sample. The second part describes the microscopic theory for two-species BEC and analytically derives its LHY correction. Then, we demonstrate the theory of droplets made of the dual-species BEC. Latter in the Chap. 5, we will implement both variational calculation and GPE simulation for comparing to the experiment.

2.1 Quantum scattering: a short reminder

This section introduces the scattering theoretical basis of partial wave analysis as a brief reminder. In the cold atom system, due to the dilute property of the system, we only consider the two-body elastic scattering. Elastic collisions dominate many cold atom processes, including evaporative cooling, the interacting BEC, etc. Because of the low scattering energy scale of the cold atom system, we use the partial wave method and only consider the lowest partial waves, s -, p -, etc. Especially for BEC systems with interactions, s -wave is sufficient to retrieve all the elastic scattering information. This leads to the use of Pseudo-potential with the same s -wave scattering length to replace the real complex scattering potential, which will be further introduced in Sec. 2.2.

The partial-wave method solves the stationary Schrodinger equation by separating the wave function into the different partial waves, labelled by s -, p - and so on. The Hamiltonian of the system is

$$\left(-\frac{\hbar^2}{2m} \nabla^2 + \hat{V}(r) \right) \psi_k(r, \theta, \phi) = \psi_k(r, \theta, \phi) \quad (2.1)$$

separating the state into radial and angular parts

$$\psi_k(r, \theta, \phi) = R_l(k.r) Y_{lm}(\theta, \phi) \quad (2.2)$$

and then the radial part equation

$$\left(\frac{d^2}{dr^2} + \frac{2}{r} \frac{d}{dr} - \frac{l(l+1)}{r^2} - \frac{2m}{\hbar^2} V(r) + k^2 \right) R_l(k, r) = 0 \quad (2.3)$$

Then, we already know that the form of wave function when r is very large, i.e.

$$\psi(r) = e^{ikz} + f(k, \theta) \frac{e^{ikr}}{r} \quad (2.4)$$

by spherical expanding we get: For left side:

$$\psi(r) = \sum_{l=0}^{\infty} R_l(k, r) P_l(\cos[\theta]) \quad (2.5)$$

For right side:

$$e^{ikz} = \sum_{l=0}^{\infty} (2l+1) i^l (kr)^{-1} \sin \left[kr - \frac{l\pi}{2} \right] P_l(\cos[\theta]) \quad (2.6)$$

$$f(k, \theta) = \sum_{l=0}^{\infty} f_l(k) P_l(\cos[\theta]) \quad (2.7)$$

Thus we have the Radial part with different l as

$$R_l(k, r) = (2l+1) i^l (kr)^{-1} \sin \left[kr - \frac{l\pi}{2} \right] + f_l(k) \frac{e^{ikr}}{r} \quad (2.8)$$

If we are treating some finite range potential, there exists a general solution: Suppose that the potential can be written as

$$V(r) = \begin{cases} V(r), & r < r_0 \\ 0, & r > r_0 \end{cases} \quad (2.9)$$

When $r > r_0$ we have

$$\left(\frac{d^2}{dr^2} + \frac{2}{r} \frac{d}{dr} - \frac{l(l+1)}{r^2} + k^2 \right) R_l(k, r) = 0 \quad (2.10)$$

Solution of this equation has been solved well as following

$$R_l(k, r) = B_l(k) j_l(kr) + C_l(k) y_l(kr) \quad (2.11)$$

When $r \rightarrow \infty$, we get the asymptotic form of Bessel function as

$$R_l(k, r) = \frac{1}{kr} \left\{ A_l(k) \text{Sin} \left[kr - \frac{l\pi}{2} - \delta_l(k) \right] \right\} \quad (2.12)$$

where

$$A_l(k) = \sqrt{B_l^2(k) + C_l^2(k)}, \quad \delta_l(k) = \text{ArcTan} \left[\frac{C_l(k)}{B_l(k)} \right] \quad (2.13)$$

Comparing [12] and [16], we get that

$$f_l(k) = \frac{2l+1}{2ik} [e^{2i\delta_l(k)} - 1] \quad (2.14)$$

$$A_l(k) = (2l+1)i^l e^{i\delta_l(k)} \quad (2.15)$$

Finally, we have

$$f(k, \theta) = \sum_{l=0}^{\infty} \frac{2l+1}{2ik} [e^{2i\delta_l(k)} - 1] P_l(\text{Cos}[\theta]) \quad (2.16)$$

Now, if we connect the boundary condition inside r_0 , we can solve the $\delta_l(k)$ and solve this problem. For now, we can say that if we get all $\delta_l(k)$, then we solve this problem well. Nevertheless, that is a massive project because there are infinite l , and for each l , δ is a function of k ; thus, we need a good approximation for our system. Then, the last feature, low temperature, can be used.

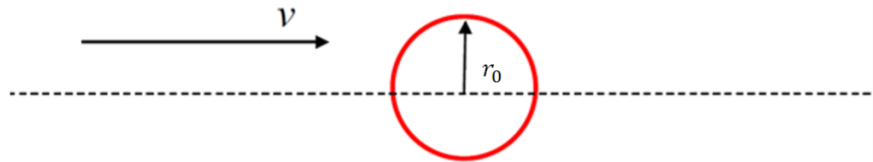


Figure 2.1: shows the low-energy scattering. Only the lowest several partial wave matter.

As shown in Fig. 2.1, particles can hit this finite potential with l less than

$$l < l_{\max} = \frac{mv r_0}{\hbar} = r_0 k \quad (2.17)$$

where r_0 is the potential range. Thus, At low-energy limit, i.e. $r_0 k \rightarrow 0$, we have $l_{\max} \rightarrow 0$, which means we can consider s -wave only.

$$f_0(k) = \frac{1}{2ik} [e^{2i\delta_l(k)} - 1] = \frac{1}{k} e^{i\delta_0(k)} \text{Sin} [\delta_0(k)] \quad (2.18)$$

Thus, only one parameter $\delta_0(k)$ representing whole process. As historical preference, we introduce an equivalent parameter, scattering length a_s

$$a_s = a_0(k)|_{k \rightarrow 0} = \lim_{k \rightarrow 0} \left[-\frac{1}{k} \text{Tan} [\delta_0(k)] \right] \quad (2.19)$$

where a_s is independent with k , just as what we want. Conclusion: when we deal with finite range potential scattering, not need to be finite intensity potential, and if the particle's momentum k is so small that $k \ll 1/a$, where a is the potential range, we can use only one parameter a_0 to describe the whole scattering process. The approximations made here are listed below: Finite range potential gives r_0 . $k \ll 1/r_0$ where k is scattering momentum divided by \hbar , and r_0 is potential range Scattering length a_0 actually depends on k , however if we consider the limit $k \rightarrow 0$, we can ignore this variance. This very beautiful property gives us a way to deal with not-weak atom-atom scattering problem even with strong interaction.

2.2 Quantum droplet

In this section, we introduce the basic theory of quantum droplets. We start from the most basic theory of BEC and first provide the treatment of BEC by Bogoliubov, which

leads to the correction of ground state energy given by LHY correction. This part describes a detailed derivation than the introduction part. Subsequently, we introduce the theory of two-component BEC and obtain a numerical solution of the LHY correction in this case, which typically has no analytical solution if the mass of both species is imbalanced. Then, we explain the formation mechanism of the quantum droplet made of Bose mixture. In this subsection, we consider only the bulk sample, ignoring the kinetic energy term and finally obtain the density of a stable quantum droplet as a function of inter-species interaction. We will discuss the theory and simulation of the finite-size droplet in the Experiment Chapter 5.

2.2.1 Dilute Bose system: Pseudo-Hamiltonian and Bogoliubov transformation

There are three keywords for this special system: short-range interaction, dilute and low-temperature. Short-range gives a length scale r_0 , which represent the inter-particle potential range. Dilute means: $n^{1/3}r_0 \ll 1$, where n denote particle number density. Low temperature(energy) means $kr_0 \ll 1$, where k denotes momentum. These three conditions allow us to replace the real complicated potential between atoms by a pseudo-potential. The only related parameter then is the s -wave scattering length a_s when the temperature is low enough, as we mentioned before.

As we can use a_s representing scattering process, we can write down a pseudo-potential, which gives the same effect as the original one. This procedure first done by *Fermi* as following

$$V(r) = g\delta(r)\partial_r \cdot r = \frac{4\pi\hbar^2 a_s}{m}\delta(r)\partial_r \cdot r \quad (2.20)$$

which is a contact potential only affect two atoms when they have same r . The last term $\partial_r \cdot r$ eliminates wave function's divergence at $r \rightarrow 0$, due to it has form of

$\psi \rightarrow 1 - a_S/r$. if we write the potential as

$$V(r) = g_R \delta(r) \quad (2.21)$$

where g_R denotes the interaction intensity. Note that this g_R cannot be considered as physics quantity due to its divergence at $r \rightarrow 0$. However, the relationship between g_R and g can be obtain by *Dyson Equation*.

$$g_R = g + g \Sigma^* g_R \quad (2.22)$$

where g_R represent normalized interaction strength, and Σ^* represent the proper self-energy of system, i.e.

$$g_R = \frac{4\pi\hbar^2 a_S}{m} \left(1 + \frac{g_R}{V} \sum_{k=0}^{\infty} \frac{1}{\hbar^2 k^2 / m} \right) \quad (2.23)$$

by just take the second order correction (loop correction), we get

$$g_R = g \left(1 + \frac{g}{V} \sum_{k=0}^{\infty} \frac{1}{\hbar^2 k^2 / m} \right) \quad (2.24)$$

The second term is actually diverge, which represents high energy scattering. This term will only be used when we need to sum over some term with all high energy collision process. In most time, we can just take g as

$$g = \frac{4\pi\hbar^2 a_S}{m} \quad (2.25)$$

Then, we can rewrite the whole Hamiltonian as following

$$\begin{aligned}\hat{H}_0 &= \frac{1}{2} \int \nabla \hat{\Psi}^\dagger(x) \nabla \hat{\Psi}(x) dx \\ H_1 &\simeq \frac{1}{2} \int \hat{\Psi}^\dagger(x) \hat{\Psi}^\dagger(x') g \delta(x - x') \hat{\Psi}(x') \hat{\Psi}(x) dx dx' \\ &= \frac{g}{2} \int \hat{\Psi}^\dagger(x) \hat{\Psi}^\dagger(x) \hat{\Psi}(x) \hat{\Psi}(x) dx\end{aligned}\quad (2.26)$$

Fourier transformation provides the Hamiltonian in momentum space as

$$H_{\text{pseudo}} = \sum_k \epsilon_k \hat{a}_k^\dagger \hat{a}_k + \frac{g}{2V} \sum_{\{k_i\}} \hat{a}_{k_1}^\dagger \hat{a}_{k_2}^\dagger \hat{a}_{k_3} \hat{a}_{k_4} \quad (2.27)$$

where $k_1 + k_2 = k_3 + k_4$, satisfies momentum conservation. This is just the pseudo-Hamiltonian for many-Boson system. Because of the special role of the state with $k = 0$, i.e. condensate, we separate ladder operator into two piece for whole Bose gas

$$\hat{\Psi}(x) = \frac{1}{\sqrt{V}} \sum_{p \neq 0} e^{ipx} \hat{a}_p + \frac{1}{\sqrt{V}} \hat{a}_0 = \hat{\Psi}'(x) + \frac{1}{\sqrt{V}} \hat{a}_0 \quad (2.28)$$

$$\hat{\Psi}^\dagger(x) = \frac{1}{\sqrt{V}} \sum_{p \neq 0} e^{-ipx} \hat{a}_p^\dagger + \frac{1}{\sqrt{V}} \hat{a}_0^\dagger = \hat{\Psi}'^\dagger(x) + \frac{1}{\sqrt{V}} \hat{a}_0^\dagger \quad (2.29)$$

where $\hat{a}_0 = \hat{a}_0^\dagger = \sqrt{n} = \sqrt{\frac{N}{V}}$, indicating the MF condensate wave-function without the quantum fluctuation. Noticed that, when we use mean field theory to calculate a system, we need pay attention to what kind of fluctuation we ignored in the calculation, then at necessary time, we can get it back.

put them into eq. 2.27, then simply

$$\begin{aligned} H = & \frac{gN^2}{2V} + \sum_{k \neq 0} (\epsilon_k + gn_0) \hat{a}_k^\dagger \hat{a}_k + \frac{gN}{2V} \sum_{k \neq 0} (\hat{a}_k^\dagger \hat{a}_{-k}^\dagger + \hat{a}_k \hat{a}_{-k}) \\ & + \frac{g\sqrt{N}}{2V} \sum_{k_1+k_2+k_3=0} (\hat{a}_{k_1}^\dagger \hat{a}_{k_2}^\dagger \hat{a}_{k_3} + \hat{a}_{k_1}^\dagger \hat{a}_{k_2} \hat{a}_{k_3}) + \frac{g}{2V} \sum_{k_i \neq 0} \hat{a}_{k_1}^\dagger \hat{a}_{k_2}^\dagger \hat{a}_{k_3} \hat{a}_{k_4} \end{aligned} \quad (2.30)$$

Here, we drop the terms with order less than N , because they are much smaller than others when temperature is quite low and large amount of atoms are condensate. (Noted that, if considering the last two term, we will get the Beliaev-Landau Damping.)

$$H_{\text{pseudo}} \simeq \frac{gN^2}{2V} + \sum_{k \neq 0} (\epsilon_k + gn_0) \hat{a}_k^\dagger \hat{a}_k + \frac{gn_0}{2} \sum_{k \neq 0} (\hat{a}_k^\dagger \hat{a}_{-k}^\dagger + \hat{a}_k \hat{a}_{-k}) \quad (2.31)$$

Now, as quadratic form, we can diagonalize it with so called Bogoliubov transformation

$$\begin{aligned} \hat{a}_k &= u_k \hat{\alpha}_k - v_k \alpha_{-k}^\dagger \\ \hat{a}_{-k} &= u_k \hat{\alpha}_{-k} - v_k \alpha_k^\dagger \end{aligned} \quad (2.32)$$

where α_k^\dagger (α_k) is a new ladder operator, which actually denote create(annihilate) a quasi-particle in this condensate system. u_k and v_k is c-number as function of k and E_k , which gives the spectrum of quasi-particle. Finally, we give out the diagonalized Hamiltonian as

$$\begin{aligned} H_{\text{pseudo}} &\simeq \frac{gN^2}{2V} - \frac{1}{2} \sum_{k \neq 0} \left(\epsilon_k + \frac{gN}{V} - E_k \right) + \sum_{k \neq 0} E_k \hat{\alpha}_k^\dagger \hat{\alpha}_k \\ E_k &= \sqrt{\epsilon_k \left(\epsilon_k + \frac{2gN}{V} \right)} = \sqrt{\frac{\hbar^2 k^2}{2m} \left(\frac{\hbar^2 k^2}{2m} + \frac{2gN}{V} \right)} \end{aligned} \quad (2.33)$$

The gap-less linear low energy excited dissipation relation gives the super fluid prop-

erty, as shown in Fig. 2.2. when k get larger, it turn back to classical particle.

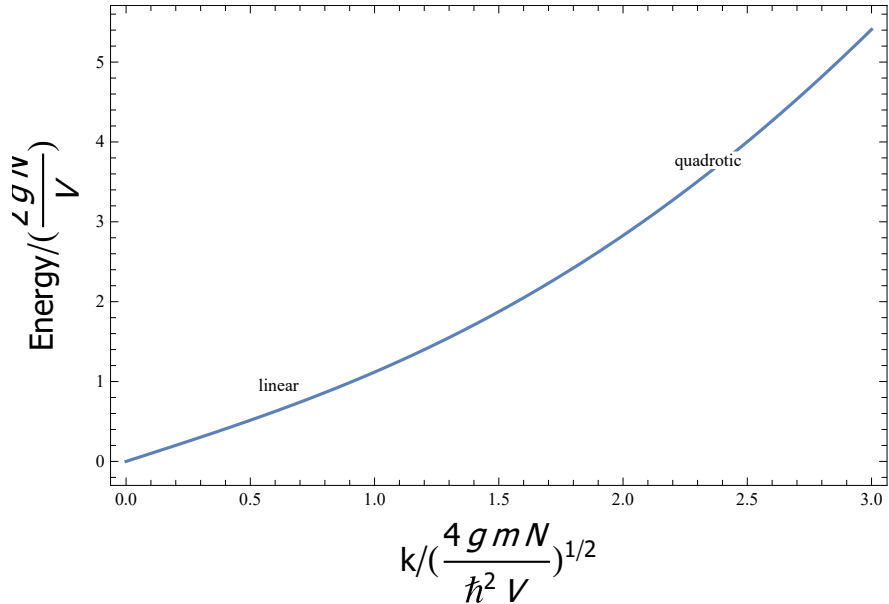


Figure 2.2: This plot shows the dissipation relationship for quasi-particle in the Bose-condensation. When k is small, it looks like a phonon, however, when k goes large it back to a particle-like quasi-particle.

Now, let's consider what happens when $g < 0$, i.e. attractive potential between atoms. The excitation spectrum will have no low-energy excitation part, since the low-energy excitation indicates the density wave and this will cause positive feedback to increase the density of the sample, which renders the so-called collapsing of BEC. However, the high-energy excitation is still there as shown in Fig. 2.3 We will argue weather this single species BEC with negative interaction can form the quantum droplet in the next subsection.

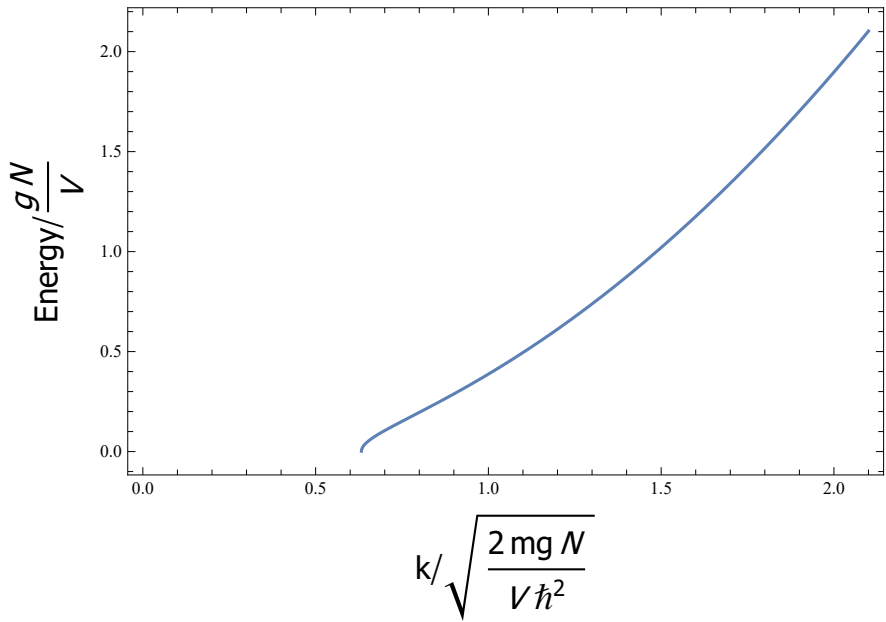


Figure 2.3: This plot shows the dissipation relationship for attractive Bose system, i.e. $g < 0$.

2.2.2 Ground state and LHY correction

Now let us consider the ground state energy of this system. Directly take the lowest energy level from eq. 2.33, we have

$$E_{\text{GS}} = \frac{gN^2}{2V} - \frac{1}{2} \sum_{k \neq 0} \left(\epsilon_k + \frac{gN}{V} - E_k \right) \quad (2.34)$$

where first term represent the mean field energy shift from “vacuum”, and second term come from quantum fluctuation (at zero temperature), i.e.

$$-\frac{1}{2} \sum_{k \neq 0} \left(\epsilon_k + \frac{gN}{V} - E_k \right) = -\frac{1}{2} \sum_{k \neq 0} \left(\frac{\hbar^2 k^2}{2m} + \frac{gN}{V} - \sqrt{\frac{\hbar^2 k^2}{2m} \left(\frac{\hbar^2 k^2}{2m} + \frac{2gN}{V} \right)} \right) \quad (2.35)$$

If you plot the term in the summation, you will find it decays with k increasing. However, if we expand it in series, we have

$$\begin{aligned} & \frac{\hbar^2 k^2}{2m} + \frac{gN}{V} - \sqrt{\frac{\hbar^2 k^2}{2m} \left(\frac{\hbar^2 k^2}{2m} + \frac{2gN}{V} \right)} \\ &= \frac{1}{2} \left(\frac{gN}{V} \right)^2 \left(\frac{2m}{\hbar^2} \right) \frac{1}{k^2} - \frac{1}{2} \left(\frac{gN}{V} \right)^3 \left(\frac{2m}{\hbar^2} \right)^2 \frac{1}{k^4} + \dots \end{aligned} \quad (2.36)$$

with leading proportional to $\frac{1}{k^2}$, we have divergence when sum over k to infinite. This divergence is due to the pseudo-potential with $\delta(r)$ actually does not allow calculation for large k , thus, we need do re-normalization to truncate this $\frac{1}{k^2}$ divergence.

Recalling the renormalized interaction g_R in eq. 2.24, we have

$$g_R = g + \frac{g^2}{V} \sum_k \frac{m}{\hbar^2 k^2} \quad (2.37)$$

Then total energy will be

$$\begin{aligned} E_{\text{GS}}^R &= \frac{gN^2}{2V} - \frac{1}{2} \sum_{k \neq 0} \left(\frac{\hbar^2 k^2}{2m} + \frac{gN}{V} \right. \\ &\quad \left. - \sqrt{\frac{\hbar^2 k^2}{2m} \left(\frac{\hbar^2 k^2}{2m} + \frac{2gN}{V} \right)} - \left(\frac{gN}{V} \right)^2 \left(\frac{2m}{\hbar^2} \right) \frac{1}{k^2} \right) \end{aligned} \quad (2.38)$$

Directly do the summation, we get the famous LHY correction

$$\frac{E_{\text{GS}}^R}{V} = \frac{gn^2}{2} \left(1 + \frac{128}{15\pi^{1/2}} (na^3)^{1/2} \right) \quad (2.39)$$

where $a = |a_S|$. For positive interaction strength $g > 0$, we can find the LHY correction is a tiny *correction* when density is low, with an order of na^3 . This has been experimentally verified in strong interacting Bose System [Navon et al., 2011]. What we are interested is the case with negative interaction strength, i.e. $g < 0$. The ground

state energy of this case shows that there is a local minimum for a specific density. Noted that actually for $g < 0$ the ground state energy formalism is ill-defined, since one cannot do the summation to get the LHY correction unless rule out the imaginary part of the low-energy excitation section. Moreover, considering the density of the local minimum, we will find that it is at the level of $na^3 \approx 1$, which actually entering the strong interaction regime.

2.2.3 Quantum Depletion and Mechanism of LHY Droplet

Now, Let us consider a ground state of BEC at zero temperature, how many particles will not stay at $k = 0$ state? The answer is that directly summing all non-zero k state in the ground state. as following

$$n_{dp} = \frac{1}{V} \sum_{k \neq 0} v_k^2 = \frac{1}{3\pi^2} \left(\frac{mc}{\hbar} \right)^3 \propto \xi^{-3} \quad (2.40)$$

where v_k is parameter in Bogoliubov transformation, $c = \sqrt{\frac{gn}{2m}}$ is the first sound speed in BEC, and $\xi = \frac{\hbar}{\sqrt{2mg}}$ is healing length. The fraction of depleted particle is

$$\frac{n_{dp}}{n} = \frac{8}{3\sqrt{\pi}} \sqrt{na_S^3} \quad (2.41)$$

we can directly read that with increasing of na_S^3 , more particles are kicked out of the condensate. Meanwhile, these particles will contribute an additional energy to ground state energy, i.e. the LHY correction we mentioned before.

2.2.4 Mean-field theory of Double BEC

With a brief review in several previous subsections, we found that: if there is only one species, since the LHY energy is always much smaller than MF energy, unless we increase the density or interaction strength to a strong interaction regime, the pure

quantum effect always remains as a tiny correction. Therefore, only if there are some methods to maintain the LHY correction and reduce the MF energy by other effects (such as dipolar interaction or another species) can we make the MF energy scale approximate to the LHY correction. Finally, we have the opportunity to demonstrate this pure quantum effect. As Petrov mentioned in the seminal work [Petrov, 2015]: if we consider a two-species BEC sample with intra-species interaction in both positive while adjusting inter-species interaction negative enough to make almost total MF be zero, the LHY correction, since it is derived from quantum depletion, can maintain at the $g_{ii}n_i^3$ level and the MF energy can be an arbitrary proxy to zero, which form the opportunity to observe LHY correction directly. In other words, LHY correction can still exist even MF energy equals 0. In this way, it is possible to form an ultra-dilute quantum droplet since the interaction is still weak and density is actually remaining in the typical gaseous BEC level.

Now, we turn to describe double BEC with mean field theory. Hamiltonian for BEC with two species is

$$\begin{aligned} H_{\text{tot}} = & \sum_k \epsilon_{1,k} \hat{a}_{1,k}^\dagger \hat{a}_{1,k} + \frac{g_{11}}{2V} \sum_{\{k_i\}} \hat{a}_{1,k_1}^\dagger \hat{a}_{1,k_2}^\dagger \hat{a}_{1,k_3} \hat{a}_{1,k_4} + \sum_k \epsilon_{2,k} \hat{a}_{2,k}^\dagger \hat{a}_{2,k} \\ & + \frac{g_{22}}{2V} \sum_{\{k_i\}} \hat{a}_{2,k_1}^\dagger \hat{a}_{2,k_2}^\dagger \hat{a}_{2,k_3} \hat{a}_{2,k_4} + \frac{g_{12}}{V} \sum_{\{k_i\}} \hat{a}_{2,k_1}^\dagger \hat{a}_{1,k_2}^\dagger \hat{a}_{1,k_3} \hat{a}_{2,k_4} \end{aligned} \quad (2.42)$$

where $k_1+k_2 = k_3+k_4$, satisfy momentum conservation. g_{ii} represent intra-interaction strength, and g_{12} for inter-interaction. $\hat{a}_{i,k}^\dagger(\hat{a}_{i,k})$ denote the ladder operator for i^{th} component. Because of the special role of the state with $k=0$, i.e. condensate, we separate ladder operator into two piece for whole Bose gas

$$\begin{aligned} \hat{\Psi}_i(x) &= \frac{1}{\sqrt{V}} \sum_{p \neq 0} e^{ipx} \hat{a}_{i,p} + \frac{1}{\sqrt{V}} \hat{a}_{i,0} = \hat{\Psi}'_i(x) + \frac{1}{\sqrt{V}} \hat{a}_{i,0} \\ \hat{\Psi}_i^\dagger(x) &= \frac{1}{\sqrt{V}} \sum_{p \neq 0} e^{-ipx} \hat{a}_{i,p}^\dagger + \frac{1}{\sqrt{V}} \hat{a}_{i,0}^\dagger = \hat{\Psi}'^\dagger(x) + \frac{1}{\sqrt{V}} \hat{a}_{i,0}^\dagger \end{aligned} \quad (2.43)$$

Then we get Hamiltonian as

$$\begin{aligned}
H = & \frac{g_{11}N_1^2 + g_{22}N_2^2 + 2g_{12}N_1N_2}{2V} + \sum_{k \neq 0} \left(\epsilon_{1,k} + \frac{g_{11}N_1 + g_{12}N_2}{V} \right) \hat{a}_{1,k}^\dagger \hat{a}_{1,k} \\
& + \sum_{k \neq 0} \left(\epsilon_{2,k} + \frac{g_{22}N_2 + g_{12}N_1}{V} \right) \hat{a}_{2,k}^\dagger \hat{a}_{2,k} + \frac{g_{11}N_1}{2V} \sum_{k \neq 0} \left(\hat{a}_{1,k}^\dagger \hat{a}_{1,-k}^\dagger + \hat{a}_{1,k} \hat{a}_{1,-k} \right) \\
& + \frac{g_{22}N_2}{2V} \sum_{k \neq 0} \left(\hat{a}_{2,k}^\dagger \hat{a}_{2,-k}^\dagger + \hat{a}_{2,k} \hat{a}_{2,-k} \right) \\
& + \frac{g_{12}\sqrt{N_1N_2}}{2V} \sum_{k \neq 0} \left(\hat{a}_{1,k}^\dagger \hat{a}_{2,k} + \hat{a}_{2,k}^\dagger \hat{a}_{1,k} + \hat{a}_{1,k} \hat{a}_{2,-k} + \hat{a}_{2,k}^\dagger \hat{a}_{1,-k} \right)
\end{aligned} \tag{2.44}$$

where we only keep the second order of N_i , dropping third and forth order of N_i . Then, diagonalize this Hamiltonian by extended Bogoliubov transformation for double BEC, we have

$$\begin{aligned}
H = & \frac{g_{11}N_1^2 + g_{22}N_2^2 + 2g_{12}N_1N_2}{2V} \\
& + \frac{1}{2} \sum_{k \neq 0} \left(E_+ + E_- - \frac{\hbar^2 k^2}{2m_1} - \frac{\hbar^2 k^2}{2m_2} - \frac{g_{11}N_1 + g_{22}N_2}{V} \right) \\
& + \sum_{k \neq 0} E_{+,k} \hat{a}_{+,k}^\dagger \hat{a}_{+,k} + \sum_{k \neq 0} E_{-,k} \hat{a}_{-,k}^\dagger \hat{a}_{-,k}
\end{aligned} \tag{2.45}$$

where

$$E_\pm = \sqrt{\frac{\omega_1^2 + \omega_2^2}{2} \pm \sqrt{\left(\frac{\omega_1^2 - \omega_2^2}{2}\right)^2 + \frac{g_{12}^2 N_1 N_2}{V^2} \frac{\hbar^2 k^4}{m_1 m_2}}} \tag{2.46}$$

where

$$\omega_i = \sqrt{\frac{\hbar^2 k^2}{2m_i} \left(\frac{\hbar^2 k^2}{2m_i} + \frac{2g_{ii}N_i}{V} \right)} \tag{2.47}$$

We plot the spectrum for each channel E_+ and E_- , with $\delta g = \sqrt{g_{11}g_{22}} - g_{12} > 0$ and $\delta g = \sqrt{g_{11}g_{22}} - g_{12} < 0$. Where we find similar spectrum with one component BEC. For $\delta g < 0$, we get complex energy with small k , which represent unstable of

the system.

2.2.5 Ground state and LHY correction of double species BEC

Ground state energy with LHY correction for the two-species BEC is

$$\begin{aligned} E_{\text{GS}} = & \frac{g_{11}N_1^2 + g_{22}N_2^2 + 2g_{12}N_1N_2}{2V} \\ & + \frac{1}{2} \sum_{k \neq 0} \left(E_+ + E_- - \frac{\hbar^2 k^2}{2m_1} - \frac{\hbar^2 k^2}{2m_2} - \frac{g_{11}N_1 + g_{22}N_2}{V} \right) \end{aligned} \quad (2.48)$$

After re-normalization we have

$$\begin{aligned} E_{\text{GS}}^R = & \frac{g_{11}N_1^2 + g_{22}N_2^2 + 2g_{12}N_1N_2}{2V} \\ & + \frac{1}{2} \sum_{k \neq 0} \left(E_+ + E_- - \frac{\hbar^2 k^2}{2m_1} - \frac{\hbar^2 k^2}{2m_2} - \frac{g_{11}N_1 + g_{22}N_2}{V} \right. \\ & \left. + \frac{m_1g_{11}^2 N_1^2/V^2 + m_2g_{22}^2 N_2^2/V^2 + 4\frac{m_1m_2}{m_1+m_2}g_{12}^2 N_1N_2/V^2}{\hbar^2 k^2} \right) \end{aligned} \quad (2.49)$$

The second term is LHY term which can be rewritten as

$$\begin{aligned} E_{\text{LHY}} = & \frac{1}{2} \sum_{k \neq 0} \left(\sqrt{\frac{\omega_1^2 + \omega_2^2}{2}} + \sqrt{\left(\frac{\omega_1^2 - \omega_2^2}{2}\right)^2 + g_{12}^2 n_1 n_2 \frac{\hbar^4 k^4}{m_1 m_2}} \right. \\ & + \sqrt{\frac{\omega_1^2 + \omega_2^2}{2}} - \sqrt{\left(\frac{\omega_1^2 - \omega_2^2}{2}\right)^2 + g_{12}^2 n_1 n_2 \frac{\hbar^4 k^4}{m_1 m_2}} \\ & \left. - \frac{\hbar^2 k^2}{2m_1} - \frac{\hbar^2 k^2}{2m_2} - g_{11}n_1 - g_{22}n_2 + \frac{m_1g_{11}^2 n_1^2 + m_2g_{22}^2 n_2^2 + 4\frac{m_1m_2}{m_1+m_2}g_{12}^2 n_1 n_2}{\hbar^2 k^2} \right) \end{aligned} \quad (2.50)$$

Replace summation by integral ($\sum_k \rightarrow V \int d\vec{k}$), we have the following formula. For simplicity, we reform it into dimensionless form

$$\begin{aligned} \mathcal{E}_{\text{LHY}} = & C_1 \int_0^\infty \frac{15}{32} \tilde{k}^2 \left\{ \sqrt{\left[\frac{1}{2} \left(\frac{\tilde{k}^2}{2} \left(\frac{\tilde{k}^2}{2} + 2 \right) + \frac{1}{\gamma^2} \frac{\tilde{k}^2}{2} \left(\frac{\tilde{k}^2}{2} + 2y\gamma \right) \right) \right.} \right. \\ & + \sqrt{\left(\frac{1}{2} \left(\frac{\tilde{k}^2}{2} \left(\frac{\tilde{k}^2}{2} + 2 \right) - \frac{1}{\gamma^2} \frac{\tilde{k}^2}{2} \left(\frac{\tilde{k}^2}{2} + 2y\gamma \right) \right) \right)^2 + \frac{xy}{\gamma} \tilde{k}^4} \\ & + \sqrt{\left[\frac{1}{2} \left(\frac{\tilde{k}^2}{2} \left(\frac{\tilde{k}^2}{2} + 2 \right) + \frac{1}{\gamma^2} \frac{\tilde{k}^2}{2} \left(\frac{\tilde{k}^2}{2} + 2y\gamma \right) \right) \right.} \\ & - \sqrt{\left(\frac{1}{2} \left(\frac{\tilde{k}^2}{2} \left(\frac{\tilde{k}^2}{2} + 2 \right) - \frac{1}{\gamma^2} \frac{\tilde{k}^2}{2} \left(\frac{\tilde{k}^2}{2} + 2y\gamma \right) \right) \right)^2 + \frac{xy}{\gamma} \tilde{k}^4} \\ & - \frac{\tilde{k}^2}{2} \left(1 + \frac{1}{\gamma} \right) - 1 - y + \frac{1 + \gamma y^2 + \frac{4xy\gamma}{1+\gamma}}{\tilde{k}^2} \left. \right\} d\tilde{k} \end{aligned} \quad (2.51)$$

where

$$\begin{aligned} C_1 &= g_{11}n_1 \left(\frac{\sqrt{m_1 g_{11} n_1}}{\hbar} \right)^3, \gamma = \frac{m_2}{m_1} \\ x &= \frac{g_{12}^2}{g_{11}g_{22}}, y = \frac{g_{22}n_2}{g_{11}n_1}, \tilde{k} = \frac{\hbar k}{\sqrt{m_1 g_{11} n_1}} \end{aligned} \quad (2.52)$$

The dimensionless of two new excitation branches are

$$\begin{aligned} \frac{\omega_1}{g_{11}n_1} &= \sqrt{\frac{\hbar^2 k^2}{2m_1 g_{11} n_1} \left(\frac{\hbar^2 k^2}{2m_1 g_{11} n_1} + 2 \right)} = \sqrt{\frac{\tilde{k}^2}{2} \left(\frac{\tilde{k}^2}{2} + 2 \right)} \\ \frac{\omega_2}{g_{11}n_1} &= \sqrt{\frac{\hbar^2 k^2}{2m_2 g_{11} n_1} \left(\frac{\hbar^2 k^2}{2m_2 g_{11} n_1} + 2 \frac{g_{22}n_2}{g_{11}n_1} \right)} \\ &= \sqrt{\frac{1}{\gamma} \frac{\tilde{k}^2}{2} \left(\frac{1}{\gamma} \frac{\tilde{k}^2}{2} + 2y \right)} = \frac{1}{\gamma} \sqrt{\frac{\tilde{k}^2}{2} \left(\frac{\tilde{k}^2}{2} + 2y\gamma \right)} \end{aligned} \quad (2.53)$$

we take out the dimensionless part of it, i.e.

$$E_{\text{GS}}^R = \frac{g_{11}N_1^2 + g_{22}N_2^2 + 2g_{12}N_1N_2}{2V} + \frac{8V}{15\pi^2}m_1^{3/2}(g_{11}n_1)^{5/2}f\left(\frac{m_2}{m_1}, \frac{g_{12}^2}{g_{11}g_{22}}, \frac{g_{22}n_2}{g_{11}n_1}\right) \quad (2.54)$$

Where f is always larger than 0 and is dimensionless.

For convenient, we rewrite the MF energy term a quadratic term and make the diagonalization

$$\frac{1}{2} \begin{pmatrix} & \\ n_1 & n_2 \end{pmatrix} \begin{pmatrix} g_{11} & g_{12} \\ g_{12} & g_{22} \end{pmatrix} \begin{pmatrix} n_1 \\ n_2 \end{pmatrix} \quad (2.55)$$

diagonalize

$$\lambda_+ = \frac{g_{11} + g_{22}}{2}, \lambda_- = \frac{\sqrt{g_{11}g_{22}}}{g_{11} + g_{22}}\delta g \quad (2.56)$$

$$n_+ = \frac{n_1\sqrt{g_{11}} - n_2\sqrt{g_{22}}}{\sqrt{g_{11} + g_{22}}}, n_- = \frac{n_1\sqrt{g_{22}} + n_2\sqrt{g_{11}}}{\sqrt{g_{11} + g_{22}}} \quad (2.57)$$

We can read from the above formula that MF energy is proportional to δgn^2 , so it provides an attractive energy when $\delta g < 0$. This term tends to increase the density of the sample, because increasing density brings lower energy (more negative). The LHY term is a positive ratio of $g_{ii}n^2/5$. Because its index is higher than MF's n^2 , the sample tends to reduce its density in high-density region. These two terms compete and finally provide a balanced density, as shown in Fig. 2.4. The density is 0 when $\delta g = 0$, indicating that the self-bound state can only form starting from this point. When δg is negative, the density of the system tends to increase rapidly with δg . This offers a window for experiment research. Considering that the density of the BEC sample we usually prepare is about 10^{12} to 10^{13} cm^{-3} . Based on this information, we can choose the appropriate inter-species interaction (actually choose the magnetic field, as we use the Feshbach resonance between two species) to prepare the quantum droplet. We put the detailed content in Chap.5.

The discussion here does not involve the kinetic energy term because we are con-

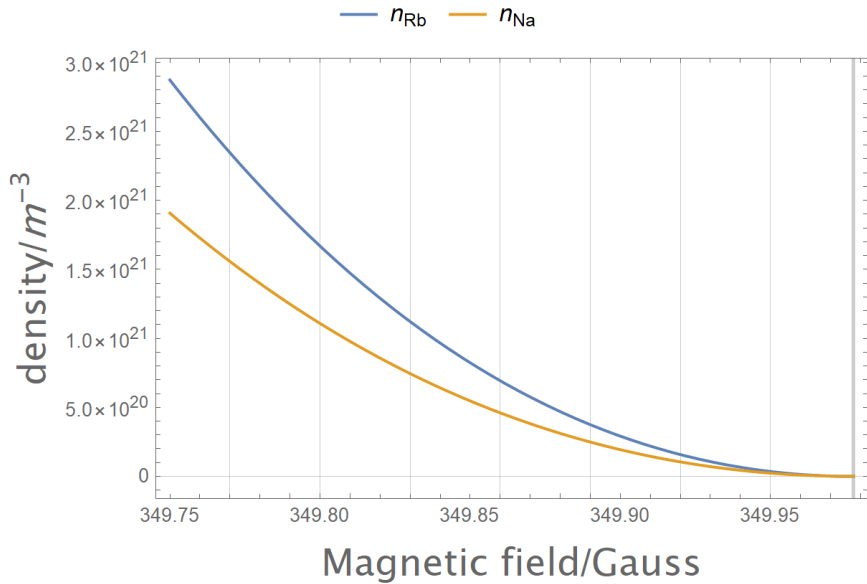


Figure 2.4: Calculated droplet density as a function of δg . The gray vertical line at the right side shows the zero density boundary. The possible window of magnetic field is around 349.8 Gauss. More details about the Feshbach resonance can be found in Chap. 4 and Chap. 5.

sidering a homogeneous sample, which means that the density of the sample is uniform. However, the actual quantum droplet must be limited in size. Thus, there will be a boundary, and this boundary will bring kinetic energy. This kinetic energy plays a decisive role in the occurrence of liquid-gas phase transition under a specific delta g. The details will be discussed in Chap. 5. What needs to be reminded here is that the density calculated here does not take into account the constraints of surface tension caused by kinetic energy. It will be slightly lower than the density in the real experimental sample. Of course, if it is an extensive droplet sample, this difference can be ignored.

End of chapter.

Chapter 3

Apparatus

工欲善其事,必先利其器。

A craftsman must sharpen his tools to do his job.

— Confucius

The Analects (5th century BC)

This chapter describes the Na-Rb machine and the upgrades we made for our droplet experiment. As most of the setup has been described by the previous thesis [Wang, 2016; Li, 2015], we only shortly make a summary in Sec. 3.1 for the completeness of this chapter. In Sec. 3.2, we turn to the image system upgrades for measuring the droplet sample with several μm sizes. We design a $15\times$ magnification image system with a resolution of $2 \mu\text{m}$. Besides, we upgraded the mechanical part onto an electro-translation stage, which can follow the ToF of the free-falling sample without worsening the image resolution. We detailedly describe the high-magnetic field in-situ image scheme for subtracting the sample's density profile reliable. To control more cameras from different manufacturers, I built a multi-camera control platform with image processing called CAMIMA. We will introduce it in Sec. 3.3 as a manual for future using and upgrading. Finally, we discuss several improvements such as fast-coil for fast controlling magnetic field (Sec. 3.4), magnetic field gradient com-

pensation (Sec. 3.5.1) and coil antennas for increasing the Rabi frequency of Rb (Na) micro-wave transition (Sec. 3.5.2).

3.1 Overview: Na-Rb machine I

A cold atom machine capable of producing reproducible samples with stable atomic conditions is indispensable for the following experiments. So, even though the Na-Rb machine in our laboratory has been running for longer than eight years, many aspects still need to improve to make the sample condition more stable. [Li, 2021] describes many efforts we made: optimization of the micro-wave evaporation procedure for Rb sympathies cooling of Na; a new ultra-stable magnetic field servo system for achieving hundred-Gauss with only two mG level fluctuation. Besides stability, producing more atoms is another goal for many experiments because there are always various types of loss during preparing the atomic (or molecular) samples. More numbers of final sample can make detection easier and offer more opportunities to study new physics. In the droplet experiment [Guo et al., 2021a], if we produce a sample with ten times more numbers (i.e. 10^6 for each species), we can study more properties of the bulk sample, such as flat-top density profile [Petrov, 2015], the surface excitation modes [Petrov, 2015] and achieving a longer lifetime.

3.1.1 Producing Na-Rb Bose-Einstein condensate mixtures

Our experiment starts from Na and Rb dispensers. We fire the Rb dispenser every day with a relatively low current of 1.9 A (temperature of less than 500 K). Na dispenser fires only once a month, however, with a relatively high current (3.5 A) and temperature (600 K). The temperature and current conversion chart is shown in Fig. 3.2. The reason for not firing the Na dispenser at a low current is that the temperature for turning on the Na dispenser (Na starts to spray out) is still too high and breaks

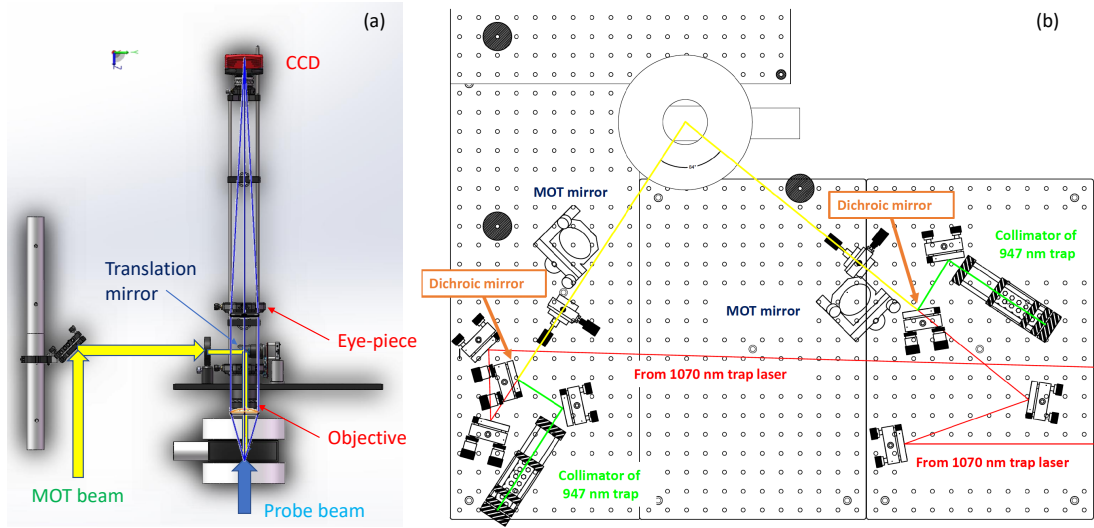


Figure 3.1: (a) shows the Front view of the Na-Rb machine. The up-down image(pumping) shares the same optical path with MOT laser. After MOT loading, we switch the mirror cart away to leave path for up-down image. (b) shows the optical trap laser layout as a top view. Image is taken from [Li, 2021]

the vacuum. Since we use a single chamber design, we have to make the trade-off between the loading rate of MOT and the vacuum condition. Thanks to the light-induced atomic desorption (LIAD) method, we can increase the atoms flux (for both Rb and Na) for MOT loading by turning UV on at the beginning of each shot. Of course, this will degrade the vacuum condition in the chamber, however, after MOT loading, we turn off the UV, and the atom can be absorbed again by the chamber and then the vacuum recovers. The typical lifetime of Rb in the quadruple trap (QT) is 30 s level, and Optical-trap (OT) lifetime is about 20 s.

After atoms gradually accumulating within 30 seconds, Na and Rb MOT finally achieves saturation. To avoid collision between Rb and Na that induces an inelastic process, we use a resonance light to push the Rb MOT aside to avoid overlapping Na and Rb. That dual MOT typically can capture 10^9 Rb and 1.5×10^6 Na. To increase its density, we apply a compress-MOT (CMOT) process, which increases the restoring

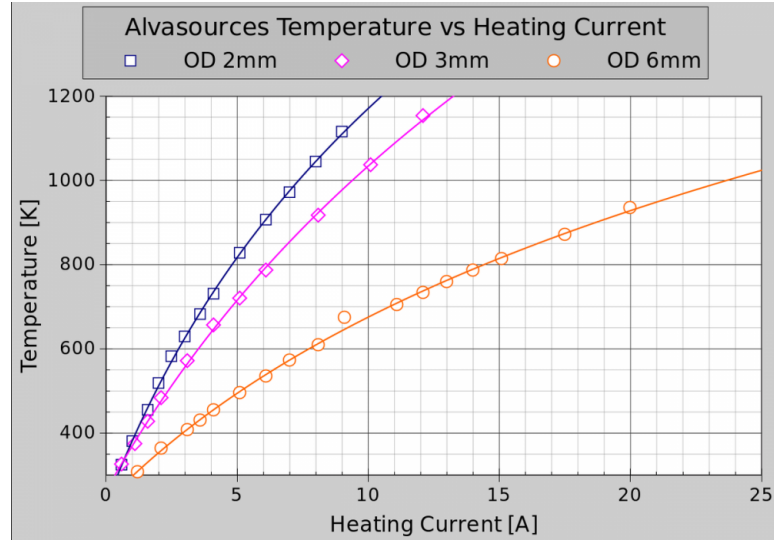


Figure 3.2: Temperature-current relationship of dispenser (Image from [alfavakuo](#)). The dispenser of Na and Rb are both with diameter of 3 mm.

force by far detuning the MOT laser¹. To further increase the phase space density (PSD) of the sample, a molasses process is implemented to cool the sample further. Finally, we load the sample into QT with both species in $|F = 1, m_F = -1\rangle$ state.

A pair of the anti-Helmholtz coil generates the Quadrupole trap (QT). At the beginning of the time sequence, the magnetic gradient is ramped up to 160 G/cm, served as a conservation trap for capture all atoms from the precooling stage. Then, we do the evaporation cooling for Rb which using a MW to pump atoms from $|F = 1, m_F = -1\rangle$ to $|F = 2, m_F = 0\rangle$. Due to the anti-trapping of $|F = 2, m_F = 0\rangle$ state, we can remove the high-temperature atoms away from the trap to decrease the overall sample temperature. Na atoms are sympathetically cooled by Rb. Due to Majorana loss bringing anti-evaporation effect, we add a single beam optical trap to shift the minimum position of the whole potential away from the QT centre. This works at the first evaporation stage and helps us obtain a sample with $20 \mu\text{K}$ temperature. After that, we adiabatically lower down the QT to 26 G/cm for avoiding severe Majorana loss

¹in our experiment, we do not increase the magnetic gradient.

further. After the MW sweeping to 6833 MHz, we finally achieve a mixture sample with temperature around several μK . This allows us to load them to an Optical dipole trap to do further cooling and experiment. More details about this hybrid trap can be found in this note of our lab [Xiong et al., 2013].

Optical trap evaporation is achieved by forcibly reducing the light intensity. In the later stage, the atomic density becomes lower due to the weakening of confinement, which reduces the collision rate, so a slower evaporation rate is required. As a result, the optical trap evaporation is relatively inefficient. Using 1070 crossed OT in our experiment, we typically spend 3 s to obtain a two-species BEC. For a one-dimensional optical trap, the evaporation time requires even longer and may take 5-10s. Therefore, we generally obtain BEC in the 1070 XOT first and then transfer it to other types of optical traps for experiments. Of course, the transfer process will inevitably bring excitation, so it is crucial to deceive an adiabatic process or wait a long enough time for reaching the ground state.

Since we need the Feshbach resonance between Na and Rb both in $|F = 1, m_F = 1\rangle$ state, we need transfer atoms from $|F = 1, m_F = -1\rangle$ to the target state. The easiest and most robust way is the adiabatic-rapid passage (ARP). By applying an RF(or MW) field to couple the initial and target state, we can detune its detuning from the blue (red) side to the red (blue) side. Following the dressed state, atoms start from $|F = 1, m_F = -1\rangle$ however end with $|F = 1, m_F = 1\rangle$. This procedure needs enough adiabaticity, which is time-consuming; however, it is robust from the system's power fluctuation and time precision. We carry out the transition under a low magnetic field, which enables us couple the $|F = 1, m_F = -1\rangle$ state to $|F = 1, m_F = 0\rangle$ and then to $|F = 1, m_F = 1\rangle$. For latter experiments that need $|F = 1, m_F = 0\rangle$, we can apply a relatively high magnetic field to decouple these two transitions. More details can be found in the previous thesis [Wang, 2016; Li, 2015, 2021].

In our experiment, Na has a relatively large interaction strength g_{Na} (even its

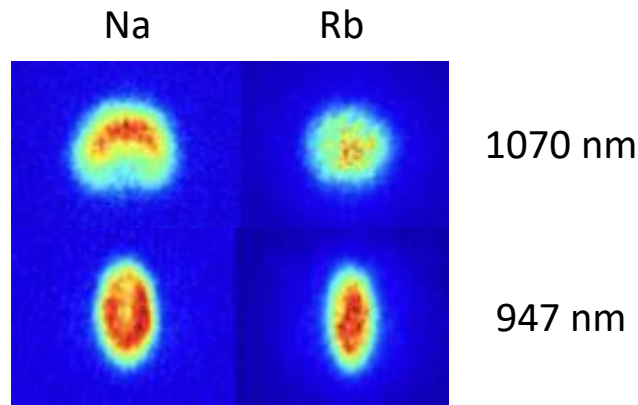


Figure 3.3: Na and Rb samples in 946 and 1070 nm ODT (image from [Li, 2021]). Due to gravitational sag difference, Na in 1070 ODT is buoyant above Rb. In 946 nm ODT, Rb stays at the centre of Na, showing the sag difference's excellent compensation.

scattering length is smaller than Rb, its mass three times smaller than Rb.), so at the beginning of OT evaporation, it is Na sympathetically cooling Rb. However, typically Na becomes BEC before Rb does because of a higher transition temperature, which is mainly due to the higher trap frequency of Na in the 1070 nm ODT. After that, the evaporation is mainly for the Rb sample, and we can achieve a two-species BEC with an almost balanced number at the final. This number ratio actually can be tuned by changing the evaporation ending in QT. For the double BEC sample in ODT, Na is immiscible with Rb in the case of a low magnetic field. Thus, Na shows a crescent shape which is because of the gravitational sag difference of two samples (shown in Fig. 3.3). In order to obtain a relatively pure BEC sample, we lower down the optical trap to a relatively shallow level, such as about 80 Hz for Na in 1070 ODT. We check the purity of the BEC sample by observing the BEC sample without any thermal part for whatever ToF. Then, we say that the sample is pure enough. However, to characterize the temperature of this sample, correspondingly the BEC fraction, is typically hard, which is beyond the range of this thesis.

In many experiments, we need to control the number ratio of Na and Rb. The

typical method is to adjust the optical trap's relative position to the QT's zero-point. By modifying this distance, we can determine the atomic number of Rb after the QT evaporation. Rb will be less evaporated and more Rb atoms remain for a longer distance, vice versa. Because the Na number is much less than Rb, with sympathetically cooled, the Na number mainly unchanges. However, the temperature will be the same as Rb. Subsequently, the evaporation of loading into OT is dominated by Na, as mentioned before. Therefore, the number ratio of Na and Rb can be manipulated by changing the number of the remaining Rb after QT evaporation.

As described in [Li, 2021], we build an optical trap with magic wavelength, which offers the same trap frequency for both Na and Rb. As shown in Fig. 3.3, Rb stays at the centre of Na. We can benefit a lot from this wavelength, such as increasing the overlap between Na and Rb and consequently increasing the Feshbach molecule's conversion rate or enhancing the signal of the polaron experiment. Our droplet experiment uses this sag-difference-free trap to achieve better overlap and form droplets with lower density and longer lifetime, which will be discussed in Chap. 5.

3.1.2 Producing Na-Rb Feshbach molecules

In our laboratory, the original intention of producing Feshbach molecules is to make the ground state molecule of NaRb further. After successfully making the ground state molecule [Guo et al., 2016], the mission of this machine becomes the study of heteronuclear mixture BEC. The core ingredient of research on this set-up consequently involves adjusting inter-particle interaction through the Feshbach resonance. Many interesting physics problems can be studied, such as Efimov state, polaron, spinor. Then the essential parameter is the FR parameter, i.e. how the scattering length of the inter-species changes with the magnetic field. The detailed calibration and calculation will be demonstrated in Chap. 4. We note that the scattering properties near resonance will be most affected by the shallowest bound state, so the preci-

sion measurement of the bound state will give accurate scattering properties in turn. Therefore, we need to synthesize FR molecules and study their properties.

Our experiment starts from an optically trapped ultracold mixture of ^{23}Na and ^{87}Rb atoms, both in their lowest hyperfine state $|F = 1, m_F = 1\rangle$ [Wang et al., 2013, 2015a; Jia et al., 2020]. Magnetoassociation starts from an initial magnetic field of 350 G, just above the FR at $B_0 = 347.64$ G. The magnetic field is ramped down across the resonance to form FMs, and then to 335.6 G. At this field, the FMs have a nearly zero magnetic dipole moment; this allows us to remove the residual atoms with a short and strong magnetic field gradient without losing molecules. Afterwards, the magnetic field is ramped up to a range of target values below B_0 for further experiments. Following this procedure, we can routinely obtain a pure sample of $^{23}\text{Na}^{87}\text{Rb}$ FMs with a typical temperature of 300 nK and a trap lifetime of more than 30 ms. This short lifetime is due to near-resonance photon scattering by the 947 nm optical trap light [Guo et al., 2017; Jia et al., 2020], which is provided by a home-built diode laser system. In another experiment on $^{23}\text{Na}^{87}\text{Rb}$, in which a single-frequency 1064 nm laser is used as the optical trap light, FM lifetimes greater than 100 ms have been observed [Wang et al., 2019; Guo et al., 2021a]. Nevertheless, the current lifetime is more than enough for the present work, as we need only 10 ms for magnetic field stabilization and less than 1 ms for dissociation.

3.2 Image system upgrades

The previous image system is composed of an f=100mm (#49360-INK) and f=300 mm (#49368-INK) pair from Edmund optics, which can support a resolution of about $3 \mu\text{m}$ (N.A.=0.13) as shown in Fig. 3.4. This imaging system is built with discrete elements, which cannot move as a whole. Thus, it is only proper for imaging for a small region; otherwise, both spherical aberration and coma shows up if moving only the camera

or the lens set. We need to do the ToF for samples for the droplet experiment, and the displacement reaches about 2 mm. If we change the camera position, the resolution for imaging sample with large displacement, i.e. at the edge of field-of-view, will be degraded. So, we improved our resolution by two means: First, we increase the imaging system's resolution by using a long working distance objective; secondly, we build a whole block by mounting all optical elements and cameras onto an electric translation stage. In the rest of this section, we discuss the absorption image method for a dense atomic cloud, introduce a high-magnetic-field image scheme, and discuss the number calibration method.

3.2.1 High resolution image system

The characteristic length for a droplet is typical of several μm , as shown in Sec. 5. In order to resolve this tiny sample, we need a better imaging system with resolution reaching μm level. The old imaging system with an $f=100\text{mm}$ objective is not enough since its N.A. is 0.13 with an airy radius of about $4 \mu\text{m}$. So, we use an objective with a shorter focal length to increase N.A. The most convenient way is using a microscope with a long working distance. So, we choose a 10X Mitutoyo plan-apo infinity-corrected Long-WD objective with an effective focal length of 20 mm. Its working distance reaches 34 mm, enough for our application without blocking any optical path, such as MOT or optical trap. We can use the same eyepiece (Edmund #49368) with $f=300$ mm and directly image the atom onto the camera thanks to the infinity-correction property.

As shown in Fig. 3.5, We use the cage system from Thorlabs to build the main body of the imaging system. A 45° mirror reflects the probe beam in the vertical direction. This avoids the diffraction light from optical dipole trap scattering to CCD and affects the image quality. The dichromatic mirror can be tuned to ensure the Na image is at the centre of Na CCD. Moreover, we add a ring adjuster for Rb CCD to

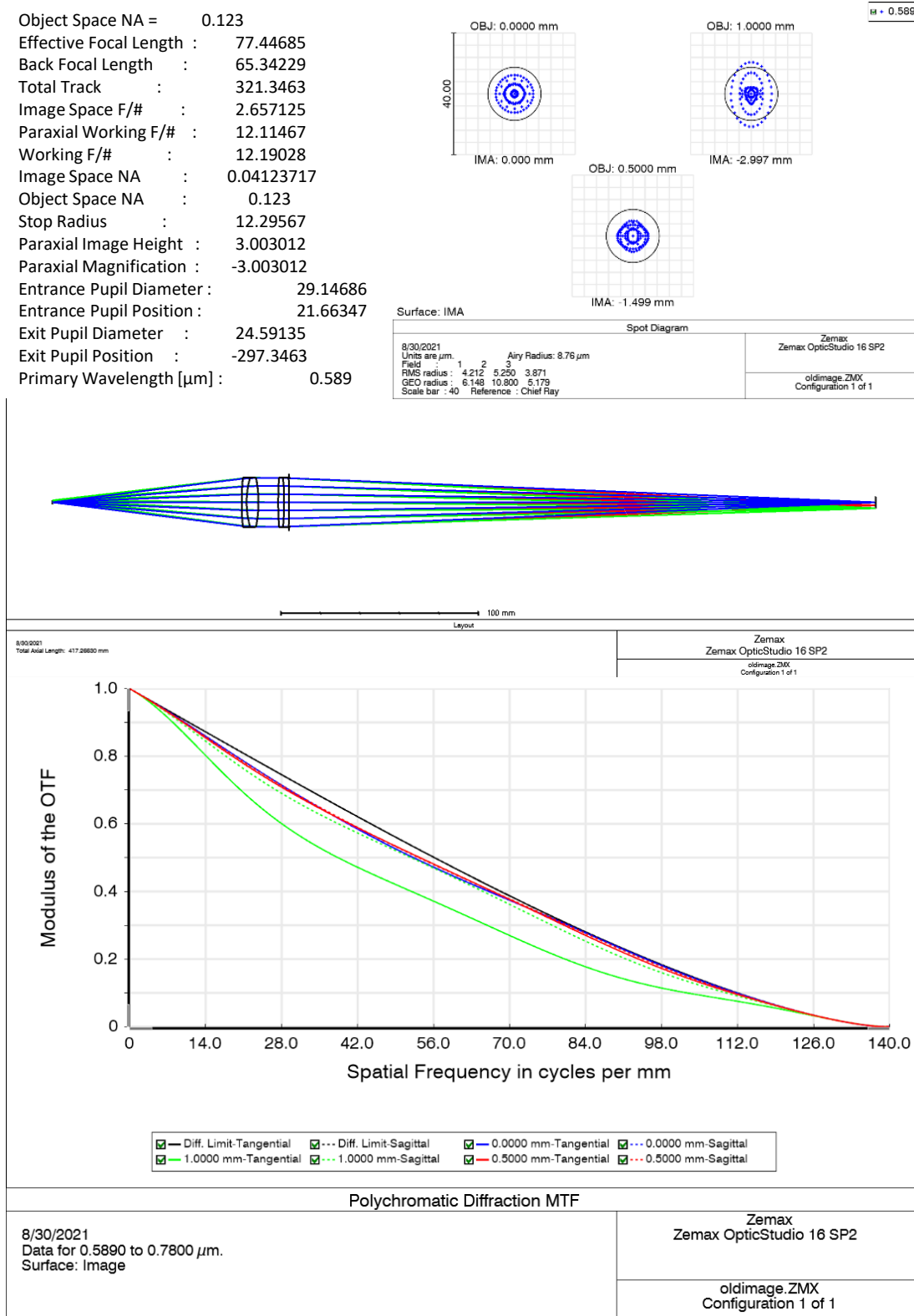


Figure 3.4: 3x image system simulation by Zemax. From the spot diagram and MTF calculation, we can read out a large field-of-view of this system.

fine-tune its position. This is mainly for focusing on both Na and Rb. Because there always be a chromatic shift for two different wavelengths (589 nm for Na and 780 nm for Rb). So, when focusing on the system, we first focus the Na by move the set-up as a whole, i.e. move the objective on focus to the atom. Then, we tune the ring adjuster to focus Rb onto the camera. One mistake is that we choose an adjuster too fine (4 mm for ten turns), so the adjustment procedure typical take a long time. As mentioned before, the whole system is mounted onto an electric translation stage controlled by an Arduino. Code and control can be found in Lintao's thesis [Li, 2021].

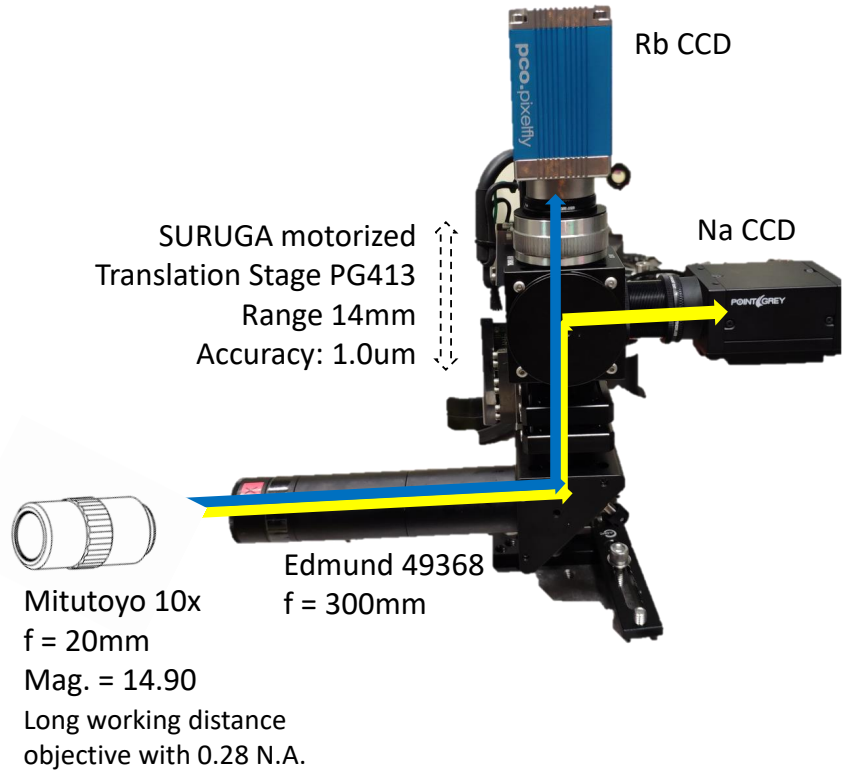


Figure 3.5: New compact imaging system. The whole set-up is mounted on a electric translation stage from SURUGA. The objective can be switched between a Mitutoyo 10x microscope and a typical $f=100$ mm achromatic lens. Then follows a $f=300$ mm eyepiece for focusing. A dichromatic mirror splits Rb and Na probe into two CCDs.

Even though we use a powerful objective with an Airy radius of $1 \mu\text{m}$, there ex-

ists a critical issue that the cell wall is 3 mm thick. So, we need to check the imaging system's performance with this 3 mm window before the objective. We did not do any correction for this glass wall because our primary goal is to increase the magnification. Even the resolution only increase twice will be enough for observing droplet signals. The 3 mm window will decrease the resolution². Since when the focused beam goes through the glass wall, light with a different angle will bend by different amplitude and finally, they cannot converge to a single point as without the glass. This effect is severe when the N.A. goes higher.

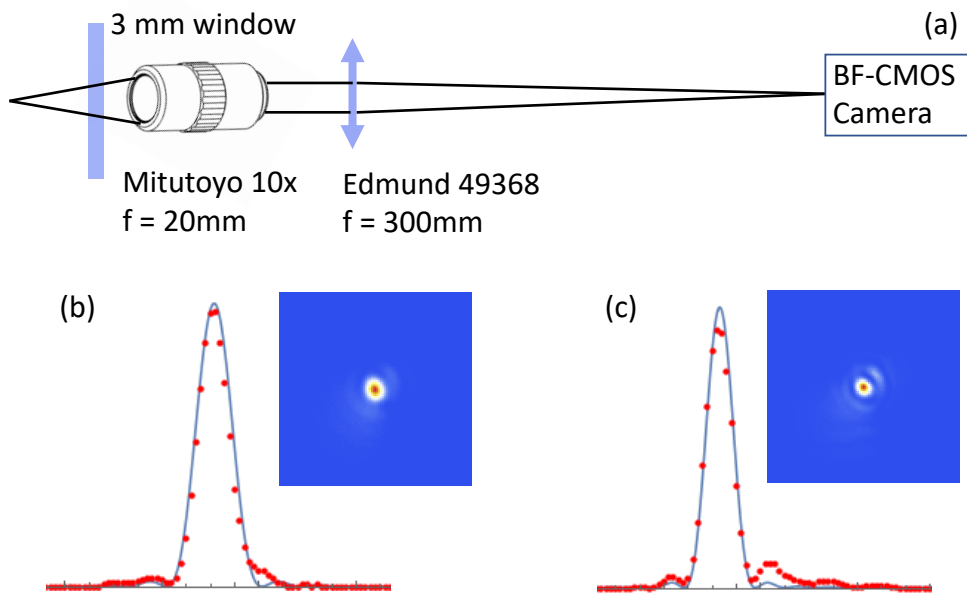


Figure 3.6: Image resolution test of 15x image system. (a) shows the test method. a 2 μm pin-hole is used as target. Image is taken by a pixel-size 3.45 μm Blackfly CMOS camera. (b) and (c) shows the airy disk we measured for Rb and Na.

Before putting it online, we first test its resolution offline with a USAF1951 target and 2 μm pinhole. Here, we show the measured Airy disk in Fig. 3.6. By simply fitting the pattern with the Airy function, we get the resolution for Na(Rb) is 1.7(2.3)

²A tutorial for standard object correction ring can be found [here](#). Moreover, the effects of thick glass on an imaging system can be found on [Thorlabs](#) under the tag of correction collar

μm . So we now have a high resolution and commercial and cheap image system.

Because we will do ToF measurement for several tens of ms, i.e. about 2 mm away from the centre of view-of-field, spherical aberration and coma can worsen the image quality. This can be shown by Zemax by a tilted angle of input light (Fig. 3.6). We use a high magnification imaging system with a short focal length of 20 mm. This makes its field-of-view very small. So, we need to move the whole imaging system along with the atomic sample. So, we build the imaging system very compact and mount it onto a translation stage controlled by a computer. The translation stage is mounted vertically with a step resolution of $1 \mu\text{m}$. We use an Arduino board to control the driver. Finally, we can change the position of our image system at will shot by shot. To avoid the movement changing affecting the EM field around the cell, we make each movement at the interval of two shots.

3.2.2 High magnetic field absorption image

To probe the droplet without distortion, we need the imaging scheme reliable, which means the method can recover the density profile of the sample as accurate as possible. Since a typical droplet sample has OD above 50 for Rb and 10 for Na, a typical absorption image method cannot be used directly, which is because the absorption image's SNR is limited when the sample OD is too high. As plotted in Fig. 3.7, weak probe intensity (less than one saturation intensity) can only support OD smaller than 3 [Guo, 2021]. Increasing the probe intensity to achieve the saturation absorption image can increase the threshold of OD to probe. However, higher intensity could cause several other problems: first, calibration could be hard to do or cause a significant error because the nonlinear response of the absorption. second, for a high density sample the re-scattering problem could introduce the effect beyond the aforementioned theory. So, we conceive a partial pumping method and a high-magnetic field absorption imaging scheme for the high-OD samples.

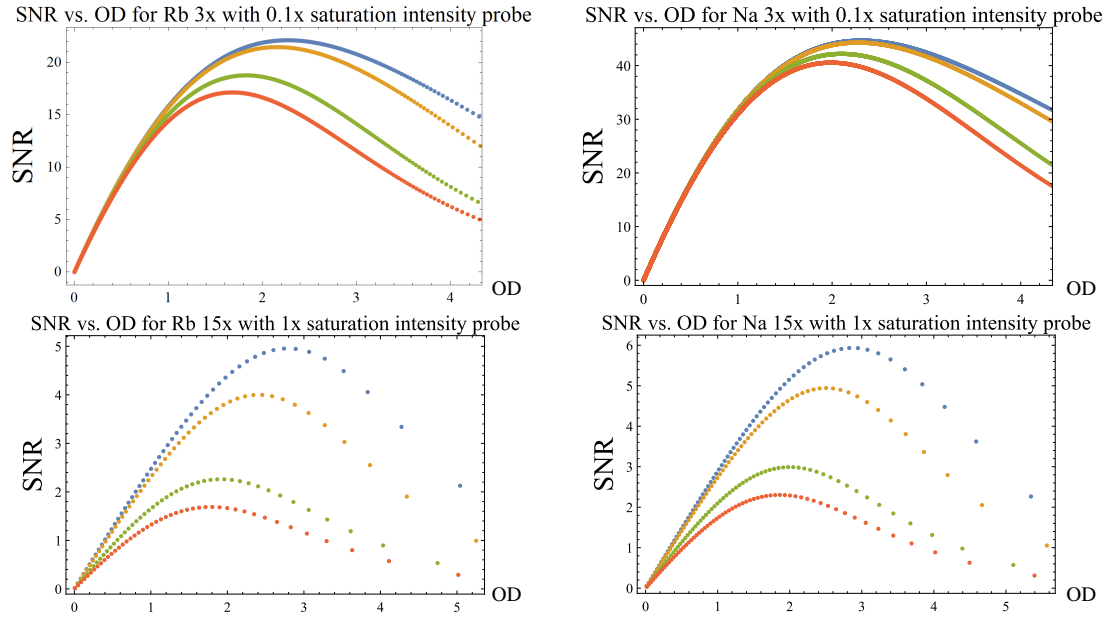


Figure 3.7: SNR of absorption image as a function of OD. Above two panels are our 3x image system, and Lower two panels are our 15x image system. Blue dots for PCO-sCMOS camera; yellow dots for BFS-PGE-31S4; green dots for PCO double-image camera; orange dots for Pointgrey 51S5.

Thus, we first decrease the sample's density; however, we keep its profile unchanged. Then, we apply the typical absorption image. This is what we called the partial pumping method for absorption image. A typical way to pump a small portion of the sample to the image transition is by MW or light. As shown in Fig. 3.5, our sample is at $|F = 1, m_F = 1\rangle$ state, which is non reacting with the absorption light. Then, we use a pumping laser to pump atoms to exited state $|m_J = 1/2, m_I = 3/2\rangle$; then, with spontaneous radiation, atoms accumulate onto $|F = 2, m_F = 2\rangle$ state. Finally, we use the cycling transition from this state to $|m_J = 3/2, m_I = 3/2\rangle$ state to do the absorption image. Here the pumping can also be done by the MW pulse. However, our original MW had a Rabi freq less than 10 kHz, which could consume 100 μ s or even longer apply a π pulse. This would make the sample's shape changed a lot when we probe it by the image light. We will get back to this point when we discuss

our upgrades of the Full-wave loop-antenna in Sec. 3.5.2.

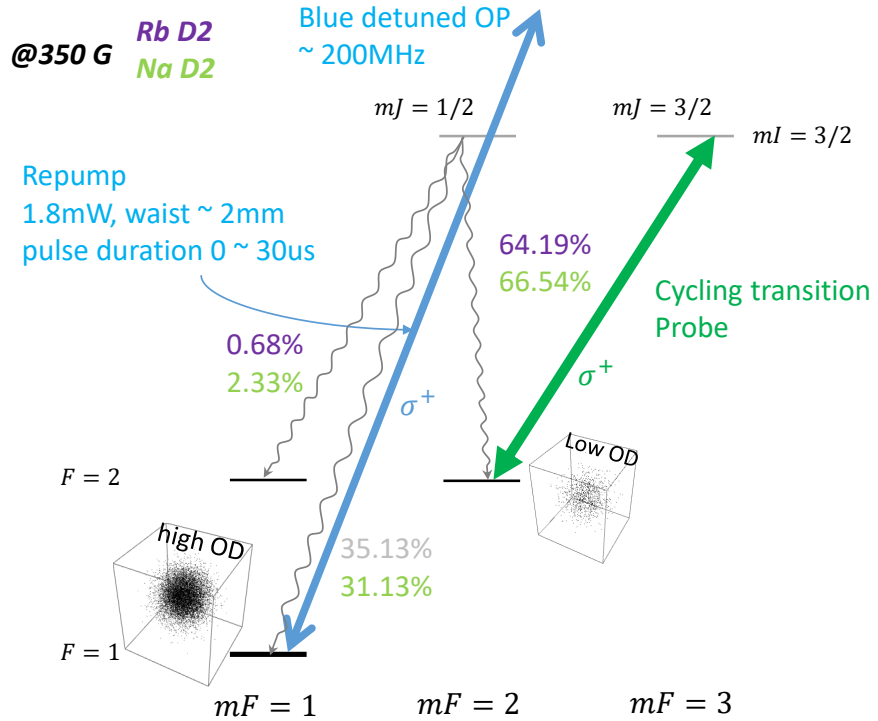


Figure 3.8: image scheme for Na(Rb) $|F = 1, m_F = 1\rangle$ state under 350 G magnetic field. The ground states are labelled with F and m_F ; the excited states are labelled with m_J and m_I . The imaging procedure is divided into two steps: first, pumping atoms from $|F = 1, m_F = 1\rangle$ to $|m_J = 1/2, m_I = 3/2\rangle$. After atoms accumulating to $|F = 2, m_F = 2\rangle$ state, we drive the cycling transition for absorption image. By blue detuning about 200 MHz of the pumping light, we can control the OD for the image transition.

So, we choose the pumping laser instead of tuned to on resonance, and we make it large detuned away from the transition and make its intensity high. This method ensures the whole sample feel around the same intensity because large detuning and intensity make the atoms only absorb a tiny portion of the light. Even for a very dense sample, the unevenness of the saturation effect can be avoided. As plotted in Fig. 3.8, Na partial pumping a small portion of the sample to $|F = 2, m_F = 2\rangle$ state, which

then can be detected directly. The pumping ratio can be controlled by the duration of the pumping laser. As shown in Fig. 3.9, the OD of pumped Na atoms as a function of the pumping duration is plotted. We can see that we have an almost linear pumping speed for the first several tens of us, and after 50 μs we have a saturation effect. This saturation effect is used to calibrate latterly. For our experiment, to decrease the OD to less than 3, we typical using a detuning 200-300 MHz and pumping only several μs to achieve a portion less than 10 per cent. Then a typical low-intensity absorption image can afford it.

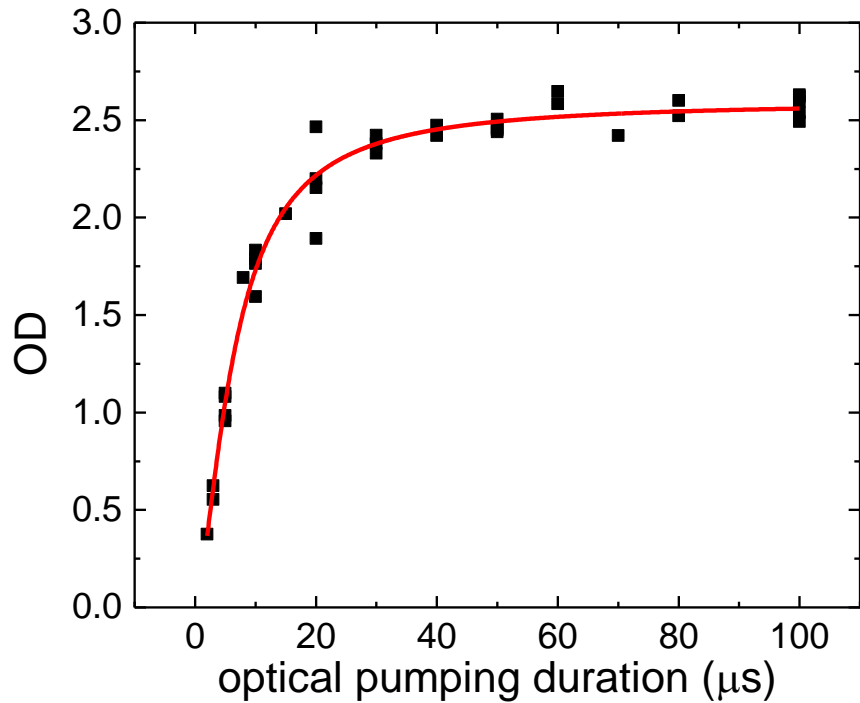


Figure 3.9: Partial pumping portion as a function of pump duration. Here shows the partial pumping for Na with 200 MHz blue detuning of the pumping light.

3.2.3 Atomic number calibration

In the previous subsection 3.2.2, in order to perform absorption imaging on samples with higher optical density (OD), we use the partial pumping method to reduce its OD. However, in order to ensure the signal-to-noise ratio of the imaging, we usually do not use the probe light whose intensity is much smaller than the saturation intensity. Therefore, considering that the droplet experiment requires atomic number measurement, we need to do a more careful atomic number calibration for our high field absorption imaging. The principle of calibration is mainly derived from the calibration of several parameters in absorption imaging. For now weak probe light intensity, the expression of absorption imaging is

$$\frac{dI(x, y)}{dz} = -n(x, y, z)\sigma_{eff}(\delta, I, others)I(x, y) \quad (3.1)$$

In above formula, σ_{eff} represents the effective cross-section of atoms, which is related to probe detuning, intensity and other parameters such as polarization. By separating intensity and detuning, we have

$$\sigma_{eff}(\delta, I, others) = \frac{\sigma^*(others)}{(1 + (\frac{2\delta}{\Gamma})^2) + \frac{I}{I_{sat}^*(others)}} \quad (3.2)$$

Probe light transmits along the z direction and has a distribution in x - y plane. $n(x, y, z)$ is density distribution of a bulk sample. When we do absorption image, we actually probe the column density

$$\int n(x, y, z)dz = \frac{OD(x, y)}{\sigma^*(others)} = \frac{1}{\sigma^*(others)}[\ln(\frac{I_{in}}{I_{out}}) + \frac{I_{in} - I_{out}}{I_{sat}^*(others)}] \quad (3.3)$$

Thus, in the following calibration, we mainly calibrate two parameters: $I_{sat}^*(others)$ and $\sigma^*(others)$.

First, we follow [Reinaudi et al., 2007] to calibrate $I_{sat}^*(others)$, which we called

it β -calibration. We define

$$I_{sat}^*(others) = \beta I_{sat}^0 \quad (3.4)$$

where $I_{sat}^0 = \frac{\hbar\omega A_{21}}{2\sigma_0}$ is the ideal saturation intensity. To calibrate the beta, we use different camera light intensities to probe the same sample and then directly plot the od without correlation, i.e. $\ln(\frac{I_{in}}{I_{out}})$. As shown in Fig. 3.10, the y-axis represents the counting rate of probe light which is proportional to light intensity I_{in} ; x-axis is the od without correction we mentioned before. Via formula 3.3 We can fit this curve and then get CR_{sat}^{eff} . We use counting rate instead of light intensity, mainly because CR can be read directly on the camera. Using the effective saturated CR to obtain the corrected od is more directly than using β . In other words, for the correction of imaging, we don't actually care about the value of β , and it is actually enough to have saturated CR. Finally, in Table. 3.1, we offer the effective saturated CR of Na and Rb in the two different image systems we used. At the same time, we point out here that the β value depends on various parameters, including light polarization, camera parameters, projection parameters of the imaging system, etc. Therefore, the number calibration of each system should be done separately. Through this engineering method, all unexpected parameters are absorbed into a single variable.

The above calibration for saturated light intensity avoids the OD change of the sample from different probe intensities. However, considering the expression 3.3, in order to obtain the column density distribution of the sample, we also need an effective scattering cross-section σ_{eff} . In order to obtain this parameter, we need to compare the OD obtained by absorption image to the column density of the actual atom density distribution. The point to be emphasized here is that we do not use the parameters in the β -calibration to correct the cross-section because of light imperfection, such as polarization, etc. The two are not entirely consistent. On the other hand, we use the partial pumping method. Therefore, we hope that this effective cross-section parameter can absorb the imperfection of pumping, such as leakage to

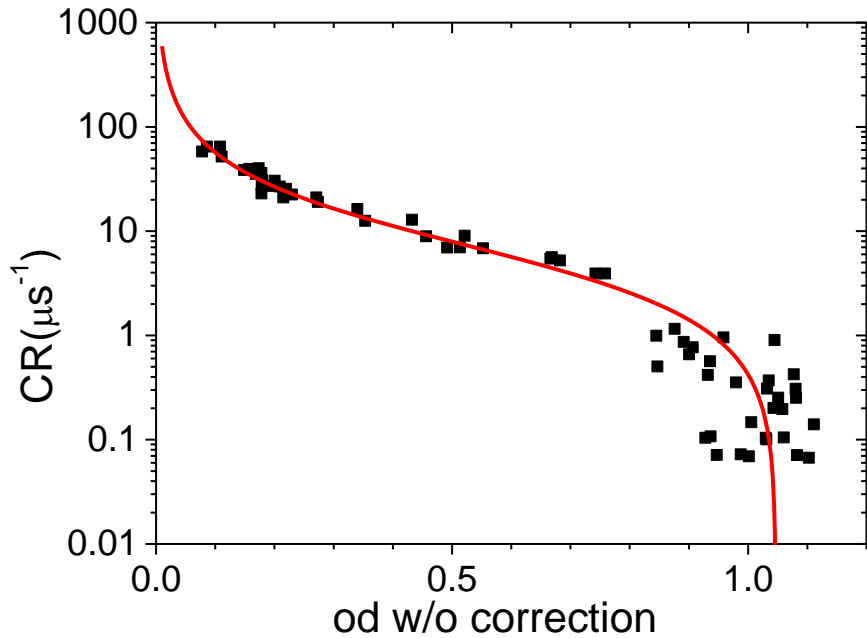


Figure 3.10: β -calibration of Rb 15x absorption image. CR is counting rate, i.e. average counting over probe duration. od w/o correction is $\ln(I_{in}/I_{out})$ without correcting the saturation effect.

the other states, which does not result in 100% pumping. We put this part of the calibration into the alpha. This part will not affect the saturation intensity of the probe but will affect the number of atoms counted at the end.

For α -calibration, we define

$$\sigma^*(others) = \frac{1}{\alpha} \sigma_{sat}^0 \quad (3.5)$$

Two methods can be used: one is from [Hung, 2011], which directly compare the density distribution of BEC in-trap with, and directly compare the density distribution of the atom calculated by trap freq with the OD distribution obtained from the photo to obtain the corresponding α -coefficient. The other is the number of atoms obtained through the BEC-thermal phase transition and the thermal part's temperature mea-

	Image system	Mag. field	Probe polar.	OP det.	CR_{sat}^{eff}	I_{sat} (mW/cm ²)	β	α
Rb	3x	LF	Circular	0 MHz	87(4)	2.792	1.67	1.59
Rb	15x	HF	Horizo.	0 MHz	5.7(3)	5.421	3.25	3.75
Rb	15x	HF	Horizo.	215MHz	5.7(3)	5.421	3.25	4.54
Na	3x	LF	Circular	0 MHz	288(5)	5.862	0.95	
Na	15x	HF	Horizo.	140 MHz	24(1)			3.76

Table 3.1: Summary of image calibration

surement. The corresponding alpha coefficient is obtained by comparing the total OD measured by the photo. The former method is more feasible for a sample with a larger in-trap size because the in-trap sample is typical μm level, which is difficult to avoid the impact due to the imaging resolution. The latter method can avoid this problem because the measurement of the total atomic number can be obtained from longer ToF. Therefore, in our experiment, we finally adopted the latter one.

In general, through the above two steps, we can accurately obtain the density distribution of the atom. Adding the high-field imaging method introduced in the Subsec. 3.2.2, we finally offer a complete imaging plan for the droplet experiment. This solution is also suitable for in-situ imaging samples with relatively high OD, such as in-trap BEC, bright solitons, etc. Furthermore, achieving enough resolution by upgrading the imaging system is essential as another aspect of the requirement to retrieve density distribution.

3.3 CAMIMA: a multi-camera and image process platform

CAMIMA is a multi-camera control platform with image processing functions. Thanks to various camera adaptors provided by the Image Acquisition Toolbox in MATLAB, CAMIMA can support multiple types of camera, including USB cameras from Point-

Grey, PCO and Migtex, Web camera and other general type of cameras. The primary time sequence is tailored for the absorption image for the cold atom experiment. However, it is very convenient to switch to other sequences such as fluorescence imaging. After acquiring images from the camera, there are extendable and programmable image processing functions for post-processing images. Users can easily re-program the time sequence and processing sequence for various scenarios, e.g. denoising or de-fringe process, fluorescence image and so on.

The software is made of four parts:

- CAMIMA: Main control for converting data from different camera to a uniform image stream, which easier for following processing.
- VUIMA: For showing and processing images from each image stream. VUIMA can be opened multiple.
- CAMSET: Setting program for various cameras. Inside it, there is a general setting panel adaptation for specific type of camera.
- FITSET: For general purpose fitting progress. fitting function can be edited as will.

3.3.1 licensing, versions and updates

This programs is a free software: you can redistribute them and/or modify them under the terms of the GNU General Public License, version 3, as published by the Free Software Foundation. The full text of the license is available from <https://www.gnu.org/licenses/> and is included in the file COPYING included in the distribution.

For adapting different version of MATLAB and its Appdesigner toolbox, CAMIMA can run under following versions:

- MATLAB2016
- MATLAB2020

Software downloads and updates are made available via github:

- <https://github.com/guozc12/CAMIMA>

3.3.2 Using the software: a basic guide

Prerequisites

Before installing CAMIMA, one need to install MATLAB with a version later than 2016. The listed several add-ons are needed.

- MATLAB (later than Ver. 2016)
- Appdesigner™ in MATLAB
- Image Acquisition Toolbox™ in MATLAB
- uitree in MATLAB

Start CAMIMA

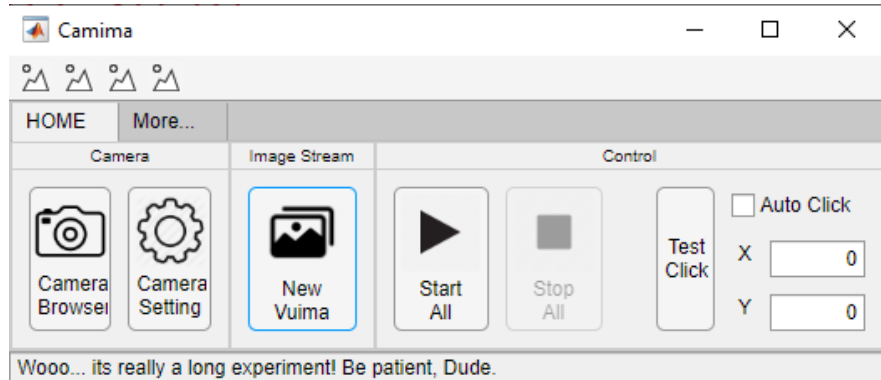


Figure 3.11: CAMIMA Main panel.

Open the CAMIMA.mlapp in Appdesigner. Then click the Run button to run the main CAMIMA program. As shown in Fig. 3.11, a small panel shows you entrances for different functions:

- Camera Browser: Open a new panel for searching and initializing all installed cameras. (As shown in Fig. 3.12)

- Camera Setting: Open a new panel (CAMSET) to control each camera directly. (Fig. 3.13)
- New VUIMA: Open an image processing panel (VUIMA) for viewing images and automatic image processing. (Fig. 3.14)
- Start All: For quick starting everything, including start acquisition for every camera
- Stop All: For quick stopping everything.
- Test Click: for setting a button, click after each shot with the written position on the right side.

Setting cameras by CAMSET

As shown in Fig. 3.13, after catching each camera, we can control the camera manually, such as previewing, get a snap by the manual trigger and setting various parameters controlling the camera. For cameras from different vendors, the general settings are different. Thus, we generate a list in a new window, as shown in the right panel of Fig. 3.13. Users can change the private properties of the camera, such as exposure time, binning and other higher-level parameters. The ROI (Region-of-interest) can only be set when the camera is stopped as shown in the right-middle of CAMSET panel. Parameters for automatic triggering can be set in the right-bottom panel of the CAMSET window. By the way, as we mentioned before, our program can support various types of cameras which is listed as follows:

- PointGrey USB camera
- BlackFly USB camera
- PCO USB camera
- camera with GIGE (web cam)
- other general types of camera

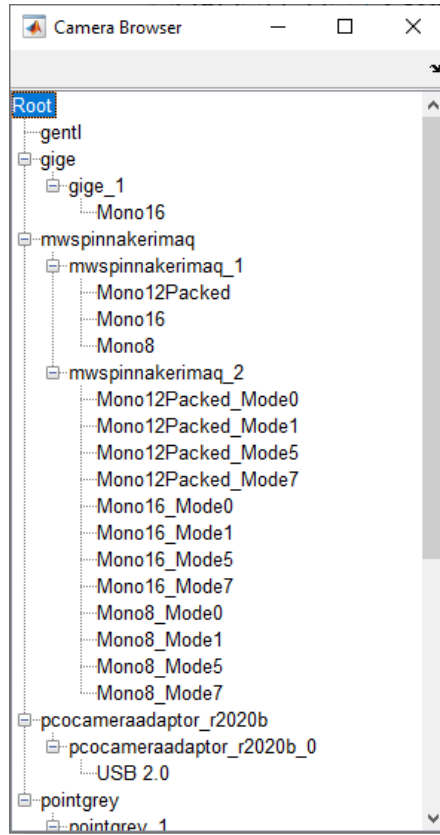


Figure 3.12: CamTree shows all available cameras for acquiring images. When click the “Camera Browser” button in CAMIMA main panel, this tree window pops up and show you a full list of all available cameras.

Image acquisition

After configuring the camera, the platform is ready for automatic image acquisition. By setting the trigger, we can integrate the camera as part of the control system. For absorption imaging, we take three pictures for each imaging, which is achieved by setting three triggers to the camera. The picture will be temporarily cached in memory. Trigger the event by setting the number of triggers. For example, after receiving three triggers, start processing the absorption imaging picture and calculate the OD picture. For specific details of absorption imaging, please refer to that section.

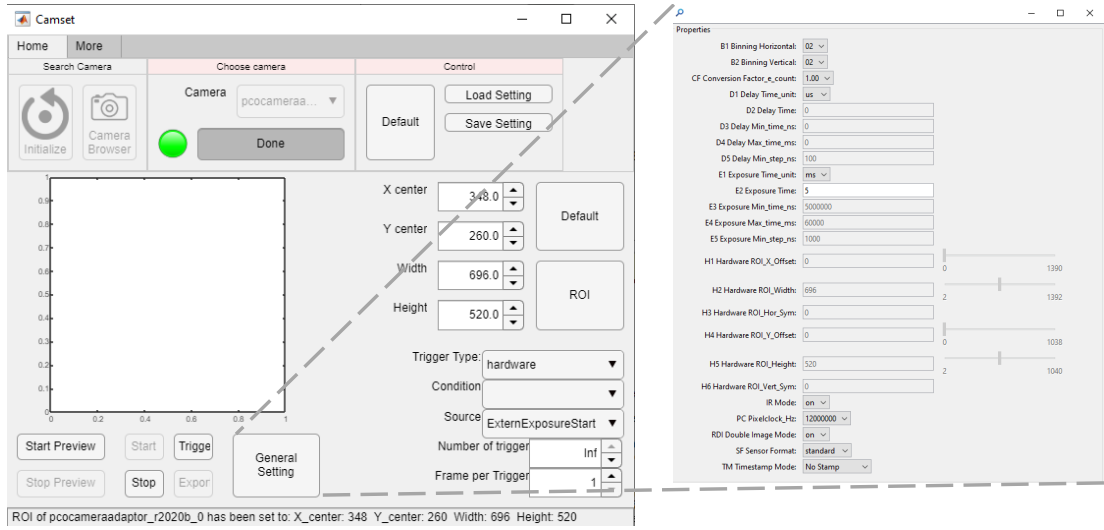


Figure 3.13: CAMSET is a module of CAMIMA used to control and set cameras. By switching the toggle, one can control multiple cameras. Besides the general setting, such as ROI and acquisition sequence, it also offers a specific entrance for each camera.

When we have multiple cameras that need acquisition data, each camera can complete the data collection independently.

Some cameras, such as PCO, have a double image. Then, we need to divide the data collected by the camera. In order to ensure the versatility of subsequent image processing and avoid the need for different codes for different cameras, we use an adaptor to convert the raw data from cameras to independent image streams. The settings of the camera and the acquisition of the camera are in the *camera stream*. Then it generates image streams. For example, a single imaging camera only provides one image stream, while a PCO double-image camera can provide two image streams. Select a specific image stream to do subsequent processing. In this way, we can say that a specific image stream is displayed in a window, i.e. VUIMA.

One VUIMA is connected to one image stream. Users can select the existing image stream in the link in the upper left corner of the VUIMA panel. As the collected images

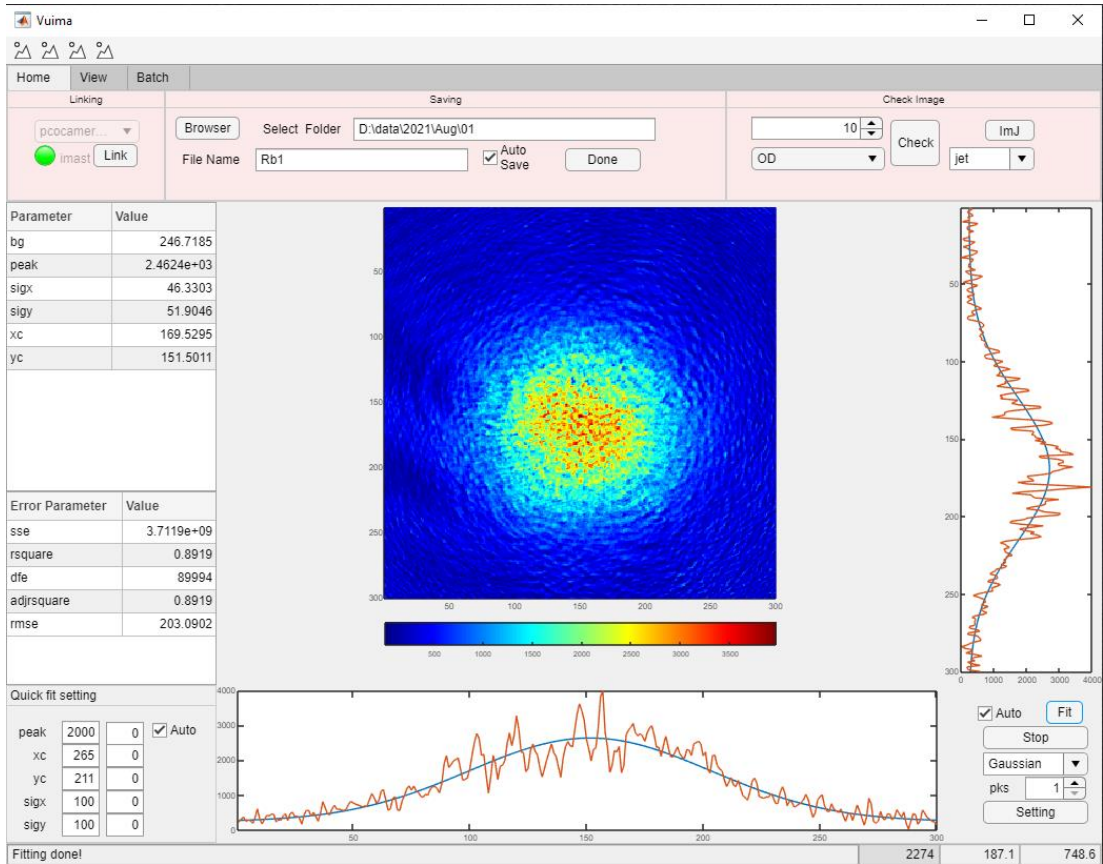


Figure 3.14: VUIMA is a module of CAMIMA used to preview image. The VUIMA window can be opened multiple for each image stream. Besides previewing the image, it can show the fitting results comparing to the raw data. It offers entrance for setting arbitrary fitting function.

are generated, VUIMA is responsible for pre-processing the images. The statistical data will be given in the lower right corner, including the number of photons in pure light photos, by setting the exposure time, calculating the light intensity, and giving a preliminary count. For the three images collected, the data needs to be cleaned first. VUIMA first removes abnormal points and take average around them. Then it processes the OD images. Because the Log function is used, in order to avoid too many abnormal values, we adopt the cut-Log method to treat points with OD smaller than -0.2 as 0. This works for most pictures and can detect abnormal cases when sometimes

the trigger is broken. For some pictures with a low signal-to-noise ratio, this limit can be modified to a lower value to ensure the authenticity of the data. Subsequently, the processed OD picture will be displayed in the middlebox, and fitting will be carried out simultaneously. The fitting result displays on the right and bottom of Vuima, in the form of slices along with the raw data points. The specific fitting will be introduced in the next section.

post processing of image

We first perform preliminary fitting on the collected pictures. The fitting function can be selected in the panel in the lower right corner of VUIMA. Thermal sample adopts 2D-Gaussian, BEC adopts parabola and so on. Multiple peaks can be selected. For mixed samples, one can choose a mixed model. At the same time, a user-defined module can be opened in the FITSET window. The general fitting takes typical 3-10 seconds, which can ensure that the analysis result can be obtained immediately and the decision can be made within a shot. Of course, Users can try to increase this speed. For the peak model, whether single-peak or multi-peak, one can manually select the initial value or automatically select the initial value. You can see the initial value selection in the lower-left corner of the Vuima panel. As the peak increases, more blanks can be added. The fitting result will also be stored in a CSV file for real-time import to the origin to give further analysis, such as temperature, number, density, and other parameters. At the same time, it is very convenient to compare multiple shots, draw pictures, etc.

The fitting data is first displayed in the table on the left. Users can get fitting errors by sliding the form to the left. In addition, indicators such as r-square value are given in the middle on the left. Adj-square is used to indicate which model is better to use when the model is not clear. In order to facilitate the data analysis after the experiment, Vuima has developed a batch processing module for batch processing of

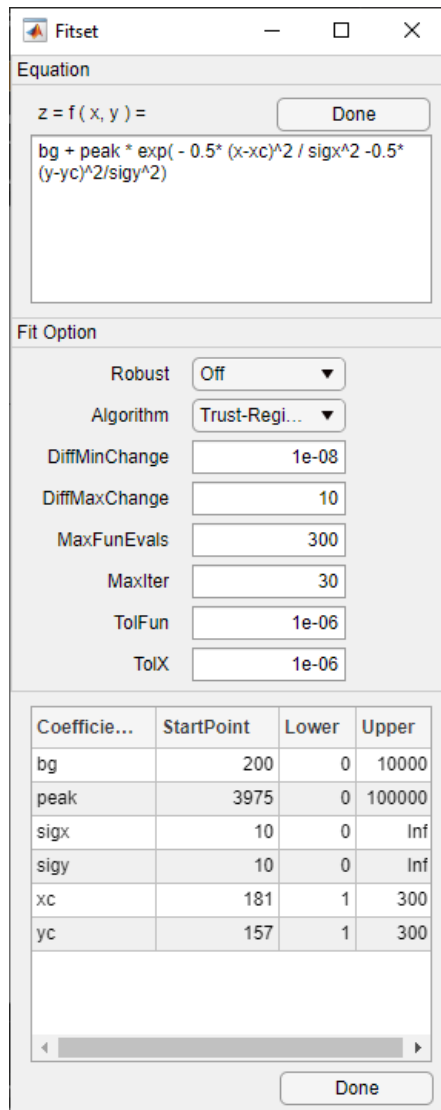


Figure 3.15: FITSET is a module of CAMIMA used to set arbitrary fitting function. Besides the default fitting functions written under the toggle button, this module offers function for easily generate arbitrary fitting function.

a large number of pictures. Because of the convenience of programming, this function has a high degree of freedom, and users can freely add the codes they want to process in the module.

3.3.3 Vision and outlooks

From the perspective of experimental physics, there are two primary purposes for using or developing new technologies: The first is to detect physical quantities that were previously undetectable through technological advancement. The second is to improve the efficiency of experiments and work through technological advancement. The former makes the frontiers of experimental physics one step forward, while the latter can make experiments one step further away from industrialization. Cold atom physics has been developed for more than two decades. Nowadays, with the rise of quantum computing, it is time to consider further substituting industrialization methods into experimental research to pave the way for research-industry transformation.

Strictly speaking, CAMIMA is only the second half of the entire cold atom experiment timing system, which is the data acquisition part. A complete experiment sequence system should be able to record all the data of each experiment: including sequence setting parameters, checking and testing parameters. Generally, we will focus the laboratory data on only what we want to control, such as a specific frequency or power, and what we want to see, such as absorption imaging pictures. However, all measured quantities are part of the experiment. A complete record has two advantages: First, a complete record includes complete monitoring, which can avoid out-of-control conditions. Second, a complete record can make the data of each shot more valuable. For example, the data collected on different days is comparable. Through systematic data analysis, there will be unpredictable discoveries. Furthermore, these are inseparable from introducing new, efficient data acquisition technology and data analysis and processing technology. In general, martial arts in the world can only be

broken quickly. The pursuit of efficiency is the eternal theme of science and research.

3.4 Fast magnetic field control

As we mentioned in the section about Feshbach resonance, by tuning the magnetic field, we can easily control the scattering properties of atoms, i.e. the interaction strength. In the previous set-up, we use a large Helmholtz coil with 70 turns. The coil's inductance is three mH, which is huge, introducing a significant time constant. So, even using a driver with 100V(check), we will have a rising slope of about 1 ms, which is not fast enough for our requirement to control the interaction. Our request depends on the time scale of the research object. For example, a typical BEC with a scattering length of $100 a_0$ order will have a time scale of less than 1 ms. Thus, we need a new magnetic field control system with the time scale of μs level to control the interaction fast. Then we can make sure the sample's size of other parameters changing much slower than the interaction changes.

So, with the above request, we need to build another coil that can generate a small but fast magnetic field. The limitation is the coil's inductance, so we reduce its turns to as few as possible. However, with fewer turns, the magnetic field can generate a less magnetic field. So we need to make a trade-off here. Finally, we choose a diameter 60 mm coil pair with six turns for each one. Also, to generate a larger magnetic field, we put it as close as possible to the cell. The set-up with the main Feshbach coil is shown in Fig. 3.17. To adapt our previous large coil, we designed a holder made of polyvinyl as shown in 3.16. Moreover, the holder winding with the fast coil is inserted into the 2-inch optical path to avoid blocking the MOT beam.

To drive this fast coil, we need a current driver that fast turns on/off and makes a precision control of the current with tiny leaking current. So, with Lintao's help, we design a fast coil driver with two groups of JFET. Each group is several JFETs set

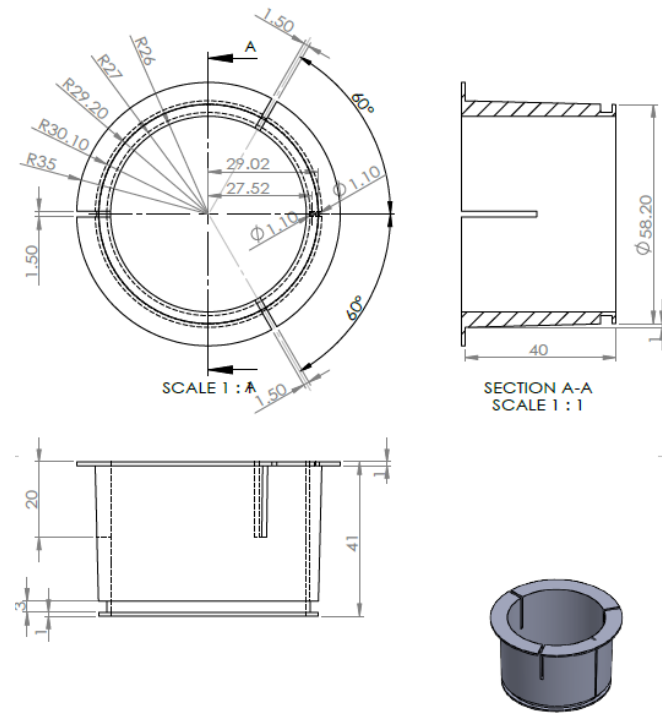


Figure 3.16: Fast coil holder for adapted to existing main coil system.

in cascade. This design uses the intrinsic fast-changing property of JFET compared to MOSFET, which typically possesses large junction capacitance. Also, cascade sets of JFETs can reduce the leak current from the base since after several levels the current in the base can be reduced to μA level or even better. The driver schematic and simulation by Tina-TI can be found in the appendix. [A](#).

Two parts of the fast coil are put as close as possible to avoid introducing more curvature since the cell is too large for the Helmholtz condition. Finally, the fast coils are separated 70 mm with a diameter of 60 mm. Each coil has an inductance of less than 5 μH . This enables us to generate a magnetic with a slew rate larger than 500 G/ms. In other words, we can change the magnetic field with several μs when working around the Feshbach resonance. As shown in Table. [3.2](#), by injecting 1 A,

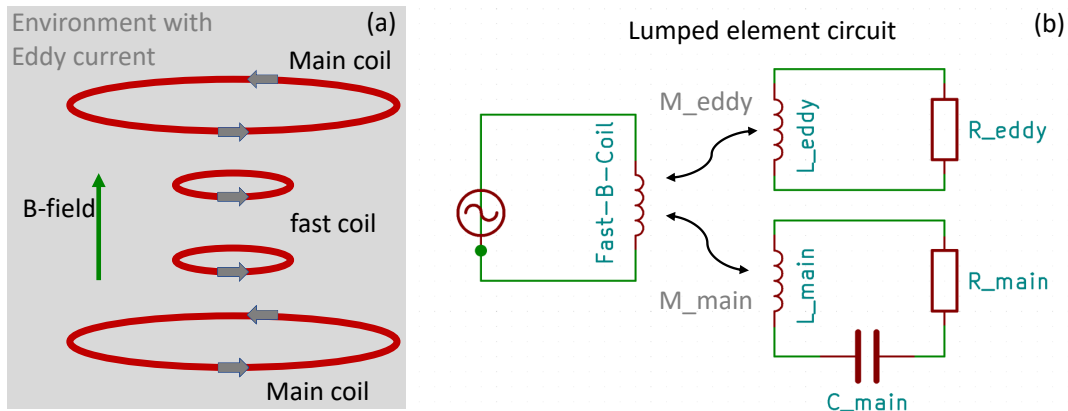


Figure 3.17: (a) set-up with main coil for generating hundred-Gauss level magnetic field and fast coil can change magnetic field in μs time scale. There is also the coupling between these coils and environment, such as metal optical board around the coil or cables for connecting antennas. (b) Lump circuit for simulating the system with two coils and the environment.

we can get 0.67 G (set in Helmholtz type). Our current controller can bear a surge current of less than 10 A as we use two TIP31. So, finally, we can get a maximum magnetic field of 6.7 G which is definitely enough as a fast trim in daily experiments.

	Main coil	Fast coil
Coil sepa. to atom (mm)	25 – 85	35
Coil radius (mm)	52 – 90	30
Coil inductance	$\sim 3 \text{ mH}$	$\sim 5 \mu\text{H}$
Magnetic field per A	$\sim 8.2 \text{ G}$	$\sim 0.67 \text{ G}$
Ramp speed	$\sim 0.6 \text{ G/ms}$	$> 500 \text{ G/ms}$
Number of turns	70	6

Table 3.2: Parameter table of main coil and fast coil

As explained in [Cumby, 2012], we need to consider the coupling of the fast coil, the main coil and the environment. Since, these coupling will cause oscillation and jiggle when quenching the current in the fast coil. As modeled by the lump elements, as shown in Fig. 3.17. The Fast coil are simulated as a inductance driven by a current source. fast coil has mutual inductance with main coil and the environment. The main

coil is viewed a RLC circuit and the environment only as a RL circuit. With this lump circuit simulation, we can qualitatively figure out however these three things coupled to each other. However, more detailed parameter can only be achieved by measure the response of the system. By adding a quenching signal, we can get the response of the whole system. Then, we can do feed-forward to compensate the overshooting or jiggles since the speed of fast coil is about 1000 times faster than the Main coil and the environment.

There are two reasons for us to do the dynamic compensations, first is the coupling of the fast coil and main coil, and the environment will cause a jigger when we quench the current of the fast coil. To avoid this jigger, we feed-forward set the current to compensate for this overshooting. The second is for the droplet experiment: because the magnetic field generated by the main Feshbach coil has a gradient, when we do ToF, the magnetic field at atom position changes with time. So, to keep the magnetic field on atoms unchanged with ToF, we need this dynamic compensation. For the first case, the compensation needs very fast, so we use the fast coil. For the second one, it is a relatively slow-changing process. So we only use the shim coil to do the compensation.

3.5 Other Technical Issues

3.5.1 Magnetic field gradient compensation

As mentioned before, we use a pair of Feshbach coils to generate a large bias magnetic field to control the Feshbach resonance. However, the imperfection of the coil, such as asymmetry of coils and imperfection of distance between up-down Helmholtz coils, renders a gradient and curvature of the magnetic field. This effect can be easily detected by the free-falling of atoms in the high magnetic field. If one finds that the atom's acceleration deviates from gravity acceleration, there must be a gradient.

Another evidence is the MW (RF) spectroscopy for an elongated sample that could detect the horizontal gradient. When we free-falling Rb or Na under a high magnetic field, if the acceleration becomes different from gravity, we can use it as an indicator of magnetic field gradient.

Before talking about cancelling this gradient, we first measure it. The method is simple, following the MW transition calibration method, we apply the MW pulse coupling the $|1, -1\rangle$ and $|2, 0\rangle$ state. To get the spatial distribution of the magnetic field, we first let the atom free-fall, then apply the MW pulse at different ToF. Even though the gradient affects the atom's position by adding an extra acceleration, considering the small effect related to gravity, this can be neglected. Not only exists the gradient but also the the curvature of the magnetic field because the spatial changing B-field is definitely more than linear. By a simple quadratic curve fitting, we get the curvature of about 2.47×10^3 G/cm² and an average gradient of about xx G/cm. One thing that needs to be noticed here is that we measured only the magnetic field gradient in the vertical direction, which is our main contribution. As we can see in the horizontal direction, the acceleration is even much lower than that in the vertical direction, which infer that this gradient should come mainly from the wrong distance of the Helmholtz coil.

It is hard to totally compensate the curvature because it will need to entirely recover the Helmholtz condition, which requires a much larger magnetic field to be added to the existing system. So, to solve the problem we meet, we degenerate to compensate the average gradient to zero inside the interesting ToF we care. So, we can add another magnetic gradient in the vertical direction and adjust its current to find the best compensation point. We use one of the up-down shim coil (e.g. up coil) as a preliminary test. As shown in Fig. 3.18, we can generate an inverse direction gradient opposite to the main coil.

We change the current of the shim coil and test the acceleration of the atom to

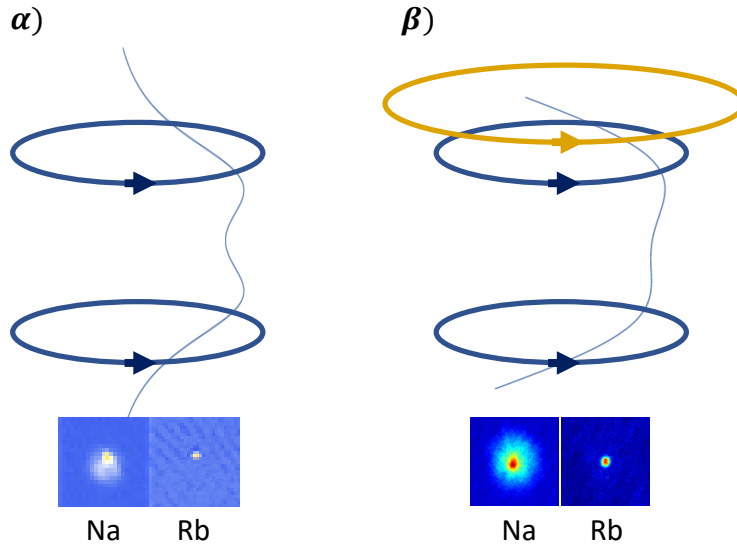


Figure 3.18: $\alpha)$ B-field curvature and gradient affects free falling of atoms. $\beta)$ Using only UP shim coil to compensate gradient.

find the compensation point. As the dipole moment of Na and Rb is quite different, we can also find the intersect point of them, which represents zero average gradient compensation point, as shown in Fig. 3.19. Finally, we tune the shim coil to the current at the intersection. We measure the magnetic field with the MW spectroscopy method and compare the result with the previous non-compensation one, as shown in Fig. 3.20. It is evident that the mean gradient is reduced significantly; however, the curvature is still there. The compensated gradient on average (we take the 10 ms ToF as an average position) are about 0.11 G/cm, which should be enough to observe BEC mixture free-falling.

3.5.2 Microwave full-wave loop antenna

As described in SubSec. 3.2.2, the internal states of atoms can be controlled by the electromagnetic wave. Typically, to drive transition between two different hyperfine states, we need to use micro-wave(MW), which has a wavelength of about 0.3 m to 3

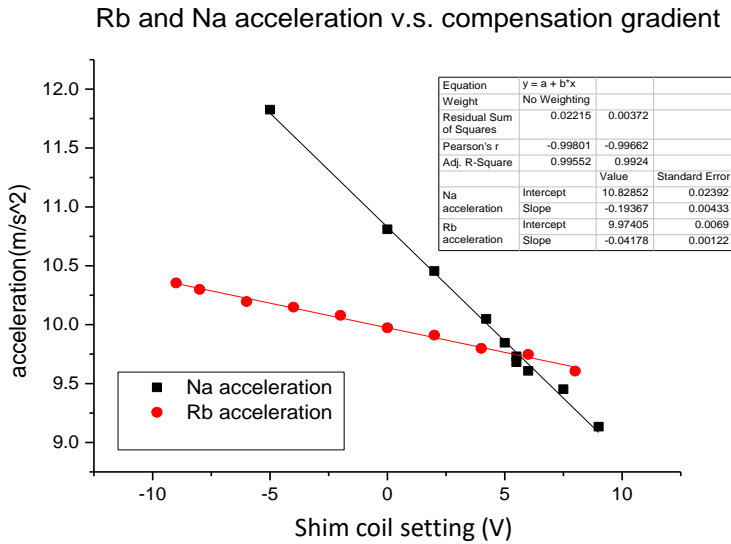


Figure 3.19: By searching the cross point of Na and Rb sharing the same acceleration, we find the compensation point.

m, i.e. 300MHz to 300 GHz for frequency in the vacuum. The hyperfine splittings for Na and Rb atoms are 1.7 GHz and 6.8 GHz at zero magnetic fields. When the magnetic field increasing to 350 G (since we typically use the 347 G Feshbach resonance to control the inter-species interaction), the splitting between $|F = 1, m_F = 1\rangle$ and $|F = 2, m_F = 2\rangle$ states are 2.6 GHz and 7.5 GHz for Na and Rb separately. Thus, we need an antenna that can work well at this frequency. Here, “work well” commonly has two meanings: First, the antenna’s standing wave ratio (SWR) is approaching 1, which means it can transmit most power to coil instead of reflecting it back to the power amplifier. Secondly, we need the atom to feel the largest amplitude of E-field because the transitions between different F-state is mainly connected by electron dipole, i.e. an electrical dipole transition. (here, need more carefully check) So, the antenna’s position, including its distance to the atom and its direction angle, is critical to maximizing the utility of the antenna. We can define the efficiency for the above two processes as μ_{trans} and μ_{anta} , and the total efficiency is just their multiplication.

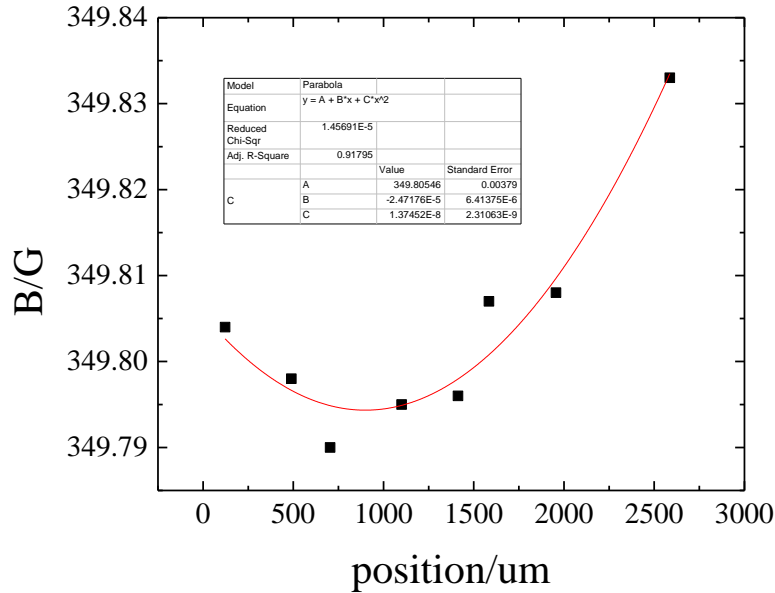


Figure 3.20: Shows the magnetic field spatial distribution at vertical direction after compensation. It still remains gradient and curvature, however much smaller than the one before compensation. We fit it with a quadratic function to get the local gradient and curvature for compensation later.

A commercial antenna is typically designed to work well in the far-field region. The radiation power declines inversely proportional to the distance. Thus, to increase the power on the atom, we put the antenna to the atom as close as possible. However, this renders the radiation on the atom turns to be near-field instead of far-field. As depicted in Fig. 3.21, the electric and magnetic field line of a dipole antenna is plotted as blue and red separately. At a considerable distance of the antenna, the electric field line is almost perpendicular to the \hat{r} direction. However, when getting closed, it shows more portions to the $\hat{\theta}$ direction. This tells us that the near-field electromagnetic field of the antenna behaves quite different from its far-field one. Both electric and magnetic field lines are perpendicular to the Poynting vector in the far-field region, which shows its radiation properties. However, the near-field cannot be treated as radiation; instead, we typically treat it as a “quasi-stati” field. A

quasi-static field means the distribution of EM field is the same as it in electrostatics, except an oscillation in magnitude with $e^{i\omega t}$. In engineering, these study is essential to wireless-charging, proximity sensors and so on.

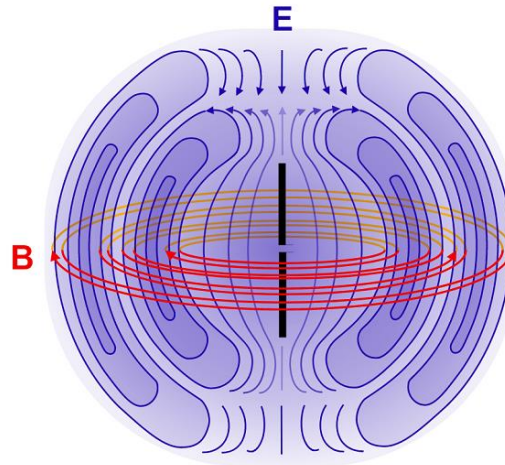


Figure 3.21: Electromagnetic field of a dipole antenna (image from [EverythingRF Website](#)). The near-field and far-field distribution are quite different as described in text.

Previously, we used a horn antenna for Rb MW transition at 6.8GHz. The distance between horn and atom is about 10-15 cm. The problem to put the antenna closer to the atom is its colossal size which could block the optical path, and its metallic body could disturb the strong magnetic field of a large Feshbach coil, causing a gradient on the atom. So the nearest position we can put is about 10 cm away from the atom, and the Rabi frequency of Rb $|1, 1\rangle$ to $|2, 2\rangle$ transition at 350 G (7.5 GHz) is less than 1 kHz with a 40 W power amplifier. The correspondents $\pi/2$ pulse duration is about $250 \mu s$ which is too long for most of our experiments, such as high magnetic field image or too weak for dissociating the FR molecule. Thus, we need to upgrade it to enhance the Rabi frequency.

So, a naive solution is to put the antenna as close to the cell as possible and try to shrink its size smaller and thinner. Therefore, the loop antenna will be a proper choice.

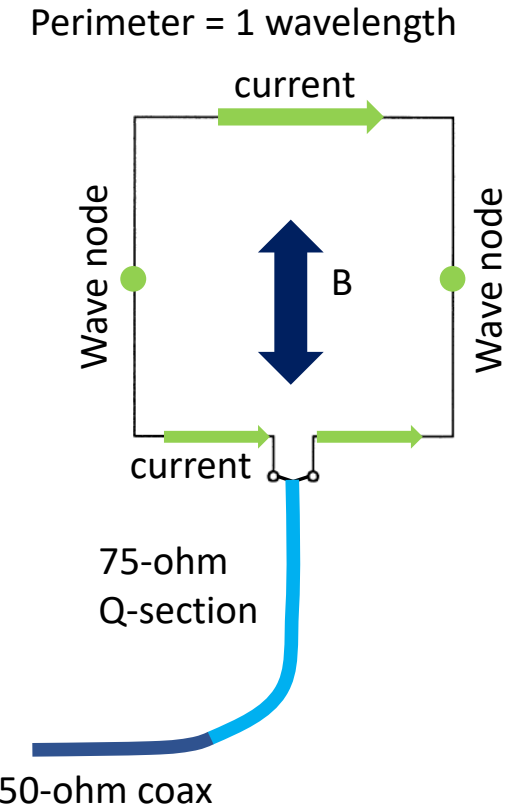


Figure 3.22: Full loop antenna and Q-section for impedance matching. The parameter of the loop is set to be one wavelength of the emitting MW. The 75-ohm Q-section is for impedance matching.

A loop antenna is just a simple loop connected to the signal generator. However, for our case with frequencies at 2.6 GHz and 7.5 GHz, The wavelength is around several cm to tens of cm. This is comparable to our coil size, which could introduce a severe problem with impedance matching. A standard solution is making the perimeter of the loop antenna just a full wavelength, which is called the full-wave loop antenna as shown in Fig. 3.22. When the scale of the antenna is closed to wavelength, the distribution of radiation becomes quite different to those small-loop antennas. This can be explained by a simplified picture, as shown in Fig. 3.22. At the joint place, and directly opposite current changes with the largest amplitude, and there placed

two nodes at the quarter wavelength place to the joint. However, the current almost has the same phase on the whole coil for a small loop antenna. Therefore, they have different radiation patterns.

According to the near-field quasi-static EM field theory, the maximum radiation appears at $\lambda/4$ away from the coil plane. Furthermore, the power at the centre of the coil is zero, which is different from the case of a small-loop coil. For our case with $f = 2.6\text{GHz}$, the wavelength is about 12 cm. So, we place the coil 3 cm away from the atom to achieve the largest power. For the 7.5 GHz case for Rb MW in a high magnetic field, we set the perimeter of the loop to 4 cm. However, we cannot put the coil 1 cm away from the atom due to the distance limitation. Finally, by making the trade-off between the optical paths and MW power, we set the tiny coil at the side of the cell with a 45-degree angle and distance to atom about 3 cm.

After preparing the coil, we set up the standard MW power amplifier circuit for it. Before the amplifier, we add a switch controlled by a TTL signal, and the signal generator is an SG-386. The critical point to increase the efficiency from power amplifier to the coil, i.e. η_{trans} , we need carefully consider the impedance matching from the transmission wire to the loop coil. As shown in Fig. 3.23, we demonstrate several full-wave loop antennas with different shapes. They have different impedance; the ideal one is rectangular with an aspect ratio of 1:2, with 50 Ohm impedance. However, for our case with a round shape, we have the coil with 133 Ohm. Our transmission line and power amplifier are all 50 Ohm, so we need to match impedance. We use a balloon, i.e. a 75 Ohm transition line, to enhance the transmission rate. As shown in Fig. 3.22, the signal can be reflected at the boundary of two lines with different impedance. Boundaries of 50-to-75 and 75-to-133 offer two reflection waves. If we choose a proper length of the 75 Ohm line, we can cancel the reflection thanks to their superposition.

Even though we know how long the q-section line should be, we still need to do

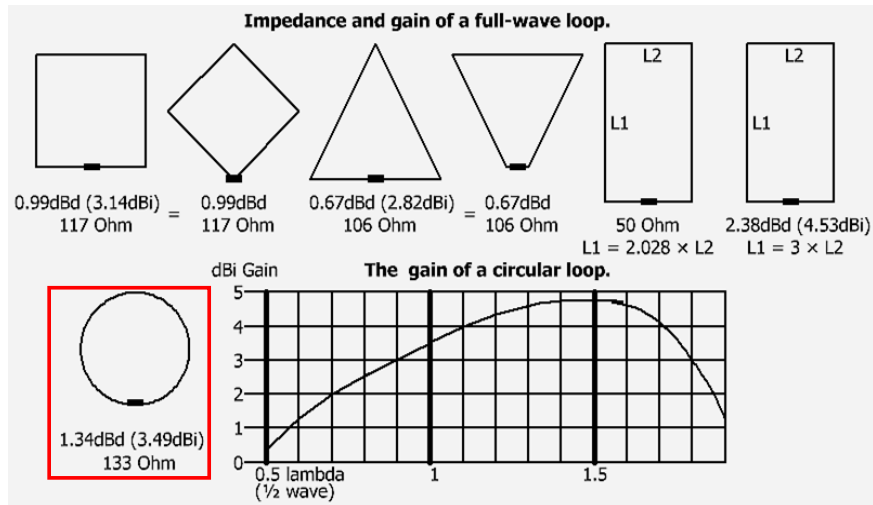


Figure 3.23: (image from [pa0fri.home](#)) Impedance of full-wave loop antenna with different shapes. In our experiment, we use the round-shape to matching the optical path of MOT beam. In experiment in LH24C, the 1:2 rectangular is better since there is no need to do the impedance matching.

the offline test for its performance because the length of several cm is too short to allow uncertainties from the imperfection of the coil's shape and impedance. These incomplete can cause the phase of reflection wave shifting and decline the effect of impedance matching. Therefore, we build a series of coils with different lengths of its q-section and measure its return loss rate by a directional coupler. As shown in Fig. 3.24, we send the signal into the output port of a coupler, and the reflecting wave from the antenna (connecting on the input port of the coupler) will be coupled a small portion into the coupled port and detected by an analyser spectrum. By calculating the reflecting power and injection power, we plot the return loss rate as a function of the length of the q-section line in Fig. 3.25. We find the period does coincident with the half of wavelength. There is a shift that could be attributed to the imperfection of the q-section line. By fitting with a sine function, we extract the period, shift and so on. Finally, We can now build the coil with the lowest return loss for covering our usage frequency.

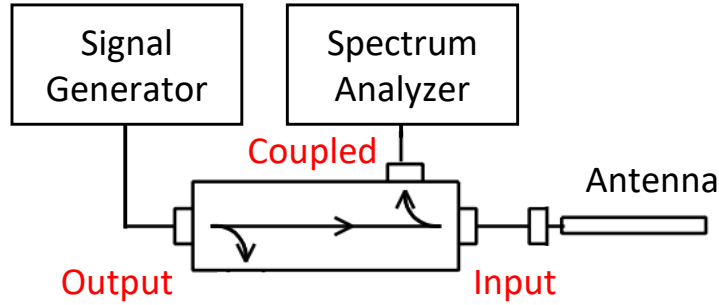


Figure 3.24: Test the return loss of the antenna by a directional coupler. Noticed that the input signal is sent from the Output port of the coupler.

Finally, we put the coil onto the atom cell. First, we test the transmission rate of the coil online to make sure the impedance matching works well since the offline test with an environment open; however; however, the online environment is full of different metals around the coil, which could change the boundary condition and shift the impedance of the coil. So, we use the same method to test the transmission rate of the coil, as shown in Figure. The bandwidth is about xxx MHz. Then, we test the Atomic Rabi frequency to measure the final performance of the coil. We apply the MW pulse for Na at 350 G and get the Rabi frequency at different freq or detuning?. As shown in Figure, we test the saturation power and get a Rabi maximum of about 100kHz(check the number). This could allow us to make a pi pulse within 10 us which is enough for most cases such as optical pumping in the high field and MW spectroscopy.

After confirming that the 2.6 GHz coil does work, we built the 7.5 GHz coil, which could also increase the Rabi freq for Rb at high field. This one is similar to the Na coil with a parameter of 4 cm, which is relatively too small even to put it onto the science cell because it will block some part of the MOT beam. So, we choose to sacrifice power by arranging the coil on one edge of the cell, which increases the distance

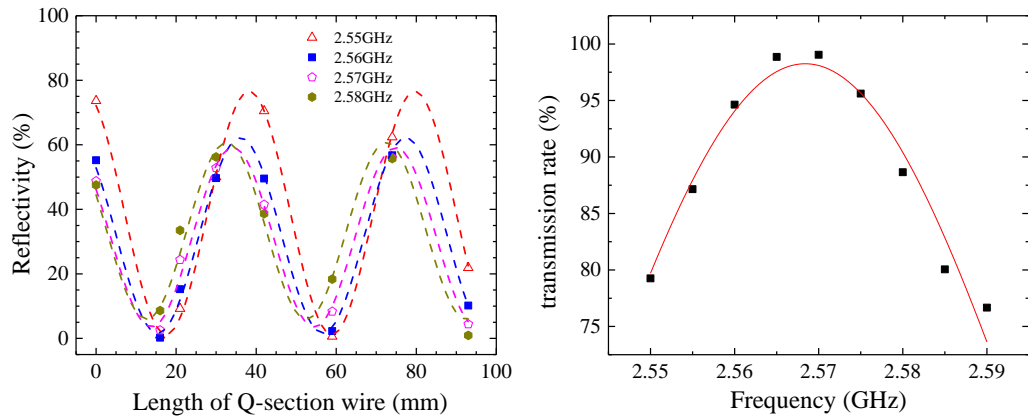


Figure 3.25: Test the return loss the full-wave loop antenna by changing the length of the Q-section line. Right side shows the band width test which provides a bandwidth of 67 MHz.

between the coil and atoms to about 3 cm. The best working distance for the 7.5 GHz coil is $\lambda/4$, i.e. 1 cm, so for 3 cm distance, we get a power of about 1/3 compared to the maximum one. In order to pump atoms to the target state within tens μs , the required Rabi frequency needs about 10 kHz. Our online test shows a Rabi frequency of 10 kHz, allowing a 50π -pulse for fast removing Rb atom from Feshbach molecules. Thanks to this new antenna, we can remove the horn antenna since the coil still works for 6.8 GHz with a transition rate of about 10%, even its impedance matching point is 7.5 GHz. For typical MW evaporation, very little power is enough. Finally, removing the horn antenna leaves us much more space for future building optics layout.

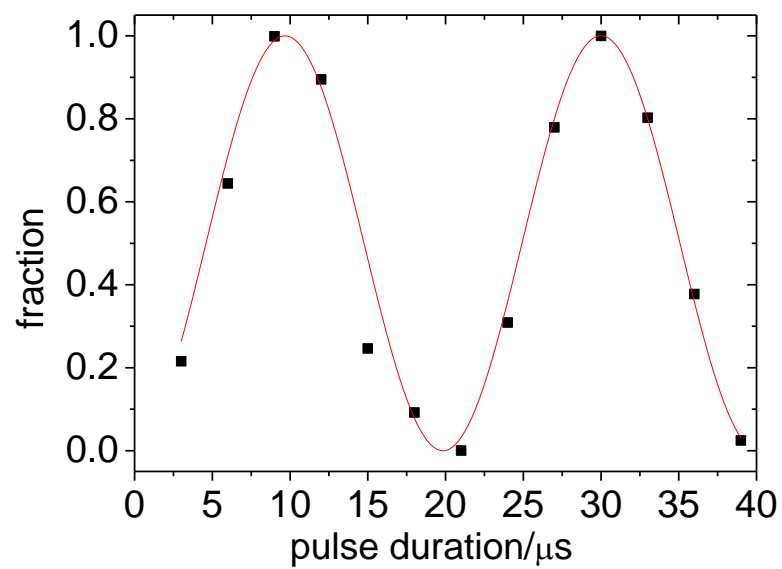


Figure 3.26: Test Rabi oscillation of Na $|1, 1\rangle$ to $|2, 2\rangle$ under 350 Gauss magnetic field. We can achieve a Rabi frequency of 50 kHz, which enable us pump atom to the target cycling transition within 10 μ s.

Chapter 4

Precision characterisation of a Feshbach Resonance

In physical science a first essential step in the direction of learning any subject is to find principles of numerical reckoning and methods for practicably measuring some quality connected with it. [Thomson, 2011]

— William Thomson, 1st Baron Kelvin
Electrical Units of Measurement (1883)

4.1 Overview

This chapter presents our precision calibration of a Na-Rb Feshbach resonance at 347.64 G. The purpose of inserting this chapter before discussing the droplet experiment is to require a precision map of the scattering length (actually not only Na-Rb but also Na-Na and Rb-Rb) as a function of the magnetic field. This narrative order is convenient for discussing the droplet experiment; however, the research in chronological order is tortuous as described in Sec. 6.2. I learned my lesson that one should not trust any unverified data. Previous measurements of Feshbach resonance(FR) pa-

rameters of Na and Rb, by three-body-loss (3B-loss) spectrum or associating method, both encountered intrinsic systematic errors, such as thermal averaging or shifting [Bartenstein et al., 2005; Zürn et al., 2013]. Due to the high sensitivity of the droplet phase diagram, we need the scattering length map as accurate as possible. So, we implemented the dissociation method to refine the results of FR parameters at 347.64 G resonance. In the rest of this section, we will introduce what Feshbach resonance (FR) is, discuss the previous measurement results, and finally offer the arrangement of this chapter.

Feshbach resonance as a powerful toolbox plays its essential role in cold atom experiments. With this nob, we can tune the interaction between atoms by applying an external field. Thus, it is used to explore the few-body (or many-body) physics and form molecules that open a new field in ultracold physics. Feshbach resonance requires two channels to couple to each other. One is the open channel (or entrance channel), with which collision can produce atoms, i.e. the energy of the collision pair is larger than the asymptotic energy of the channel. Another is the closed channel which offers bound states with the set energy instead of scattering state[Chin et al., 2010]. When the energy of one bound state in the closed channel approaching the open channel threshold (typically set to be 0), the resonance happens. Near the resonance B_0 , the two-body scattering length is approximate as

$$a(B) = a_{\text{bg}} \left(1 + \frac{\Delta}{B - B_0} \right), \quad (4.1)$$

where a_{bg} is the slowly varying background scattering length, and Δ is the resonance width. By simply scanning the magnetic field, the scattering length a and thus the effective two-body contact interaction can be changed from repulsive (for $a > 0$) to attractive (for $a < 0$). The capability of manipulating the interaction strengths has been playing a vital role in the study of exotic physics such as the con-

trolled collapse [Donley et al., 2001] or soliton formation in Bose-Einstein condensates (BEC) [Khaykovich et al., 2002; Strecker et al., 2002], the BEC-BCS crossover in quantum-degenerate Fermi gases [Regal et al., 2004; Zwierlein et al., 2004; Bartenstein et al., 2004; Bourdel et al., 2004], and more recently the formation of dilute quantum droplets [Petrov, 2015; Ferrier-Barbut et al., 2016a; Cabrera et al., 2018]. In addition, FRs are used to associate atomic pairs and form weakly bound Feshbach molecules (FMs) [Köhler et al., 2006]. Combined with a subsequent two-photon Raman process, this has led to the creation of long-sought ultracold ground-state molecules [Ni et al., 2008; Takekoshi et al., 2014; Molony et al., 2014; Park et al., 2015; Guo et al., 2016; Voges et al., 2020].

The typical way of tuning the scattering length by an FR in the cold atom experiment is to control the magnetic field. When the magnetic field is tuned to the vicinity of the resonance, we have a large scattering length, thus can increase the two-body collision rate. This method enables us to enhance the three-body loss rate [Wang et al., 2013], and by scanning the magnetic field, we can obtain a loss dip (as shown in Fig. 4.1). This phenomenon can be used to characterize an FR directly at first glance. By a simple Gaussian fitting to extract the peak, we obtain the resonance position. The problem of calibrating an FR by this method mainly comes from the existence of lots of Efimov states near the resonance. These three-body bound states render a severe three-body loss and then broaden or shift the measurement of resonance position [Chin et al., 2010]. Later in 2015, [Wang et al., 2015a] used the association method to calibrate the 347 G and 478 G Na-Rb FR again. However, the asymmetric associating spectrum still reveals the thermal broadening and shifting, leading to inaccuracy measurement of FR parameters [Bartenstein et al., 2005; Zürn et al., 2013].

Thus, in this Chapter, we use the most accurate method, i.e. the dissociating method, to calibrate the FR of Na and Rb at 347.64 G. To obtain an accurate map of scattering length, we need the knowledge of the molecular bound state. Recalling

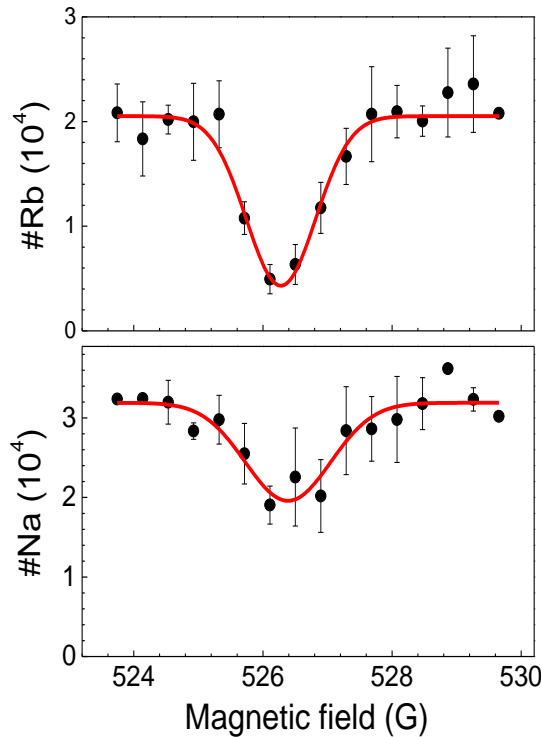


Figure 4.1: shows the loss spectrum of one Feshbach resonance of $\text{Na}|F = 1, m_F = 0\rangle$ and $\text{Rb}|F = 1, m_F = 0\rangle$.

the discussion in chap. 2, when we talk about quantum scattering, we typically use a pseudopotential to substitute the real complex interaction potential. However, we have to go back to the complicated real potential to obtain its scattering properties before having the scattering length. Then, an accurate map of the molecule potential is essential. Historically, people use the hot molecule to get the spectrum and then inversely deduct the potential curve []. However, this spectrum is typical only for deeply bound molecule states, which contains little information about the weakly bound states and thus the Feshbach resonances. However, our experiments need the scattering length near a Feshbach resonance, related to shallow bound states near or approaching zero when the external magnetic field is tuned across specific values. Thus, similar to the associating method, our goal is clear that we need a method to

obtain these bound states energy accurately. However, to avoid the systematic error in the associating method (as shown in Fig. 4.2), we first form a pure molecule sample and then dissociate. Thinking in the coordinate of one molecule, one would find that this dissociation process can avoid thermal effects and thus improve the measurement accuracy. After obtaining the information of bound states, we can fit them by the coupled-channel calculation to get the Na-Rb potential. Finally, we achieve the accurate scattering length map as a function of the magnetic field.

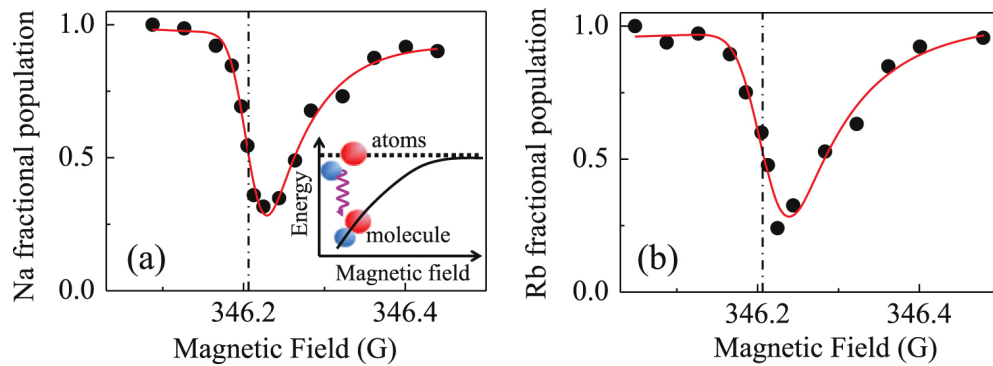


Figure 4.2: Image from [Wang et al., 2015a]. (a) and (b) shows the Na and Rb residue signal when doing the associating of Feshbach molecules. The dash-dot line shows the association limit, which corresponding to the zero-energy of the bound state. For a magnetic field less than the threshold, there are still association signals indicating the thermal effect. These thermal shifting and broadening smoothen the kink at the associating limit.

The rest of this chapter is arranged as follows: Sec. 4.2 describes the method of dissociation measurement of FR molecule binding energy. Then, we apply the coupled-channel (c.c.) calculation fitting the data to obtain an accurate molecule potential curve. Finally, we achieve an accurate scattering length map. In Sec. 4.3, we present ten more Feshbach resonance loss spectrums with different spin configurations of Na and Rb. They are compared to a c.c. calculation. We measured most elastic resonances and some of the inelastic, which process imaginary part of scattering length. This information can be used as a map for further exploration of a variety

of Bose mixtures. Moreover, in the second part of Sec. 4.3 we demonstrate c.c. calculations for Rb-Rb and Na-Na both in $|F = 1, m_F = 1\rangle$ states. We find that the Na intraspecies interaction shows a very smooth variation from $54.5 a_0$ (at 0 Gauss) to $64 a_0$ (at around 900 G). This renders our estimation of Na-Na intraspecies scattering length shift about 10% in the droplet paper [Guo et al., 2021a], from $54.45 a_0$ to $60.05 a_0$.

4.2 Na-Rb Feshbach resonance at 347.64 G

This section¹ reports new measurements of binding energies for the state that causes the FR near 347.64 G. To reach the highest accuracy, we implement the dissociation method [Bartenstein et al., 2005; Zürn et al., 2013; Chin and Julienne, 2005; Chapurin et al., 2019] to measure the binding energies. We achieve magnetic field stability at the mG level. The data are used to refine the interaction potentials for the $X^1\Sigma^+$ and $a^3\Sigma^+$ electronic states by fitting to coupled-channel bound-state calculations. We then use coupled-channel scattering calculations to obtain a highly accurate mapping $a(B)$ for the FR near 347.64 G. This has become a cornerstone for our recent experiment on the heteronuclear Na-Rb quantum droplet[Guo et al., 2021a].

By applying a radio-frequency pulse to drive a bound-free transition [Bartenstein et al., 2005; Zürn et al., 2013; Chapurin et al., 2019]. The binding energy is obtained by subtracting the free-free transition energy from the bound-free transition energy. In the current work, as shown schematically in Fig. 4.3(a), the FM lies very close in energy to the free atom pair. In this case, the dissociation can be driven by magnetic field modulation spectroscopy [Claussen et al., 2003; Thompson et al., 2005]. As illustrated in Fig. 4.3(b), this is implemented by adding a small-amplitude oscillation to the magnetic field after the magnetoassociation. The oscillating magnetic field can be ex-

¹Announcement: most materials in this section is from our paper [Guo et al., 2021b], which could lead to resemblance.

pressed as $B + A \times \sin(2\pi ft)$, with B the final magnetic field that determines E_b , and $A \ll B_0 - B$. B_0 is the resonance magnetic field and f is the modulation amplitude and frequency. Dissociation starts to occur when f matches E_b/h . For $f > E_b/h$, the excess energy is converted to kinetic energy of the free atoms as $E_k = hf - E_b$. Due to the variation of the bound-free Franck-Condon factor with E_k [Chin and Julienne, 2005], the dissociation spectrum is typically asymmetric and broad with respect to f .

In the rest part of this section, we first detailedly describe experimental measurement. Then, after obtaining the binding energies, we demonstrate the coupled-channel modelling for fitting. Finally, we compare the new calibrated parameters of Feshbach resonance at 347.64 G to the previous measurements.

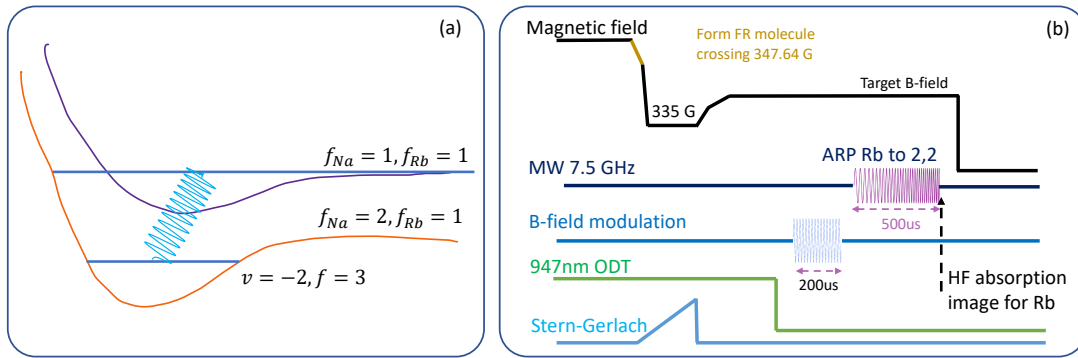


Figure 4.3: Measuring the binding energy of a Feshbach molecule with magnetic field modulation spectroscopy. (a) The binding energy of the FM is E_b . An oscillating magnetic field can drive a bound-free transition. (b) The FMs are first created by ramping the magnetic field across B_0 . After the magnetic field is stabilized to its final value, a small-amplitude sinusoidal oscillation at frequency f near E_b/h is added to dissociate the FMs and measure the binding energy. See the text for a more detailed description of the magnetic field ramping procedure.

4.2.1 Measurement of the Na-Rb Feshbach molecule binding energy

Our experiment starts from an optically trapped ultracold mixture of ^{23}Na and ^{87}Rb atoms, both in their lowest hyperfine state $|F = 1, m_F = 1\rangle$ [Wang et al., 2013, 2015a; Jia et al., 2020]. Magnetoassociation starts from an initial magnetic field of 350 G, just above the FR at $B_0 = 347.64$ G. The magnetic field is ramped down across the resonance to form FMs, and then to 335.6 G. At this field, the FMs have a nearly zero magnetic dipole moment; this allows us to remove the residual atoms with a short and strong magnetic field gradient without losing molecules. Afterwards, the magnetic field is ramped up to a range of target values below B_0 for further experiments. Following this procedure, we can routinely obtain a pure sample of $^{23}\text{Na}-^{87}\text{Rb}$ FMs with a typical temperature of 300 nK and a trap lifetime of more than 30 ms. This short lifetime is due to near-resonance photon scattering by the 947 nm optical trap light [Guo et al., 2017; Jia et al., 2020], which is provided by a home-built diode laser system. In another experiment on $^{23}\text{Na}-^{87}\text{Rb}$, in which a single-frequency 1064 nm laser is used as the optical trap light, FM lifetimes greater than 100 ms have been observed [Wang et al., 2019; Guo et al., 2021a]. Nevertheless, the current lifetime is more than enough for the present work, as we need only 10 ms for magnetic field stabilization and less than 1 ms for dissociation.

To obtain a high-quality dissociation spectrum, we need a pure molecule sample. If there remain atoms inside the molecule sample, though very few, because the dissociated atoms are few, it is hard to distinguish the dissociated one from the residue one. On the other hand, this part of the atom could be associated to molecules which makes the spectrum hard to subtract information. To remove residue atoms from molecules, we need to identify them by different properties, such as magnetic dipole, mass, transition frequency. To blast atoms away, we need to obtain the acceleration of atoms as large as possible and keep the molecule unaffected. The typical

methods can be magnetic gradient, species-dependent optical dipole force (tune-in, tune-out trap) and resonance light for atoms. In our experiment, we originally apply the magnetic gradient at 335 G, where FMs possess zero magnetic dipoles. This method typically requires 1-2 ms to separate atoms all away from molecules, which is slow. The main limitation is the slew rate of coil current due to large coil inductance. So, later we change the method: we first transfer atoms to $|F = 2, m_F = 2\rangle$ state by light or by MW, then use the image cycling transition to remove the atom. With the newly upgraded full-wave loop antenna, we can achieve a high Rabi frequency for Na and Rb, both up to 50 kHz. Then, a ten us pulse could transfer all atoms to the cycling transition ground state $|F = 2, m_F = 2\rangle$. Then, the probe light with several saturation-intensity can blast all atoms away within less than 10 μs . More details can be found in Chap. 3.

The magnetic field modulation is generated by a single loop coil driven by a low-frequency high power radio frequency amplifier. The single loop coil is placed just above the vacuum cell and coaxially with the Feshbach coils so that a modulation depth of several mG can be added to the large magnetic field. The coil has a limited modulation bandwidth of about 2 MHz. The optical trap was turned off 50 μs before applying the magnetic field modulation pulse to avoid the AC-Stark shift from the trapping light. This also reduces possible systematic errors induced by mean-field shifts of both the FMs and the free atoms as the density of FMs is lowered down. The magnetic field modulation pulse duration is chosen empirically so that the fraction of dissociation is no more than 70%. This is a compromise for detection signal-to-noise ratio and the requirement for using the Fermi Golden rule to fit the dissociation lineshape, which is only strictly followed for weak coupling.

The dissociation signal is detected by absorption imaging of the fragmented ^{87}Rb atoms. Fig. 4.4(a) shows several examples of dissociation spectrum versus the modulation frequency f for FMs from 347.371(5) G to 345.713(5) G. Here the magnetic field

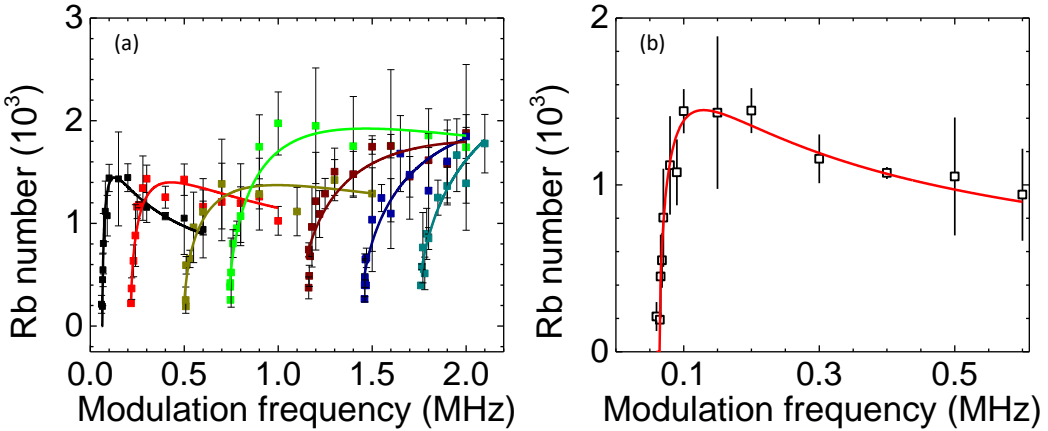


Figure 4.4: Feshbach molecule dissociation spectrum at magnetic field of (a) 347.371 G, and (b) 346.000 G. The red solid curves are fitted to Eq. 4.2 to extract the FM binding energies. Because of the limited modulation bandwidth of the single-loop coil, only part of the spectrum is accessible in (b).

is measured with radio frequency spectroscopy of the Rb atoms. Threshold behaviors are clearly visible in all dissociation spectra. Fig. 4.4(b) shows the enlargement of 347.371 G dissociation spectrum in (a). There is no dissociation observed for f below 60 kHz. Since the dissociation process involves no moment transfer, the dissociation threshold is an accurate measurement of the binding energy E_b of the FM. Above this threshold, the profile of the spectrum is determined by the overlap between the wave functions of the bound and free states. As the excessive energy $hf - E_b$ will be converted into the relative motion of the two atoms, the wave function of the free atoms and thus the bound-free transition rate changes with f . Following [Mohapatra and Braaten, 2015], the lineshape of magnetic field modulation spectroscopy can be represented as

$$N_{Rb}(f) \propto \frac{\sqrt{hf - E_b}}{hf}. \quad (4.2)$$

From this lineshape, a dissociation maximum should be observed at $f = 2E_b/h$, afterwards, the signal will decay with a long tail following $1/\sqrt{f}$. The spectrum

in Fig. 4.4(b) follows this lineshape well. For the spectrum with $E_b > 1$ MHz in Fig. 4.4(a), the maximum is not reached due to the limited modulation bandwidth.

To determine the dissociation threshold, we fit each spectrum with Eq. 4.2. For partial dissociation spectra like Fig. 4.4(b), we have verified with simulated data that E_b can still be determined with uncertainties less than 5 kHz. The variation of E_b with magnetic field, over a range from 0.061 MHz to 1.739 MHz, is plotted in Fig. 4.5 as black open circles. The error bar for each E_b is smaller than the symbol size. The uncertainty in the measured magnetic field is ± 3 mG.

Figure 4.2 shows E_b for FMs that were obtained in 2015 with the association method [Wang et al., 2015a] near the resonances at 347.64 G. In that work [Wang et al., 2015a], the binding energy was fitted using the square-well model [Lange et al., 2009] with a fixed background scattering length $a_{bg} = 66.77a_0$. This value of a_{bg} was obtained from the coupled-channel modelling of the several Feshbach resonances observed with atom-loss spectroscopy in 2013 [Wang et al., 2013]. However, the square-well model requires a_{bg} much larger than the interaction range, which is set by the mean scattering length of the van der Waals potential [Gribakin and Flambaum, 1993]; this is $\bar{a} = 55.2 a_0$ for $^{23}\text{Na}^{87}\text{Rb}$. This condition is not satisfied for the Feshbach resonances considered here. It is also well known that resonance positions measured by atom-loss spectroscopy are not accurate enough due to the complicated dynamics of three-body recombination. These issues all contribute to the inaccuracy of the Feshbach resonance parameters determined previously [Wang et al., 2015a]. In the following, we solve these issues with a new coupled-channel modelling of the binding energies of the FMs.

4.2.2 Coupled-channel modeling and FR parameters

After obtaining the Feshbach molecule's binding energy, we measure out how the highest shallow bound state energy varies with the magnetic field. This very shallow

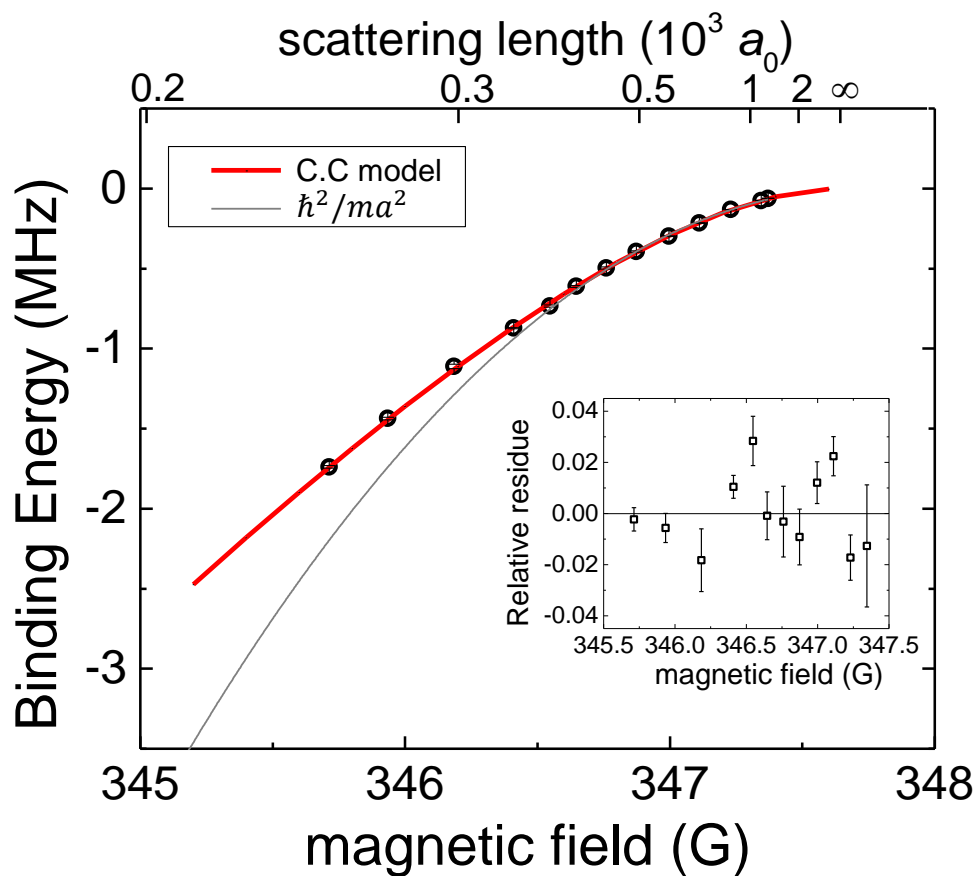


Figure 4.5: Binding energy of $^{23}\text{Na}^{87}\text{Rb}$ Feshbach molecules created via the FR near 347.64 G in the entrance channel $\text{Na}|1, 1\rangle + \text{Rb}|1, 1\rangle$. The black open circles are the data points measured with the dissociation method. The error bars are smaller than the symbol size. The solid red curve is from the coupled-channel (c.c.) fitting, while the thin black curve is from the universal model. Inset shows the relative residue between the experiment data and the c.c. fitting.

bound state is affected mainly by the shortest part and the long-range part (C_6, C_8, C_{10}) of the molecular potential curve. So, by the above measurement, we can calibrate the potential more precisely, especially at short and long-range since a typical molecular potential is achieved by the Fourier-transform molecular spectroscopy [Pashov et al., 2005], which mainly use the information for the deep binding bound state, i.e. middle range potential. We can achieve a more accurate molecular potential for Na and Rb by combining the spectroscopy data for mid-range and the measurement of shallow bound state for short and long-range.

Coupled-channel calculations rely on expanding the total wavefunction for a pair of interacting atoms in a basis set that represents the electron and nuclear spins and the relative rotation of the atoms (the partial wave L). Substituting this expansion into the total Schrödinger equation produces a set of coupled differential equations that can be solved to obtain either bound-state or scattering properties. The Hamiltonian for the interacting pair is

$$\hat{H} = \frac{\hbar^2}{2\mu} \left[-\frac{1}{R} \frac{d^2}{dR^2} R + \frac{\hat{L}^2}{R^2} \right] + \hat{H}_A + \hat{H}_B + \hat{V}(R), \quad (4.3)$$

where R is the internuclear distance, μ is the reduced mass, and \hbar is the reduced Planck constant. \hat{L} is the two-atom rotational angular momentum operator. The single-atom Hamiltonians \hat{H}_i contain the hyperfine couplings and the Zeeman interaction with the magnetic field. The interaction operator $\hat{V}(R)$ contains the two isotropic Born-Oppenheimer potentials, for the $X^1\Sigma_g^+$ singlet and $a^3\Sigma_u^+$ triplet states, and anisotropic spin-dependent couplings which arise from dipole-dipole and second-order spin-orbit coupling. In the present work, scattering calculations are carried out using the MOLSCAT package [Hutson and Le Sueur, 2019; Hutson and Le Sueur, 2020] and bound-state calculations use the related packages BOUND and FIELD [Hutson and Le Sueur, 2020]. The scattering wavefunction is expanded in a fully uncoupled

basis set that contains all allowed spin and rotational functions, limited by $L_{\max} = 2$. The numerical methods are similar to those used in Ref. [Berninger et al., 2013], so will not be described in detail here.

The interaction potential used here is based on the potential curves for the $X^1\Sigma^+$ and $a^3\Sigma^+$ states of NaRb, originally obtained by fitting to Fourier transform (FT) molecular spectroscopy [Pashov et al., 2005] and later refined by Feshbach spectroscopy with ultracold atoms [Wang et al., 2013]. The potential curve for each electronic state, with spin $S = 0$ (singlet) or 1 (triplet), has three parts: (1) a high-order power-series in the well region, which is the part best determined by FT spectroscopy; (2) a long-range extrapolation, outside internuclear distance $R_{\text{LR},S}$, which uses theoretical dispersion coefficients and a simple exchange term; (3) a short-range extrapolation, inside $R_{\text{SR},S}$, which uses a simple repulsion of the form $A_S + B_S/R_S^N$. $R_{\text{SR},S}$ is usually chosen as a distance just outside the inner turning point of the potential at zero energy. For particular values of $R_{\text{SR},S}$ and N_S , A_S and B_S are usually determined so that the short-range extrapolation has the same value and derivative at $R_{\text{SR},S}$ as the mid-range power-series potential².

Our goal is to adjust the interaction potential to fit the measured FM binding energies, while retaining as much as possible its ability to reproduce the FT spectra. We therefore keep the two power series that represent the singlet and triplet potential wells fixed at the fitted values of Ref. [Wang et al., 2013]. We also retain the long-range extrapolation in its original form, with the dispersion coefficients unchanged. We vary only the parameters $R_{\text{SR},S}$ and N_S that define the short-range extrapolations. For the triplet potential, $R_{\text{SR},1}$ is held at its original value from Ref. [Wang et al., 2013], and N_1 is varied; this provides sufficient flexibility to adjust the singlet scattering length and reproduce resonance positions and binding energies. For the singlet potential, however, the original value of $R_{\text{SR},0}$ is so close to the turning point that varying N_0

²This constraint was applied in the present work, but for the potential of Ref. [Wang et al., 2013] there are derivative discontinuities at $R_{\text{SR},S}$.

does not allow enough change in the potential to reproduce the experimental data. In this case N_0 is held at its original value from Ref. [Wang et al., 2013], and $R_{\text{SR},0}$ is varied.

Here attaches the new potential parameters for Na and Rb $X^1\Sigma_g^+$ singlet and a $^3\Sigma_u^+$ triplet states.

```
Analytic potential energy curve for the NaRb a3Sigma+ state
(for definition of parameters see C. Samuelis et al. PRA 63, 012710
(2000))
-----
Potential is given with respect to the dissociation limit which is
set to 0!

For R <= 4.65 A

U(R)=A+B/R^alpha

A -232.9656123524      cm-1
B 10710621685.47        cm-1 A^alpha
alpha      11.492

For 4.65 < R < 11.30 A

U(R)=Sum_i[a_i*((R-R_m)/(R+b*R_m))^i]

b      -0.4700
R_m    5.60071538 A
a_0   -203.35070852 cm-1
a_1   0.122517410860683240E+01 cm-1
a_2   0.968561681714175506E+03 cm-1
a_3   -0.167358901820848331E+03 cm-1
a_4   -0.115108986132623340E+04 cm-1
a_5   0.538103153477437104E+03 cm-1
a_6   0.576427139041465671E+04 cm-1
a_7   -0.137759208524156093E+05 cm-1
a_8   -0.484354206699185452E+05 cm-1
a_9   0.876873287464803143E+05 cm-1
a_10  0.242372373596938676E+06 cm-1
a_11  -0.283727768851481727E+06 cm-1
a_12  -0.762367745318190078E+06 cm-1
a_13  0.433100100910781766E+06 cm-1
a_14  0.150133971696866141E+07 cm-1
a_15  -0.489081569236799405E+05 cm-1
a_16  -0.164041059210233274E+07 cm-1
a_17  -0.680259713656829204E+06 cm-1
a_18  0.665168317123337765E+06 cm-1
```

```

a_19  0.606016435356653412E+06 cm-1
a_20  0.137434664322447614E+06 cm-1

For R>=11.30 Å

U(R)=-C_6\R^6-C_8\R^8-C_10\R^10+A_ex*R^gamma*exp(-beta*R)

C_6      0.129463596372576691E+08 cm-1 Å^6
C_8      0.358980000000000000E+09 cm-1 Å^8
C_10     0.130601455102733498E+11 cm-1 Å^10
A_ex    0.31859846D+05 cm-1 Å^(-gamma)
gamma   5.00810
beta    2.20850 Å^-1

-----
Analytic potential energy curve for the NaRb X1Sigma+ state
(for definition of parameters see C. Samuelis et al. PRA 63, 012710
(2000))
-----
Potential is given with respect to the dissociation limit which is
set to 0!

For R <= 2.7256 Å

U(R)=A+B/R^alpha

A          -8490.090071421      cm-1
B          450828.6299011      cm-1 Å^alpha
alpha     4.06143861049682720

For 2.7256 < R < 11.30 Å

U(R)=Sum_i [a_i*((R-R_m)/(R+b*R_m))^i]

b      -0.2100
R_m    3.64340736 Å
a_0   -5030.50869783 cm-1
a_1   -0.662030723944292271E-01 cm-1
a_2   0.253807725995464061E+05 cm-1
a_3   0.929104757521979809E+04 cm-1
a_4   -0.211814748606123285E+05 cm-1
a_5   -0.284181834656136671E+05 cm-1
a_6   0.210407753693068798E+04 cm-1
a_7   -0.851968733976350748E+06 cm-1
a_8   -0.123216494098773529E+07 cm-1
a_9   0.383640579108661637E+08 cm-1
a_10  0.109125343263982777E+08 cm-1
a_11  -0.109331126199059677E+10 cm-1
a_12  0.540863749615297675E+09 cm-1

```

```

a_13  0.203930014933835602E+11 cm-1
a_14  -0.222458146577416687E+11 cm-1
a_15  -0.258727375257563232E+12 cm-1
a_16  0.419458345047378906E+12 cm-1
a_17  0.226157469213112939E+13 cm-1
a_18  -0.493156268638760059E+13 cm-1
a_19  -0.133732693094783848E+14 cm-1
a_20  0.391427433409150078E+14 cm-1
a_21  0.491914424477468672E+14 cm-1
a_22  -0.214673998282790187E+15 cm-1
a_23  -0.736821254504513125E+14 cm-1
a_24  0.806693583557253000E+15 cm-1
a_25  -0.249784752437157937E+15 cm-1
a_26  -0.198517974510287375E+16 cm-1
a_27  0.172480088271182725E+16 cm-1
a_28  0.281094984850021900E+16 cm-1
a_29  -0.441448085841028300E+16 cm-1
a_30  -0.122221795646213325E+16 cm-1
a_31  0.552071157529799900E+16 cm-1
a_32  -0.210051881065563800E+16 cm-1
a_33  -0.244906408631624500E+16 cm-1
a_34  0.238499017935224850E+16 cm-1
a_35  -0.611040299017092875E+15 cm-1

For R>=11.30 Å

U(R)=-C_6\R^6-C_8\R^8-C_10\R^10-A_ex*R^gamma*exp(-beta*R)

C_6    0.129463596372576691E+08 cm-1 Å^6
C_8    0.358980000000000000E+09 cm-1 Å^8
C_10   0.130601455102733498E+11 cm-1 Å^10
A_ex   0.31859846E+05 cm-1 Å^(-gamma)
gamma  5.00810
beta   2.20850 Å^-1

```

The shape of the curve of E_b as a function of B is quite insensitive to variations in the singlet and triplet scattering lengths, represented by $R_{SR,0}$ and N_1 . It is therefore sufficient to fit to one binding energy from each FR. For the resonance near 347.64 G, we choose the point with $E_b/h = 0.611(6)$ MHz at 346.646(5) G, while for the resonance near 478.7 G, we choose the point with $E_b/h = 0.400$ MHz at 478.052(10) G. The parameters $R_{SR,0}$ and N_1 are then adjusted so that these binding energies are reproduced essentially exactly. The resulting values are $R_{SR,0} = 2.7256 \text{ Å}$ and $N_1 = 11.492$. The singlet and triplet scattering lengths calculated from the fitted potentials

are $a_s = 106.474a_0$ and $a_t = 68.864a_0$, respectively. These are $0.27a_0$ smaller and $0.24a_0$ larger than the values of Ref. [Wang et al., 2013], indicating that the triplet potential needs to be slightly more repulsive than the original at short range, while the singlet potential needs to be slightly less repulsive.

We use the fitted potentials to calculate the s -wave scattering length $a(B)$. We find that each resonance is well represented by Eq. 4.1. The parameters B_0 , Δ and a_{bg} are obtained as described by Frye and Hutson [Frye and Hutson, 2017], and are given in Table 4.1. In Fig. 4.5, the binding energies calculated from the universal model $E_b = \hbar^2/2\mu a(B)^2$ using the new $a(B)$ is also shown. Compared with the coupled channel results (red solid curve), this reproduces the data only for $E_b < 0.6$ MHz.

Table 4.1: Parameters of the two low-field s -wave Feshbach resonances for the entrance channel $\text{Na}|1, 1\rangle + \text{Rb}|1, 1\rangle$.

B_0 (G)	Δ (G)	a_{bg} (a_0)	reference
347.648	4.255	76.33	this work
347.64	5.20	66.77	[Wang et al., 2015a]
347.75	4.89	66.77	[Wang et al., 2013]
478.714	3.491	71.55	this work
478.83	4.81	66.77	[Wang et al., 2015a]
478.79	3.80	66.77	[Wang et al., 2013]

In the present fit, the resonance near 347.64 G has shifted by about 0.08 G compared to Ref. [Wang et al., 2013]. The resonance near 487.7 G has shifted by more than 0.1 G. These shifts produce substantial changes in the calculated scattering lengths. Moreover, in Ref. [Wang et al., 2013], the calculated scattering length was fitted using the formula

$$a(B) = a_{\text{bg}} \left[1 + \frac{\Delta_0}{B - B_0} + \frac{\Delta_1}{B - B_1} + \dots \right], \quad (4.4)$$

with a single B -independent background scattering length a_{bg} for all resonances. This formula breaks down when the background scattering length varies significantly between resonances. In the present work, Eq. 4.1 is found to be a good local repre-

sentation for each resonance, but significantly different values of a_{bg} are needed for the resonances at 347.64 G and 487.7 G. Such behavior can arise from many sources, including the changing spin character of atomic states with magnetic field and the presence of additional resonances not included in the summation of Eq. 4.4. As shown in Fig. 4.6, for the resonance near 347.64 G, the scattering lengths calculated with the new potential differ by about $20a_0$ from those of Ref. [Wang et al., 2015a] in the region from 349.8 G to 350.0 G that is important for studies of Na-Rb quantum droplets. This change is significant and largely explains the discrepancies initially observed between experiment and theory in Ref. [Guo et al., 2021a].

All the coupled-channel calculations use a basis set that includes functions for partial waves $L = 0$ and $L = 2$, with the effective dipolar coupling function of Ref. [Wang et al., 2013] unchanged. Omitting the $L = 2$ basis functions causes shifts that are on the same level as the experimental uncertainties: the calculated resonance positions and binding-energy curves shift down by between 3 and 4 mG. It is possible to include additional partial waves, but we expect the shifts to be very small. In contrast to Ref. [Wang et al., 2013], we do not include any variation of the atomic hyperfine coupling with internuclear distance.

4.3 Na-Rb, Na-Na and Rb-Rb scattering length summary

Besides the Feshbach resonance at 347.64 G, different combinations of the spin state of Na and Rb possess plenty of FRs. Ref. [Wang et al., 2013] investigated the entrance channels $|m_F = 1\rangle + |m_F = 1\rangle$ and $|m_F = -1\rangle + |m_F = -1\rangle$ and in total observed three *s*-wave and two *p*-wave FRs. In addition, ten more *s*-wave FRs were predicted for collisions between pairs of atoms in different $F = 1$ hyperfine Zeeman states. In this section, we report the experimental observation of several of these FRs below 1000 G in 5 hyperfine Zeeman combinations. We believe these FRs will find impor-

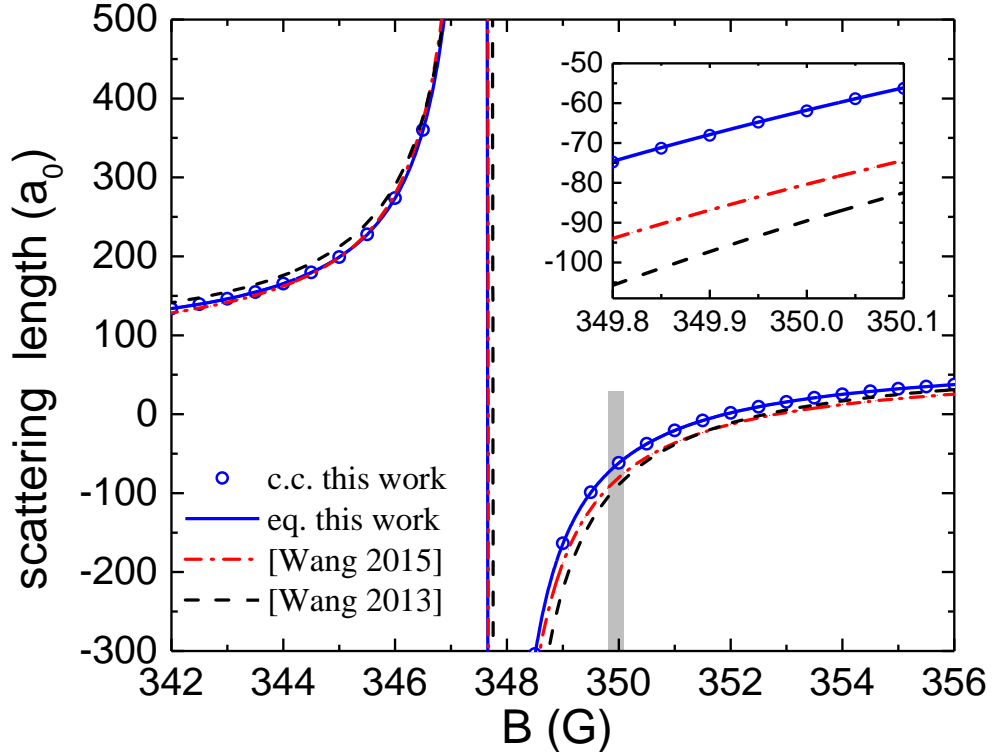


Figure 4.6: Comparison of the mapping between magnetic field and scattering length with Feshbach resonance parameters obtained in this work, using coupled-channel results directly (blue open circles) and fitted to Eq. 4.1 (blue solid curve) and , and in Ref. [Wang et al., 2015a] (red dash-dotted curve) and Ref. [Wang et al., 2013] (black dashed curve), both using Eq. 4.4. The region of interest for the droplet experiment [Guo et al., 2021a], marked with a vertical gray bar, is enlarged in the inset.

tant applications in the future, for example, in the investigation of BEC mixtures and quantum droplets with more than two components [Ma et al., 2021].

With the powerful tool, MOLSCAT [Hutson and Le Sueur, 2019; Hutson and Le Sueur, 2020], we can get more precise maps of scattering length and magnetic field. Since even the background scattering length varies when the external field changes, the value of the scattering length, especially for a finite (not low) field, should be treated with more care. Here we find that the Na-Na 1,1 state have a smoothly varying background scattering length from low field to around 900 G (near the FR). Its value starts from $54.45 \text{ } a_0$ to about $64 \text{ } a_0$. For our droplet experiment, under about 350 G magnetic field, the Na-Na scattering length is $60.05 \text{ } a_0$ which is larger about 10% than at low field.

4.3.1 Na-Rb scattering length for different spin combination

For simplicity, we will denote the collision channel of a pair of $^{23}\text{Na}+^{87}\text{Rb}$ atoms by $|m_F^{\text{Na}}\rangle + |m_F^{\text{Rb}}\rangle$. In ref. [Wang et al., 2013], both the $|1\rangle + |1\rangle$ and the $|-1\rangle + |-1\rangle$ channels were investigated and in total 3 *s*-wave and 2 *p*-wave FRs were observed. As shown in Fig. 4.7, we detect more FRs in different combinations. The experiment for this section starts from optically trapped thermal mixtures of Na and Rb both in the $|-1\rangle + |-1\rangle$ channel. The number of atoms for both species are typically around 10^5 and the sample temperatures are about $1 \mu\text{K}$. The atoms are then transferred to selected hyperfine Zeeman levels with radio frequency (rf) rapid adiabatic passages. For each species, the $|-1\rangle \rightarrow |0\rangle$ and the $|0\rangle \rightarrow |1\rangle$ Zeeman splittings are very similar. In addition, these splittings in different species are also very similar to each other. To avoid cascade transitions and to realize species-selective state control, the state transfers are performed at 100 G where the transitions are all different by more than 500 kHz. With this method, we are able to prepare the Na-Rb mixture in all the 9 possible m_F combinations of their $F = 1$ states. Then, we ramp the magnetic field to

different values and hold the samples for 50 ms before releasing the atoms from the optical trap and measuring the remained numbers of atoms. Interspecies FRs manifest as losses of atoms in both ^{23}Na and ^{87}Rb atoms as a result of enhanced interspecies three-body recombination rates. As presented in Fig. 4.7, guided by the predictions in [Wang et al., 2013], we observe 10 FRs in 6 hyperfine Zeeman combinations.

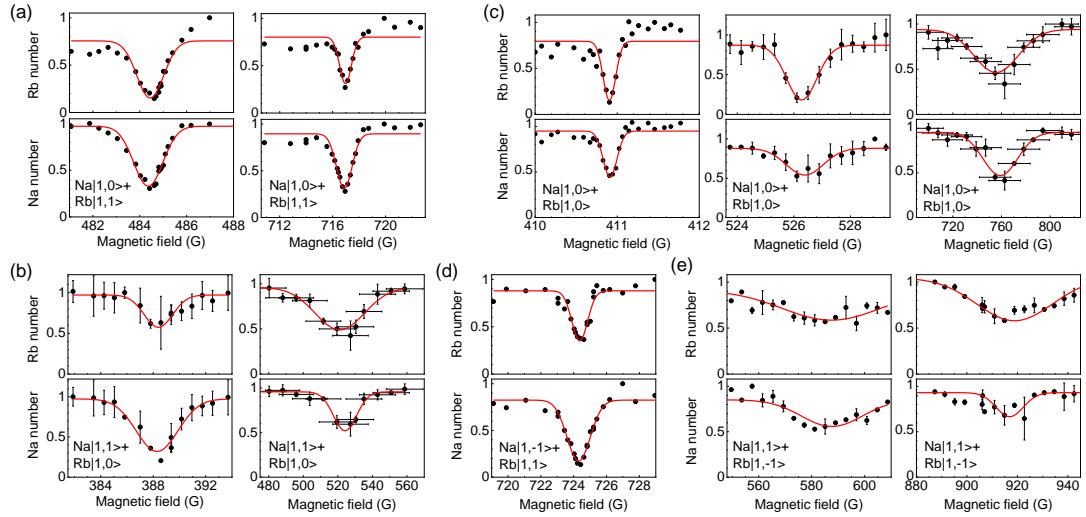


Figure 4.7: Feshbach resonances in ^{23}Na - ^{87}Rb , observed by losses for atoms in the $F = 1$ hyperfine states. (a) and (b) are for the two channels in the $M_F = 1$ manifold; (c), (d) and (e) are for the three channels in the $M_F = 0$ manifold. The typical holding time at each magnetic field is 50 ms. The solid curves are from Gaussian fitting to determine the lineshape center. Error bars for the atom numbers represent one standard deviation. The large error bars for the magnetic field for the several broad loss spectra are due to less precise magnetic field control in these cases (see text).

We have carried out coupled-channel calculations of resonance parameters for both elastic and decayed resonances, using the interaction potentials obtained in Sec. 4.2.2. The results are included in Table 4.2. For elastic resonances, the resonance positions for the lowest threshold of each M_F is first located with the FIELD program [Hutson and Le Sueur, 2020]. The FRs are then characterized using the MOLSCAT program [Hutson and Le Sueur, 2019; Hutson and Le Sueur, 2020] following the elastic procedure of Ref. [Frye and Hutson, 2017], which converges on the

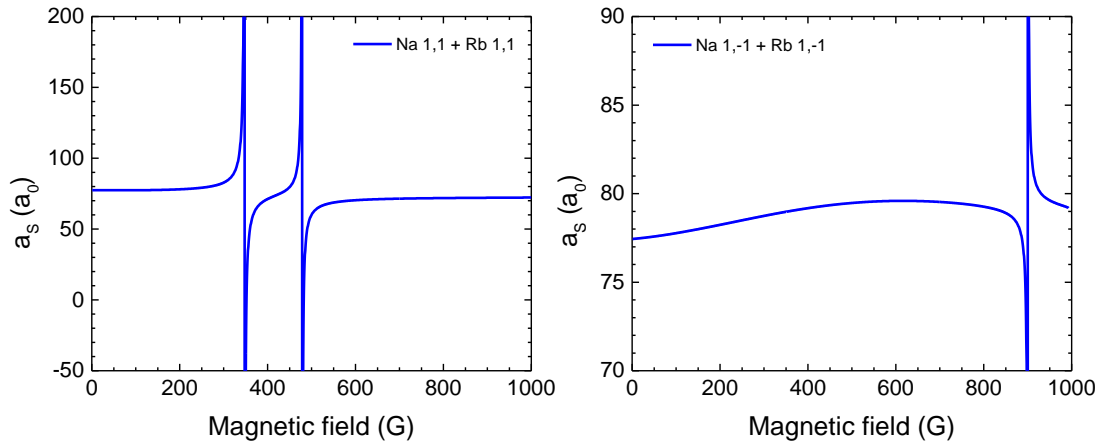


Figure 4.8: Both $\text{Na}|1\rangle+\text{Rb}|1\rangle$ and $\text{Na}|-1\rangle+\text{Rb}|-1\rangle$ are elastic channels. Here we only plot the real part of the scattering length since there is no imaginary part. Two resonances show in $\text{Na}|1\rangle+\text{Rb}|1\rangle$ channel and one in $\text{Na}|-1\rangle+\text{Rb}|-1\rangle$ channel. A smooth variation of the scattering length is obvious in $\text{Na}|-1\rangle+\text{Rb}|-1\rangle$ channel.

resonance position B_0^{cc} , the elastic resonance width Δ , and the background scattering length a_{bg} . Here a_{bg} is a local background scattering length that is different for each resonances. In the current calculation, we have not included the spin-spin interaction, so that both the quantum number L of the partial wave and its projection M_L are conserved in the calculation. Since $M_{\text{tot}} = m_F^{\text{Na}} + m_F^{\text{Rb}} + M_L$ is conserved, only closed channels with $M_F = m_F^{\text{Na}} + m_F^{\text{Rb}}$ the same as the colliding atoms can cause FRs.

As shown in Table 4.2 and in Fig. 4.8, $\text{Na}|1\rangle+\text{Rb}|1\rangle$ $\text{Na}|-1\rangle+\text{Rb}|-1\rangle$ are two channels with all resonances elastic, which means there is no possible for the scattering to other channels. These resonances are a pole as shown in the scattering length plot following the $1/(B - B_0)$ variation. If only considering the two-body collision, one would not have the loss peak as shown in Fig. 4.1 or Fig. 4.7, because increasing the scattering length only means increasing the elastic collision rate. So, the loss peaks in those measurements are the result of the three-body loss.

When an inelastic channel is present, the states at the threshold are quasi-bound,

Table 4.2: Comparison of experimental resonance positions B_0^{exp} with theoretical parameters for interspecies FRs below 1000 G in ^{23}Na - ^{87}Rb , for the nine $F = 1$ entrance channels. L indicates the partial wave of the entrance channel. B_0^{exp} is the mean of the centers of the loss spectra for ^{23}Na and ^{87}Rb in Fig. 4.7, determined by Gaussian fitting. Error bars represent one standard deviation. The theoretical values are from coupled-channel calculations using the singlet and triplet potential-energy curves described in Sec. 4.2.2 with the latest potential parameters. B_0^{cc} , Δ , and a_{bg} are the theoretical position, elastic width, and background scattering length, respectively. The last column “inel.” indicates whether the FR is subject to inelastic losses from spin exchange. For decayed FRs with inelastic losses, the resonant scattering length a_{res} and the inelastic width Γ_{inel} are also listed.

Entrance channel	L	B_0^{exp} (G)	B_0^{cc} (G)	Δ (G)	$a_{\text{bg}}(a_0)$	$a_{\text{res}}(a_0)$	Γ_{inel} (G)	inel.?
$\text{Na} 1, 1\rangle + \text{Rb} 1, 1\rangle$	0	347.61(2)	347.645	4.258	76.328			N
	0	478.82(3)	478.712	3.495	71.548			N
$\text{Na} 1, 1\rangle + \text{Rb} 1, 0\rangle$	0	388.5(2)	388.577	5.684	78.441	6548.8	-0.13617	Y
	0	522(10)	524.286	1.010	74.332	12.906	-11.634	Y
$\text{Na} 1, 0\rangle + \text{Rb} 1, 1\rangle$	0	-	358.078	<0.001	80.108			N
	0	484.45(5)	484.569	4.476	77.258			N
	0	-	570.441	<0.001	73.784			N
	0	716.97(6)	717.166	5.593	72.998			N
$\text{Na} 1, 1\rangle + \text{Rb} 1, -1\rangle$	0	587(3)	580.686	0.241	82.389 - 0.0072 <i>i</i>	2.3917 + 0.87566 <i>i</i>	-16.596	Y
	0	920(1)	913.431	0.091	81.139 + 0.0352 <i>i</i>	0.47768 + 0.12885 <i>i</i>	-30.861	Y
$\text{Na} 1, 0\rangle + \text{Rb} 1, 0\rangle$	0	410.90(1)	409.810	0.176	82.328			N
	0	526.29(3)	526.548	5.676	78.132	23515	-0.03772	Y
	0	759(13)	768.781	1.638	75.495	19.983	-12.373	Y
$\text{Na} 1, -1\rangle + \text{Rb} 1, 1\rangle$	0	-	419.648	<0.001	80.109	0.25533	-0.34477	Y
	0	-	516.986	0.003	79.401			N
	0	724.38(4)	727.270	4.870	76.444			N
$\text{Na} 1, 0\rangle + \text{Rb} 1, -1\rangle$	0	-	-	-	-			N
$\text{Na} 1, -1\rangle + \text{Rb} 1, 0\rangle$	0	-	609.754	0.416	80.572			N
	0	-	759.441	5.676	78.826			N
$\text{Na} 1, -1\rangle + \text{Rb} 1, -1\rangle$	0	899.8(3)	900.317	-0.315	79.270			N
	1	954.2(3)	954.755					N
	1	954.5(3)	955.024					N

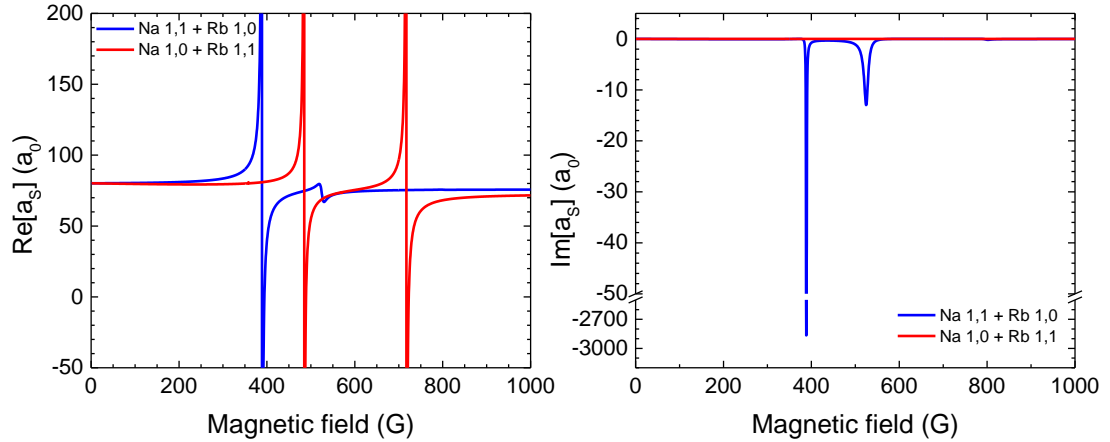


Figure 4.9: Scattering lengths of $M_F = 1$ channels, including $\text{Na}|1\rangle+\text{Rb}|0\rangle$ and $\text{Na}|0\rangle+\text{Rb}|1\rangle$. Left(right) shows the real(imaginary) part of the scattering length. For $\text{Na}|1\rangle+\text{Rb}|0\rangle$ channel there are two inelastic resonance with non-zero imaginary part of scattering length.

so using FIELD is more complicated. Instead, the FRs are located by computing the scattering lengths for magnetic fields up to 1000 G using the MOLSCAT program [Hutson and Le Sueur, 2019; Hutson and Le Sueur, 2020]. Once an FR is located, the resonance parameters are then determined following the regularized scattering length or fully complex procedure of Ref. [Frye and Hutson, 2017]. In this case, the scattering length is complex and shows an oscillation rather than a pole at resonance [Hutson, 2007]. Such a resonance is termed decayed, and the procedure generates the resonant scattering length a_{res} and the inelastic width Γ_{inel} in addition to B_0^{cc} , Δ and a_{bg} .

The calculation reproduces all the observed s -wave resonances. As shown in Table 4.2, the deviations between B_0^{cc} and B_0^{exp} are within 0.5 G for most of the elastic FRs, labelled by “N” in the last column “inel?”. The only exception is the resonance observed at 410.9 G for the entrance channel $|0\rangle+|0\rangle$, for which B_0^{cc} is 1.1 G lower. As shown in Fig. 4.11(b), this channel features a nearby switchover between the relative channel energies near 450 G. The four s -wave resonances for the entrance channels

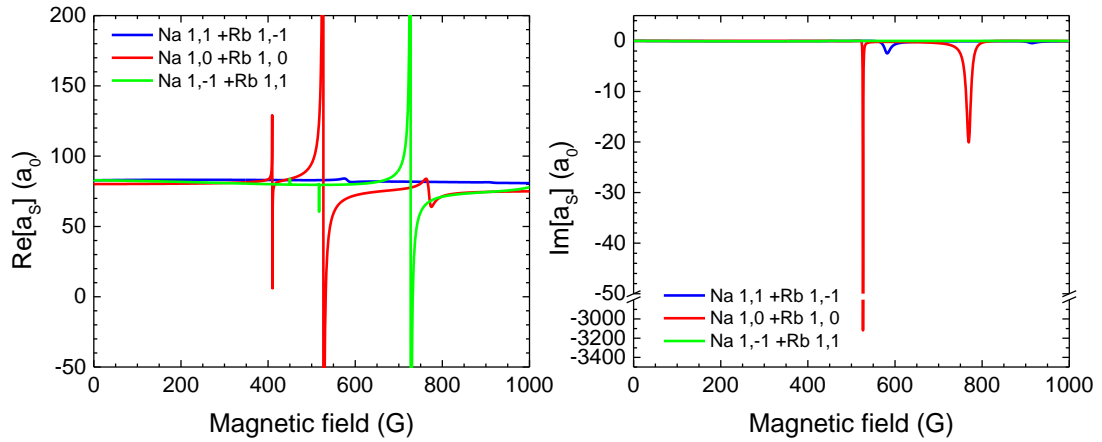


Figure 4.10: Scattering lengths of $M_F = 0$ channels, including $\text{Na}|1\rangle+\text{Rb}|-1\rangle$, $\text{Na}|0\rangle+\text{Rb}|0\rangle$ and $\text{Na}|-1\rangle+\text{Rb}|1\rangle$. Left(right) shows the real(imaginary) part of the scattering length.

$|1\rangle + |1\rangle$ and $|0\rangle + |1\rangle$ all have calculated resonance widths Δ of several Gauss. They should all be useful for investigating Na–Rb mixtures with tunable interactions. These resonances also have rather small calculated effective ranges, on the order of 10s of a_0 ; thus, using the scattering lengths should be sufficient for most applications.

The decayed FRs can have very different characters, depending on a_{res} and/or Γ_{inel} . When a_{res} is large and $\Gamma_{\text{inel}} \ll \Delta$, the resonance *may* be fairly similar to the elastic case and be dominated by three-body loss. However, when a_{res} is small and Γ_{inel} is comparable to or larger than Δ , the loss is more likely to be dominated by two-body loss. This looks to be the case for the resonances at 522 G for $|1\rangle + |0\rangle$, at 759 G for $|0\rangle + |0\rangle$, and the unobserved one at 420 G for $|-1\rangle + |1\rangle$. It is also true for both resonances for $|1\rangle + |-1\rangle$, but for those there is a significant *background* loss characterized by the imaginary part of a_{bg} .

For the decayed resonances with $\Gamma_{\text{inel}} < 1$ at 388 G for $|1\rangle + |0\rangle$ and at 526 G for $|0\rangle + |0\rangle$, the calculated resonance positions B_0^{cc} agree with the measured resonance positions B_0^{exp} very well. However, deviations up to several Gauss are observed for inelastic resonances with large Γ_{inel} . These can be attributed to several factors. For the

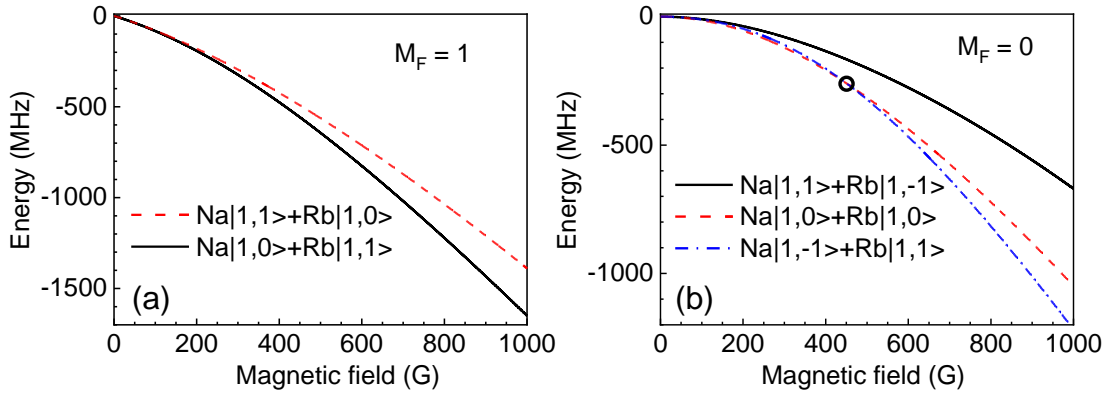


Figure 4.11: (a) Channel energies for the manifold with $M_F = 1$ for magnetic field up to 1000 G. (b) The same for the manifold with $M_F = 0$. The energies of the channels $|0\rangle + |0\rangle$ and $| -1 \rangle + |1\rangle$ cross each other near 450 G, as marked by the black open circle. For each M_F , atom pairs in higher-energy channels can undergo inelastic loss by spin exchange to the lower-energy channels.

two resonances with very broad observed loss spectra at 522 G for $|1\rangle + |0\rangle$ and at 759 G for $|0\rangle + |0\rangle$, the resonance centers have large uncertainties near 10 G. In addition, in presence of the background loss, the two-body loss induced by these resonances has an asymmetric (Fano-like) profile and its measured peak is not at B_0 . Finally, although we have not studied them carefully, some nearby intraspecies FRs in Na or Rb may also affect the measurements of the resonance positions.

Several resonances predicted by the coupled-channel calculation are not observed experimentally. Most of these are very narrow ones with calculated Δ in the mG range. No resonance is found from the calculation for the entrance channel $|0\rangle + | -1 \rangle$. In addition, we have not searched experimentally for FRs in the entrance channel $| -1 \rangle + |0\rangle$ although the calculation indicates that two resonances should exist.

Table 4.2 also lists the several p -wave FRs observed by [Wang et al., 2013] for the entrance channels $|1\rangle + |1\rangle$ and $| -1 \rangle + | -1 \rangle$. As mentioned above, we have not attempted to improve the agreement between the current calculation and the experiment by including the dependence of the atomic hyperfine coupling on R . We note

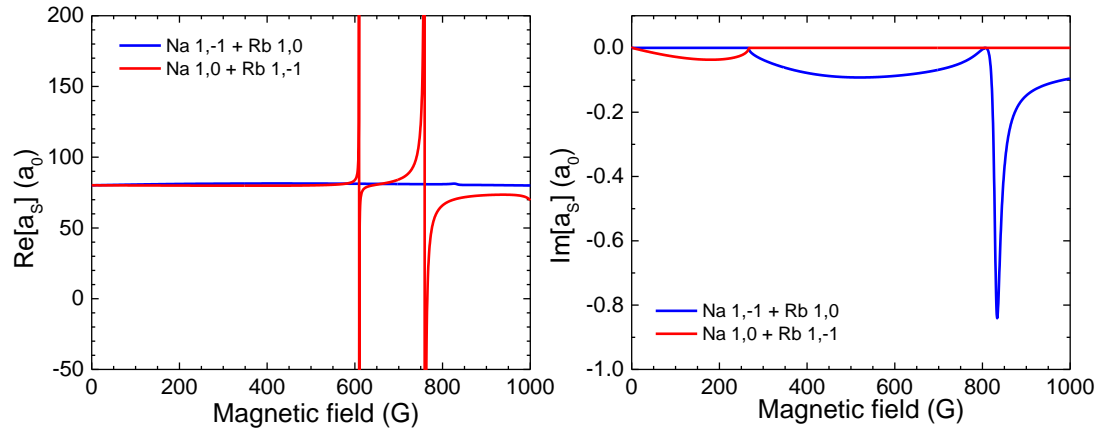


Figure 4.12: Scattering lengths of $M_F = -1$ channels, including $\text{Na}|0\rangle+\text{Rb}|-1\rangle$ and $\text{Na}|-1\rangle+\text{Rb}|0\rangle$. Left(right) shows the real(imaginary) part of the scattering length.

that Ref. [Cui et al., 2018], which presented a compilation of FRs for alkali atoms calculated with multichannel quantum defect theory (MQDT), identified the resonance near 284 G as a “broad” p -wave resonance. It would be possible to perform a full-scale coupled-channel fitting to these resonances. This, however, is not pursued here as it would involve further adjustments to the potential parameters, beyond those used in Ref.[Guo et al., 2021a]. In view of the inaccuracy of the loss spectroscopy compared with the measurements of FM binding energies, we believe such fitting is not currently justified.

4.3.2 Na-Na and Rb-Rb scattering length

Besides interspecies Na-Rb scattering properties, we also study the intraspecies scattering length for Na-Na and Rb-Rb, because the droplet experiment needs all three scattering lengths. Our calculation directly send the potential file from [] to MOLSCAT [] and then use the molscat modular to obtain the scattering length. The Feshbach resonances for Na-Na and Rb-Rb are all far away from 347 G, where we study the droplet []. However, Na-Na scattering length varies with magnetic field very smoothly, even without resonance. As shown in Fig. 4.13, From 0 to around 800 G, we have a scat-

tering length changing from $54.5 \text{ } a_0$ to about $64 \text{ } a_0$. For magnetic field around 350 G, i.e. the field for forming droplet sample, the scattering length for Na-Na is $60.05 \text{ } a_0$. This value is about 10% larger than in a low magnetic field.

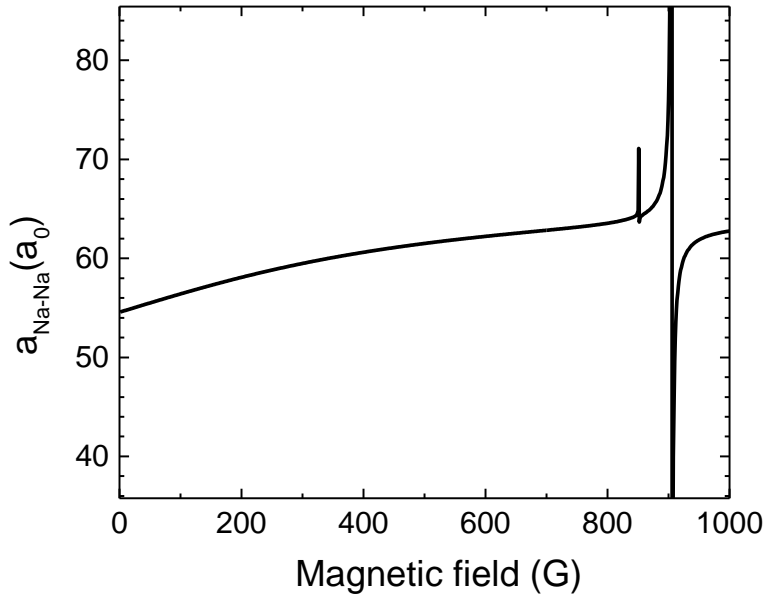


Figure 4.13: $\text{Na}|1,1\rangle + \text{Na}|1,1\rangle$ scattering length as a function of magnetic field. A smooth changing from

Verifying the Na-Na scattering length value is not easy since the smooth-changing background scattering length only has about 10% to 20% variation. Typical methods for measuring s -wave scattering length, such as measurement of elastic collision rate by tracing the thermalization process[] or by measuring the BEC expansion[], are all difficult and need precisely calibration of some other physical parameter (such as atomic number in the second method). These measurements are prone to have an error with 10% to 20%. On the other hand, the coupled-channel calculation is the most precise method and is an ab initio calculation that offers reliable numbers. So, we directly take the calculated one.

End of chapter.

Chapter 5

Quantum droplet of hetero-nuclear Bose mixture

Law of physicists I:
Without experimentalists, theorists tend to drift. [Lee, 1992]

— T.D. Lee
History of the weak interactions (1987)

This chapter discusses the heteronuclear droplets formed by the Bose-Einstein condensate mixture of Na and Rb. We first re-analyze the droplet, however, with a finite volume instead of homogeneous density distribution. This is to compare with experiments since an actual quantum droplet we build in the experiment always has a specific size due to a limited atomic number. We make a rough estimation by analyzing the energy scales of each term. Then, continuing with the analytical solution in Sec. 2.2, we implement the variational calculation. We use a simple Gaussian trial function to help understand how different energy scales compete in the finite-size droplets. Its specific size mainly requires introducing a kinetic energy term (i.e. quantum pressure). In order to better understand the droplet sample, we simulate it with extended Gross–Pitaevskii equation (eGPE). In this part, we give the derivation of the extended GPE especially for the two-species BEC sample near zero MF energy region. We put the code of GPELAB [Antoine and Duboscq, 2014] and samples of the simulation results in the Appendix ?? with more details.

In Sec. 5.4, we experimentally study Na-Rb droplet and measure the phase diagram of liquid-gas phase transition, which is the central part of our experimental research. The experimental method is simple and straightforward. We directly let the sample do Time-of-Flight and observe the non-expansion signal. This method avoids the complexity of the optical-levitation method however need more effort to eliminate the inhomogeneity of the magnetic field. In order to cooperate with this scheme, we upgrade our system on both control of magnetic field and imaging method, referring to Sec. 3.2 and Sec. 3.4 for details. Later, in Sec. 5.5, we study the gaseous LHY sample. This research aims to explore the behaviour of a gaseous sample under the dominance of LHY energy instead of MF energy. This research is a supplement to the study of LHY gas by measuring the trap frequency [Skov et al., 2021]. After understanding the droplet formation process, we realize that the previous process of preparing droplets is far from adiabatic, which resulted in significant limitations on the sample life and the number of atoms. So we improve the preparation scheme to achieve a droplet sample with more numbers as shown in Sec. 5.6. Finally, Sec. 5.7 shows our efforts on using droplets to form the Feshbach molecules. Although the conversion efficiency has no improvement, we have greatly reduced the temperature of the molecules and provide a promising path for the future production of degenerate Feshbach molecules.

5.1 Quantum droplet with finite size

In Sec. 2.2, we calculate the quantum liquid analytically, showing the mean-field and LHY energy expressions. Then we obtain the equilibrium density of the system. This calculation ignores the system's quantum pressure (kinetic energy), which means it is only proper for homogeneous bulk samples. However, in our experiments, due to the limitation of the atomic number, we currently cannot obtain a sample with a large enough number allowing us to ignore its edge. Thus, in this section, we first

analyse the quantum pressure caused by the finite volume then show its influence on the quantum liquid droplet.

The total energy of the system consists of three parts; in addition to the interaction energy (Mean-field energy and LHY correction), there is also the quantum pressure due to the finite size of the sample. This can also be explained by the uncertainty principle since the finite size can be viewed as a size limitation and will introduce a finite momentum (energy). The total energy expression of this finite-size droplet sample is

$$\begin{aligned} E_{\text{total}} &= E_{\text{kin}} + E_{\text{MF}} + E_{\text{LHY}} \\ E_{\text{kin}} &= N \frac{\hbar^2}{2m} \int |\nabla \phi(\mathbf{r})|^2 dr^3 \\ E_{\text{MF}} &= \frac{g}{2} N^2 \int |\phi(\mathbf{r})|^4 dr^3, \quad g = \frac{2\pi\hbar^2 a_S}{m/2} \end{aligned} \quad (5.1)$$

where N is particle number, m is its mass, g is the interaction strength which is proportional to scattering length a_S . Note that here we write down the formula with only single species, however later we need to extend it to double species case, which is just summation along two species for all N and g_{ij} . The LHY correction expression needs an infinite integration which is will be explained later.

Locally, MF energy is proportional to n^2 , and LHY correction is proportional to $n^{5/2}$. The kinetic energy (quantum pressure) is proportional to the square of the derivation of the wave function. For a homogeneous bulk sample, just as we mentioned in Chap. 2, the quantum pressure term is zero. However, considering a finite size sample, the rapid decreasing of the wave function on the boundary (the density inside is limited and the outside is the vacuum) introduces additional kinetic energy. This kinetic energy tends to reduce the variation rate of the wave function (density) on the boundary. So it tends to inflate the sample. This term does not exist in a classic system but only in a quantum system which is the same as the LHY term.

Another phenomenon called surface tension can be explained by MF energy on the boundary. At the boundary, density is lower than at the core part, and the positive energy of LHY is much smaller than the attraction energy of MF. So the attraction force is dominated by MF energy and offer surface tension similar to the classical liquid. From another perspective, MF energy is a zero-order approximation, both existing in classical and quantum systems. This surface tension will cause the pressure at the core to be higher than the homogeneous sample. In the finite droplet case, because the environment is with zero pressure, thus the core of the sample will have a pressure higher than zero. This can be offered by the LHY term, as we mentioned in Chap. 2, the LHY term increase faster than the MF term with increasing density. So, the LHY repulsion overcomes the MF attraction at the core and support the sample without collapsing.

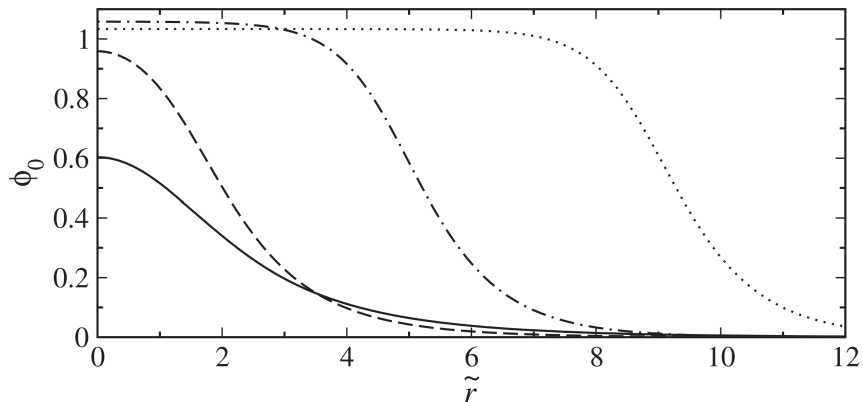


Figure 5.1: Figure shows the density distribution of a finite-size droplet. The edge size is of about one \hat{r} which provides the surface tension. Figure from [Petrov, 2015].

In addition to the quantum droplet of free space, we also discuss the sample of in trap. For the in-trap sample, we need to add an additional energy term of the trap. So, the total energy is made of four parts now. For a sample with finite size, trap energy and quantum pressure behaves opposite. Small size introduces higher quantum pressure but reduces trap energy and vice versa. This is similar for MF and LHY

energy, where MF energy is negative; however, LHY energy is positive. For samples with specific sizes, these two-term compete with each other. Analyzing such a sample with two groups of energies competing with each other is not straightforward. Therefore, the calculation of the variational method we introduced in Sec. 5.2 can help us understand better. This part is explained carefully in sec. For more detailed calculations, please refer to [Hu and Liu, 2020a].

5.2 Variational calculation

In this section, we introduce the variational calculation of droplets. Variational calculations can help us better understand the energy competition in the system. From the analysis in the previous section, we can read that whatever the quantum pressure or the interaction energy in a quantum droplet of finite volume, they all depend on the system's wave function distribution. Thus, a pure analytical calculation lacks information and can not reveal how these different energies compete with each other.

A more accurate method is the finite element method, which treats the entire wave function as a function of space coordinates. Then it uses a variational method to adjust the value of the wave function at each spatial position, reducing the overall system's energy, thereby providing a more accurate solution. However, the calculation of the three-dimensional system consumes vast computing resources, which is incapable of ordinary personal computers. In order to understand the behaviour of the system, we need an intermediate model to help us establish the relationship between various causes and effects. After this step, the subsequent GPE simulation will be more straightforward.

This section first reviews the variational calculation of single species BEC and defines the so-called release energy. We explain how release energy reflects the interaction and the measurement of the second-order correlation function. At the same time, this also gives an experimental measurement method, i.e. the direct TOF

method. Then we show the introduction of the Gaussian variational method in the double-species system. Although it is a very rough approximation, the calculation should be pretty effective for the case with a relatively small atomic number and the droplet sample far away from the top-flat density distribution at the centre. This will be verified in subsequent calculations. We imitate the dimensionless parameters of the single-species BEC and introduce two dimensionless parameters to characterize the double-species BEC in the trap. Thereby it is convenient to describe the system and compare it with different species combinations.

We calculate two items by the variational method: 1. LHY gas in a harmonic trap and the released energy when expansion in free-space. 2. Droplet with magnetic field gradient and how the critical number is shifting. We start from a single BEC in a harmonic trap and review the variational method with Gaussian Ansatz. Noted that, we get the $\chi = -0.67$ there is a collapse point, which offers no solution. Then, we plot the release energy curve. The release energy is just the sum of kinetic energy in the trap plus the interaction energy. For the Double BEC near-zero MF energy, the behaviour of the sample is very similar to a single BEC, as the λ_+ branch requires minimum density, leaving only the λ_- branch. So, assuming that Na and Rb share the same wave function, we can use the result from the single BEC part. By choosing the correct characteristic value, we can make a comparison for experimental data.

We also use the eGPE to calculate the release energy in Sec. 5.3, due to Gaussian Ansatz does not fit for large atomic number cases. We find a great overlap between our experiment and the eGPE simulation. In comparing the MF and LHY cases, we can say that we measured the LHY energy for the zero-MF with a shift from $0.75\hbar\omega$ to about $1.3\hbar\omega$. This relatively large shift is definite beyond MF theory. The eGPE simulation cannot give out physics explanation. However, the variational method can. So, we plot all kinds of energy as a function of the variational parameter w . This plot can explain several questions: 1. How do these different energies compete?

What is the meaning of the meta-stable state of a droplet? 2. What parameter do we need to characterize the LHY term? Moreover, how large is this term compared to the MF term and others? 3. what will happen if the initial state does not match the droplet state? Will the expansion over the local maximum and miss the droplet formation?

Finally, we add one more variational parameter to the Gaussian Ansatz to explain the shift of critical numbers when the magnetic field gradient exists. The main idea is that Na and Rb wavefunction will suffer a tiny centre shifting δ , which decrease the absolute value of Mean-Field energy between Na and Rb. Because the E_{MF_Rb-Na} is the product of their density. So the overlap will change dramatically. However, The rest part of MF and LHY energy will keep. So, this gradient will decrease the binding term when we are in the droplet region, which shifts the critical number above.

5.2.1 Single species BEC in harmonic trap

We first recall the textbook result of the variational solution about a single BEC in harmonic trap. Here, we introduce the Gaussian ansatz as an approximation. Considering N Bosons in a harmonic trap with trap frequency of ω_0 , its ground state energy is made of

$$\begin{aligned} E_{\text{kin}} &= N \frac{\hbar^2}{2m} \int |\nabla \phi(\mathbf{r})|^2 dr^3 \\ E_{\text{trap}} &= N \int |\phi(\mathbf{r})|^2 V_{\text{trap}}(\mathbf{r}) dr^3, \quad V_{\text{trap}}(\mathbf{r}) = \frac{1}{2} m \omega_0^2 \mathbf{r}^2 \\ E_{\text{MF}} &= \frac{g}{2} N^2 \int |\phi(\mathbf{r})|^4 dr^3, \quad g = \frac{2\pi\hbar^2 a_S}{m/2} \end{aligned} \quad (5.2)$$

where we for now ignore the LHY correction. For convenience we define the harmonic length $a_{\text{ho}} = \sqrt{\frac{\hbar}{m\omega_0}}$.

Now, we use variational method to calculate the wave-function in trap. the Gaus-

sian ansatz is

$$\phi(\mathbf{r}) = \frac{1}{\pi^{3/4} (w^3 a_{\text{ho}}^3)^{1/2}} e^{-\frac{\mathbf{r}^2}{2w^2 a_{\text{ho}}^2}} \quad (5.3)$$

where the w is the variational parameter. Then, we have

$$\begin{aligned} E_{\text{kin}} &= N \frac{\hbar^2}{2m} \int |\nabla \phi(\mathbf{r})|^2 dr^3 = N \hbar \omega_0 \frac{3}{4w^2} \\ E_{\text{trap}} &= N \int |\phi(\mathbf{r})|^2 V_{\text{trap}}(\mathbf{r}) dr^3 = N \hbar \omega_0 \left(\frac{3}{4} w^2 \right) \\ E_{\text{MF}} &= \frac{g}{2} N^2 \int |\phi(\mathbf{r})|^4 dr^3 = N \hbar \omega_0 \left(\frac{1}{\sqrt{2\pi}} \frac{a_S N}{a_{\text{ho}}} \frac{1}{w^3} \right) \end{aligned} \quad (5.4)$$

i.e. total energy

$$E_{\text{tot}}(w) = N \hbar \omega_0 \left(\frac{3}{4} \frac{1}{w^2} + \frac{3}{4} w^2 + \frac{1}{\sqrt{2\pi}} \frac{a_S N}{a_{\text{ho}}} \frac{1}{w^3} \right) \quad (5.5)$$

Then we minimize the E_{tot} with the constrain of $\int \phi \phi^* dr^3 = N$

$$E_{\text{tot}}(w) - \mu N = N \hbar \omega_0 \left(\frac{3}{4} \frac{1}{w^2} + \frac{3}{4} w^2 + \frac{1}{\sqrt{2\pi}} \frac{a_S N}{a_{\text{ho}}} \frac{1}{w^3} \right) - \mu N \quad (5.6)$$

To get the w of ground state, we take the derivative of E_{tot}

$$\partial_w \left(\frac{3}{4} \frac{1}{w^2} + \frac{3}{4} w^2 + \frac{1}{\sqrt{2\pi}} \frac{\chi}{w^3} \right) = -\frac{3}{2w^3} + \frac{3w}{2} - \frac{3\chi}{\sqrt{2\pi} w^4} \quad (5.7)$$

where we use χ represent the dimensionless quantity $\frac{a_S N}{a_{\text{ho}}}$.

- If tuning $g = 0$, i.e. the non-interacting case, we get back to the single particle picture. The wave-function is a Gaussian with size of harmonic length, i.e. $w = 1$
- With increasing χ , we have larger size (larger w), and finally, when reach $\chi \gg 1$ limit, we turn to the Thomas-Fermi limit.
- For $\chi < 0$, we have attractive Bose gas, with collapse point at $\chi = -0.671$ []

5.2.2 Double BEC in harmonic trap with near zero-MF interaction

Now we turn to our double species case, i.e. N_{Rb} Rb and N_{Na} Na in a harmonic trap with trap frequency of ω_{Rb} and ω_{Na} , we have ground state energy of

$$\begin{aligned} E_{\text{kin}} &= N_{\text{Na}} \frac{\hbar^2}{2m_{\text{Na}}} \int |\nabla \phi_{\text{Na}}(\mathbf{r})|^2 dr^3 + N_{\text{Rb}} \frac{\hbar^2}{2m_{\text{Rb}}} \int |\nabla \phi_{\text{Rb}}(\mathbf{r})|^2 dr^3 \\ E_{\text{trap}} &= N_{\text{Na}} \int |\phi_{\text{Na}}(\mathbf{r})|^2 V_{\text{trap-Na}}(\mathbf{r}) dr^3 + N_{\text{Rb}} \int |\phi_{\text{Rb}}(\mathbf{r})|^2 V_{\text{trap-Rb}}(\mathbf{r}) dr^3 \\ E_{\text{MF}} &= \frac{g_{\text{Na}}}{2} N_{\text{Na}}^2 \int |\phi_{\text{Na}}(\mathbf{r})|^4 dr^3 + \frac{g_{\text{Rb}}}{2} N_{\text{Rb}}^2 \int |\phi_{\text{Rb}}(\mathbf{r})|^4 dr^3 \\ &\quad + g_{\text{Rb},\text{Na}} N_{\text{Na}} N_{\text{Rb}} \int |\phi_{\text{Rb}}(\mathbf{r})|^2 |\phi_{\text{Na}}(\mathbf{r})|^2 dr^3 \\ E_{\text{LHY}} &= \int \frac{256\sqrt{\pi}\hbar^2}{15} \left(m_{\text{Na}}^{-2/5} a_{\text{Na}} |\phi_{\text{Na}}(\mathbf{r})|^2 + m_{\text{Rb}}^{-2/5} a_{\text{Rb}} |\phi_{\text{Rb}}(\mathbf{r})|^2 \right)^{5/2} dr^3 \end{aligned} \quad (5.8)$$

where

$$\begin{aligned} V_{\text{trap-Rb}}(\mathbf{r}) &= \frac{1}{2} m_{\text{Rb}} \omega_{\text{Rb}}^2 \mathbf{r}^2, V_{\text{trap-Na}}(\mathbf{r}) = \frac{1}{2} m_{\text{Na}} \omega_{\text{Na}}^2 \mathbf{r}^2 \\ g_{\text{Rb}} &= \frac{2\pi\hbar^2 a_{\text{Rb}}}{m_{\text{Rb}}/2}, g_{\text{Na}} = \frac{2\pi\hbar^2 a_{\text{Na}}}{m_{\text{Na}}/2}, g_{\text{Rb},\text{Na}} = \frac{2\pi\hbar^2 a_{\text{Rb},\text{Na}}}{m_{\text{Rb}} m_{\text{Na}} / (m_{\text{Rb}} + m_{\text{Na}})} \end{aligned} \quad (5.9)$$

As we are dealing with the case of $E_{\text{MF}} \rightarrow 0$, we can make several approximation:

- Two BECs share the same wave-function $\phi(\mathbf{r})$
- Gaussian Ansatz

With the first approximation, we can rewrite the Hamiltonian as

$$\begin{aligned} E_{\text{kin}} &= \left(\frac{N_{\text{Na}}}{m_{\text{Na}}} + \frac{N_{\text{Rb}}}{m_{\text{Rb}}} \right) \frac{\hbar^2}{2} \int |\nabla \phi(\mathbf{r})|^2 dr^3 = \frac{N \hbar^2}{m} \frac{2}{2} \int |\nabla \phi(\mathbf{r})|^2 dr^3 \\ E_{\text{trap}} &= \frac{1}{2} (m_{\text{Rb}} \omega_{\text{Rb}}^2 N_{\text{Rb}} + m_{\text{Na}} \omega_{\text{Na}}^2 N_{\text{Na}}) \int |\phi(\mathbf{r})|^2 \mathbf{r}^2 dr^3 = \frac{1}{2} m \omega^2 N \int |\phi(\mathbf{r})|^2 \mathbf{r}^2 dr^3 \\ E_{\text{MF}} &= \frac{g_{\text{Na}} N_{\text{Na}}^2 + g_{\text{Rb}} N_{\text{Rb}}^2 + 2g_{\text{Rb},\text{Na}} N_{\text{Na}} N_{\text{Rb}}}{2} \int |\phi(\mathbf{r})|^4 dr^3 = \frac{g}{2} N^2 \int |\phi(\mathbf{r})|^4 dr^3 \\ E_{\text{LHY}} &= \frac{8 \left(m_{\text{Na}}^{3/5} g_{\text{Na}} N_{\text{Na}} + m_{\text{Rb}}^{3/5} g_{\text{Rb}} N_{\text{Rb}} \right)^{5/2}}{15\pi^2\hbar^3} \int |\phi(\mathbf{r})|^5 dr^3 = \frac{8m^{3/2} \Gamma^{5/2} N^{5/2}}{15\pi^2\hbar^3} \int |\phi(\mathbf{r})|^5 dr^3 \end{aligned}$$

Now, we recover to the single component case, with new mass, number, trap frequency and interaction strength following **the negative branch** as shown in [Petrov, 2015]

$$E_{\text{MF}-} = \lambda_- n_-^2, \quad \text{with} \quad \lambda_- = \frac{\delta g \sqrt{g_{\text{Rb}} g_{\text{Na}}}}{(g_{\text{Na}} + g_{\text{Rb}})} \quad \text{and} \quad n_- = \frac{n_{\text{Rb}} \sqrt{g_{\text{Na}}} + n_{\text{Na}} \sqrt{g_{\text{Rb}}}}{\sqrt{g_{\text{Na}} + g_{\text{Rb}}}} \quad (5.10)$$

Thus, we can define the new number and interaction strength as

$$\begin{aligned} N &= N_- = \frac{N_{\text{Rb}} \sqrt{g_{\text{Na}}} + N_{\text{Na}} \sqrt{g_{\text{Rb}}}}{\sqrt{g_{\text{Na}} + g_{\text{Rb}}}} \\ g &= \frac{4\pi\hbar^2 a_S}{m} = 2\lambda_- = \frac{2\delta g \sqrt{g_{\text{Rb}} g_{\text{Na}}}}{(g_{\text{Na}} + g_{\text{Rb}})}, \quad \delta g = g_{\text{Rb},\text{Na}} + \sqrt{g_{\text{Rb}} g_{\text{Na}}} \end{aligned} \quad (5.11)$$

Then, we have

$$\begin{aligned} m &= \frac{N m_{\text{Na}} m_{\text{Rb}}}{N_{\text{Na}} m_{\text{Rb}} + N_{\text{Rb}} m_{\text{Na}}} \\ \omega &= \sqrt{\frac{(N_{\text{Na}} m_{\text{Rb}} + N_{\text{Rb}} m_{\text{Na}}) (m_{\text{Rb}} \omega_{\text{Rb}}^2 N_{\text{Rb}} + m_{\text{Na}} \omega_{\text{Na}}^2 N_{\text{Na}})}{N^2 m_{\text{Na}} m_{\text{Rb}}}} \\ \Gamma &= \frac{m_{\text{Na}}^{3/5} g_{\text{Na}} N_{\text{Na}} + m_{\text{Rb}}^{3/5} g_{\text{Rb}} N_{\text{Rb}}}{m^{3/5} N} = \frac{4\pi\hbar^2 A}{m} \end{aligned} \quad (5.12)$$

For convenience we define the harmonic length

$$a_{\text{ho}} = \sqrt{\frac{\hbar}{m\omega}} = \sqrt{\hbar \sqrt{\frac{N_{\text{Na}} m_{\text{Rb}} + N_{\text{Rb}} m_{\text{Na}}}{(m_{\text{Rb}} \omega_{\text{Rb}}^2 N_{\text{Rb}} + m_{\text{Na}} \omega_{\text{Na}}^2 N_{\text{Na}}) m_{\text{Na}} m_{\text{Rb}}}}} \quad (5.13)$$

With Gaussian Ansatz

$$\phi(\mathbf{r}) = \frac{1}{\pi^{3/4} (w^3 a_{\text{ho}}^3)^{1/2}} e^{-\frac{\mathbf{r}^2}{2w^2 a_{\text{ho}}^2}} \quad (5.14)$$

We get the similar formula as the single BEC near zero-MF point, and its total energy is

$$E_{\text{tot}}(w) = N\hbar\omega \left(\frac{3}{4} \frac{1}{w^2} + \frac{3}{4} w^2 + \frac{1}{\sqrt{2\pi}} \chi \frac{1}{w^3} + \frac{512}{75\pi^{7/4}} \sqrt{\frac{2}{5}} \xi \frac{1}{w^{9/2}} \right) \quad (5.15)$$

where

$$\chi = \frac{a_S N}{a_{\text{ho}}}, \xi = \left(\frac{A}{a_{\text{ho}}} \right)^{5/2} N^{3/2} \quad (5.16)$$

Released energy is

$$E_{\text{release}} = \frac{\left(\frac{3}{2}m_{\text{Rb}}N_{\text{Rb}}v_{\text{Rb}}^2 + \frac{3}{2}m_{\text{Na}}N_{\text{Na}}v_{\text{Na}}^2 \right)}{N} \quad (5.17)$$

$$\begin{aligned} \frac{E_{\text{release}}}{\hbar\omega_{\text{ho}}} &= \frac{\left(\frac{3}{2}m_{\text{Rb}}N_{\text{Rb}}v_{\text{Rb}}^2 + \frac{3}{2}m_{\text{Na}}N_{\text{Na}}v_{\text{Na}}^2 \right)}{N} \frac{1}{\hbar\sqrt{\frac{(N_{\text{Na}}m_{\text{Rb}}+N_{\text{Rb}}m_{\text{Na}})(m_{\text{Rb}}\omega_{\text{Rb}}^2N_{\text{Rb}}+m_{\text{Na}}\omega_{\text{Na}}^2N_{\text{Na}})}{N^2m_{\text{Na}}m_{\text{Rb}}}}} \\ &= \frac{(m_{\text{Rb}}N_{\text{Rb}}v_{\text{Rb}}^2 + m_{\text{Na}}N_{\text{Na}}v_{\text{Na}}^2)}{2\hbar} \frac{3\sqrt{m_{\text{Na}}m_{\text{Rb}}}}{\sqrt{(N_{\text{Na}}m_{\text{Rb}}+N_{\text{Rb}}m_{\text{Na}})(m_{\text{Rb}}\omega_{\text{Rb}}^2N_{\text{Rb}}+m_{\text{Na}}\omega_{\text{Na}}^2N_{\text{Na}})}} \end{aligned} \quad (5.18)$$

about the χ

$$\chi = \frac{a_S N}{a_{\text{ho}}} = \frac{g \frac{m_{\text{Na}}m_{\text{Rb}}}{N_{\text{Na}}m_{\text{Rb}}+N_{\text{Rb}}m_{\text{Na}}}}{4\pi\hbar^2} \frac{\left(\frac{N_{\text{Rb}}\sqrt{g_{\text{Na}}}+N_{\text{Na}}\sqrt{g_{\text{Rb}}}}{\sqrt{g_{\text{Na}}+g_{\text{Rb}}}} \right)^2}{\sqrt{\hbar\sqrt{\frac{N_{\text{Na}}m_{\text{Rb}}+N_{\text{Rb}}m_{\text{Na}}}{(m_{\text{Rb}}\omega_{\text{Rb}}^2N_{\text{Rb}}+m_{\text{Na}}\omega_{\text{Na}}^2N_{\text{Na}})m_{\text{Na}}m_{\text{Rb}}}}}} \quad (5.19)$$

about the ξ

$$\xi = \left(\frac{A}{a_{\text{ho}}} \right)^{5/2} N^{3/2} = \left(\frac{\left(\frac{m_{\text{Na}}m_{\text{Rb}}}{N_{\text{Na}}m_{\text{Rb}}+N_{\text{Rb}}m_{\text{Na}}} \right)^{2/5}}{4\pi\hbar^2} - \frac{m_{\text{Na}}^{3/5}g_{\text{Na}}N_{\text{Na}} + m_{\text{Rb}}^{3/5}g_{\text{Rb}}N_{\text{Rb}}}{\sqrt{\hbar\sqrt{\frac{N_{\text{Na}}m_{\text{Rb}}+N_{\text{Rb}}m_{\text{Na}}}{(m_{\text{Rb}}\omega_{\text{Rb}}^2N_{\text{Rb}}+m_{\text{Na}}\omega_{\text{Na}}^2N_{\text{Na}})m_{\text{Na}}m_{\text{Rb}}}}}} \right)^{5/2} \quad (5.20)$$

5.2.3 How magnetic field gradient affect droplet

When we put N_{Rb} Rb and N_{Na} Na in free space, with magnetic gradient ∇B , we take the center-of-mass as original point. Consider gradient force

$$F = N_{\text{Rb}}\mu_{\text{Rb}}\nabla B + N_{\text{Na}}\mu_{\text{Na}}\nabla B \quad (5.21)$$

The acceleration of whole sample is

$$\mathcal{A}_{\text{center of mass}} = F/m = \frac{N_{\text{Rb}}\mu_{\text{Rb}} + N_{\text{Na}}\mu_{\text{Na}}}{N_{\text{Rb}}m_{\text{Rb}} + N_{\text{Na}}m_{\text{Na}}} \nabla B \quad (5.22)$$

So, in the coordinate of center of mass, we have Na and Rb with acceleration on different direction

$$\mathcal{A}_{\text{Rb}} = \frac{\mu_{\text{Rb}} \nabla B}{m_{\text{Rb}}} - \frac{N_{\text{Rb}}\mu_{\text{Rb}} \nabla B + N_{\text{Na}}\mu_{\text{Na}} \nabla B}{N_{\text{Rb}}m_{\text{Rb}} + N_{\text{Na}}m_{\text{Na}}} \quad (5.23)$$

$$\mathcal{A}_{\text{Na}} = \frac{\mu_{\text{Na}} \nabla B}{m_{\text{Na}}} - \frac{N_{\text{Rb}}\mu_{\text{Rb}} \nabla B + N_{\text{Na}}\mu_{\text{Na}} \nabla B}{N_{\text{Rb}}m_{\text{Rb}} + N_{\text{Na}}m_{\text{Na}}} \quad (5.24)$$

and their relationship is

$$m_{\text{Rb}}\mathcal{A}_{\text{Rb}}N_{\text{Rb}} = -m_{\text{Na}}\mathcal{A}_{\text{Na}}N_{\text{Na}} \quad (5.25)$$

Now, we can take gradient as an external field and the formula of the energy coming from this gradient is

$$E_{\text{gradient}} = N_{\text{Na}}m_{\text{Na}}\mathcal{A}_{\text{Na}} \int |\phi_{\text{Na}}(\mathbf{r})|^2 dr^3 + N_{\text{Rb}}m_{\text{Rb}}\mathcal{A}_{\text{Rb}} \int |\phi_{\text{Rb}}(\mathbf{r})|^2 dr^3 \quad (5.26)$$

Other terms of energy as following

$$\begin{aligned} E_{\text{kin}} &= N_{\text{Na}} \frac{\hbar^2}{2m_{\text{Na}}} \int |\nabla \phi_{\text{Na}}(\mathbf{r})|^2 dr^3 + N_{\text{Rb}} \frac{\hbar^2}{2m_{\text{Rb}}} \int |\nabla \phi_{\text{Rb}}(\mathbf{r})|^2 dr^3 \\ E_{\text{trap}} &= N_{\text{Na}} \int |\phi_{\text{Na}}(\mathbf{r})|^2 V_{\text{trap-Na}}(\mathbf{r}) dr^3 + N_{\text{Rb}} \int |\phi_{\text{Rb}}(\mathbf{r})|^2 V_{\text{trap-Rb}}(\mathbf{r}) dr^3 \\ E_{\text{MF}} &= \frac{g_{\text{Na}}}{2} N_{\text{Na}}^2 \int |\phi_{\text{Na}}(\mathbf{r})|^4 dr^3 + \frac{g_{\text{Rb}}}{2} N_{\text{Rb}}^2 \int |\phi_{\text{Rb}}(\mathbf{r})|^4 dr^3 \\ &\quad + g_{\text{Rb},\text{Na}} N_{\text{Na}} N_{\text{Rb}} \int |\phi_{\text{Rb}}(\mathbf{r})|^2 |\phi_{\text{Na}}(\mathbf{r})|^2 dr^3 \\ E_{\text{LHY}} &= \int \frac{256\sqrt{\pi}\hbar^2}{15} \left(m_{\text{Na}}^{-2/5} a_{\text{Na}} |\phi_{\text{Na}}(\mathbf{r})|^2 + m_{\text{Rb}}^{-2/5} a_{\text{Rb}} |\phi_{\text{Rb}}(\mathbf{r})|^2 \right)^{5/2} dr^3 \end{aligned} \quad (5.27)$$

where

$$\begin{aligned}
 V_{\text{trap-Rb}}(\mathbf{r}) &= \frac{1}{2}m_{\text{Rb}}\omega_{\text{Rb}}^2\mathbf{r}^2 \\
 V_{\text{trap-Na}}(\mathbf{r}) &= \frac{1}{2}m_{\text{Na}}\omega_{\text{Na}}^2\mathbf{r}^2 \\
 g_{\text{Rb}} &= \frac{2\pi\hbar^2a_{\text{Rb}}}{m_{\text{Rb}}/2} \\
 g_{\text{Na}} &= \frac{2\pi\hbar^2a_{\text{Na}}}{m_{\text{Na}}/2} \\
 g_{\text{Rb,Na}} &= \frac{2\pi\hbar^2a_{\text{Rb,Na}}}{m_{\text{Rb}}m_{\text{Na}}/(m_{\text{Rb}}+m_{\text{Na}})}
 \end{aligned} \tag{5.28}$$

Gaussian Ansatz with center shifts

$$\begin{aligned}
 \phi_{\text{Na}}(x, y, z) &= \frac{1}{\pi^{3/4}(w^3a_{\text{ho}}^3)^{1/2}}e^{-\frac{x^2+\left(y-\frac{m_{\text{Rb}}N_{\text{Rb}}\delta_y}{m_{\text{Rb}}N_{\text{Rb}}+m_{\text{Na}}N_{\text{Na}}}\right)^2+z^2}{2w^2a_{\text{ho}}^2}} \\
 \phi_{\text{Rb}}(x, y, z) &= \frac{1}{\pi^{3/4}(w^3a_{\text{ho}}^3)^{1/2}}e^{-\frac{x^2+\left(y+\frac{m_{\text{Na}}N_{\text{Na}}\delta_y}{m_{\text{Rb}}N_{\text{Rb}}+m_{\text{Na}}N_{\text{Na}}}\right)^2+z^2}{2w^2a_{\text{ho}}^2}}
 \end{aligned} \tag{5.29}$$

Then, we have

$$\begin{aligned}
 E_{\text{kin}} &= N_{\text{Na}}\frac{\hbar^2}{2m_{\text{Na}}}\int|\nabla\phi_{\text{Na}}(\mathbf{r})|^2dr^3 + N_{\text{Rb}}\frac{\hbar^2}{2m_{\text{Rb}}}\int|\nabla\phi_{\text{Rb}}(\mathbf{r})|^2dr^3 \\
 E_{\text{trap}} &= \frac{1}{2}(m_{\text{Rb}}\omega_{\text{Rb}}^2N_{\text{Rb}}+m_{\text{Na}}\omega_{\text{Na}}^2N_{\text{Na}})\int|\phi(\mathbf{r})|^2\mathbf{r}^2dr^3 = \frac{1}{2}m\omega^2N\int|\phi(\mathbf{r})|^2\mathbf{r}^2dr^3 \\
 E_{\text{MF}} &= \frac{g_{\text{Na}}N_{\text{Na}}^2+g_{\text{Rb}}N_{\text{Rb}}^2+2g_{\text{Rb,Na}}N_{\text{Na}}N_{\text{Rb}}}{2}\int|\phi(\mathbf{r})|^4dr^3 = \frac{g}{2}N^2\int|\phi(\mathbf{r})|^4dr^3 \\
 E_{\text{LHY}} &= \frac{8}{15\pi^2\hbar^3}\left(m_{\text{Na}}^{3/5}g_{\text{Na}}N_{\text{Na}}+m_{\text{Rb}}^{3/5}g_{\text{Rb}}N_{\text{Rb}}\right)^{5/2}\int|\phi(\mathbf{r})|^5dr^3 \\
 &= \frac{8}{15\pi^2\hbar^3}m^{3/2}\Gamma^{5/2}N^{5/2}\int|\phi(r)|^5dr^3
 \end{aligned} \tag{5.30}$$

Put the center shift Gaussian into it, we have

$$\begin{aligned} E_{\text{tot}}[w] = & N\hbar\omega \left((-\mu_{\text{eff}}\nabla B)\delta + \frac{3}{4}\frac{1}{w^2} + \frac{3}{4}w^2 + \frac{1}{\sqrt{2\pi}}\frac{a_S N}{a_{\text{ho}}} \frac{1}{w^3} (\lambda e^{-\delta^2}) \right. \\ & \left. + \frac{512}{75\pi^{7/4}} \sqrt{\frac{2}{5}} \left(\frac{A}{a_{\text{ho}}}\right)^{5/2} N^{3/2} \frac{1}{w^{9/2}} \right) \end{aligned} \quad (5.31)$$

When, δ is a small value, we have $e^{-\delta^2} = 1 - \delta^2$, thus we have

$$\begin{aligned} E_{\text{tot}}[w] = & N\hbar\omega \left[\left(\frac{3}{4}\frac{1}{w^2} + \frac{3}{4}w^2 + \frac{1}{\sqrt{2\pi}}\chi \frac{1}{w^3} + \frac{512}{75\pi^{7/4}} \sqrt{\frac{2}{5}}\xi \frac{1}{w^{9/2}} \right) \right. \\ & \left. + \lambda\delta^2 - (\mu_{\text{eff}}\nabla B)\delta \right] \end{aligned} \quad (5.32)$$

where

$$\begin{aligned} \chi &= \frac{a_S N}{a_{\text{ho}}} \\ \xi &= \left(\frac{A}{a_{\text{ho}}}\right)^{5/2} N^{3/2} \end{aligned} \quad (5.33)$$

5.3 extended GPE solution

Although the variational method used in the previous section provides a general physical image, the method will get meaningless results when the system deviates from the reasonable parameter interval because we use a rough Gauss ansatz. So we need more accurate numerical calculations to compare with experimental data. Since quantum depletion takes only a tiny portion of our system, it is reasonable to use the local density approximation to calculate the wave function of the condensate part. Therefore, we only need to add LHY correction to the MF shift as a high-level correction, then use this extended GPE to calculate the system to get the condensate wave function of the system.

In this section, let us first revisit the calculation of MF and LHY correction of the double BEC system. Then we first derive the single species GPE. Then imitating

this process, the derivation of the extended GPE of double-species is provided. When calculating the LHY correction, if we adopt the method of infinite integration, the amount of calculation will increase. So we imitated [Minardi et al., 2019] and adopted an approximation with an error of less than 15%. The rationality of this approximation essentially stems from the symmetry of exchanging two species. If two species have the same mass, such as two spin states of the same atomic species, the approximation gets back to the analytical solution as shown in [Petrov, 2015].

Hamiltonian for BEC with two components is

$$\begin{aligned} H_{\text{tot}} = & \sum_k \epsilon_{1,k} \hat{a}_{1,k}^\dagger \hat{a}_{1,k} + \frac{g_{11}}{2V} \sum_{\{k_i\}} \hat{a}_{1,k_1}^\dagger \hat{a}_{1,k_2}^\dagger \hat{a}_{1,k_3} \hat{a}_{1,k_4} + \sum_k \epsilon_{2,k} \hat{a}_{2,k}^\dagger \hat{a}_{2,k} \\ & + \frac{g_{22}}{2V} \sum_{\{k_i\}} \hat{a}_{2,k_1}^\dagger \hat{a}_{2,k_2}^\dagger \hat{a}_{2,k_3} \hat{a}_{2,k_4} + \frac{g_{12}}{V} \sum_{\{k_i\}} \hat{a}_{2,k_1}^\dagger \hat{a}_{1,k_2}^\dagger \hat{a}_{1,k_3} \hat{a}_{2,k_4} \end{aligned} \quad (5.34)$$

where $k_1 + k_2 = k_3 + k_4$, satisfy momentum conservation. g_{ii} represent intra-interaction strength, and g_{12} for inter-interaction. $\hat{a}_{i,k}^\dagger (\hat{a}_{i,k})$ denote the ladder operator for i^{th} component, i.e.

$$\hat{a}_{i,0} = \sqrt{N_i} \quad (5.35)$$

As calculated in Chap. 2, ground state energy is

$$\begin{aligned} E_{\text{GS}} = & \frac{g_{11}N_1^2 + g_{22}N_2^2 + 2g_{12}N_1N_2}{2V} \\ & + \frac{1}{2} \sum_{k \neq 0} \left(E_+ + E_- - \frac{\hbar^2 k^2}{2m_1} - \frac{\hbar^2 k^2}{2m_2} - \frac{g_{11}N_1 + g_{22}N_2}{V} \right) \end{aligned} \quad (5.36)$$

After re-normalization we have the second term, called LHY correction, which can

be rewritten with as

$$\begin{aligned}
\mathcal{E}_{\text{LHY}} = & C_1 \int_0^\infty \frac{15}{32} \tilde{k}^2 \left\{ \sqrt{\left[\frac{1}{2} \left(\frac{\tilde{k}^2}{2} \left(\frac{\tilde{k}^2}{2} + 2 \right) + \frac{1}{\gamma^2} \frac{\tilde{k}^2}{2} \left(\frac{\tilde{k}^2}{2} + 2y\gamma \right) \right) \right.} \right. \\
& \left. \left. + \sqrt{\left(\frac{1}{2} \left(\frac{\tilde{k}^2}{2} \left(\frac{\tilde{k}^2}{2} + 2 \right) - \frac{1}{\gamma^2} \frac{\tilde{k}^2}{2} \left(\frac{\tilde{k}^2}{2} + 2y\gamma \right) \right) \right)^2 + \frac{xy}{\gamma} \tilde{k}^4} \right] \right. \\
& \left. + \sqrt{\left[\frac{1}{2} \left(\frac{\tilde{k}^2}{2} \left(\frac{\tilde{k}^2}{2} + 2 \right) + \frac{1}{\gamma^2} \frac{\tilde{k}^2}{2} \left(\frac{\tilde{k}^2}{2} + 2y\gamma \right) \right) \right.} \right. \\
& \left. \left. - \sqrt{\left(\frac{1}{2} \left(\frac{\tilde{k}^2}{2} \left(\frac{\tilde{k}^2}{2} + 2 \right) - \frac{1}{\gamma^2} \frac{\tilde{k}^2}{2} \left(\frac{\tilde{k}^2}{2} + 2y\gamma \right) \right) \right)^2 + \frac{xy}{\gamma} \tilde{k}^4} \right] \right. \\
& \left. - \frac{\tilde{k}^2}{2} \left(1 + \frac{1}{\gamma} \right) - 1 - y + \frac{1 + \gamma y^2 + \frac{4xy\gamma}{1+\gamma}}{\tilde{k}^2} \right\} d\tilde{k}
\end{aligned} \tag{5.37}$$

where

$$\begin{aligned}
C_1 &= \frac{8}{15\pi^2} g_{11} n_1 \left(\frac{\sqrt{m_1 g_{11} n_1}}{\hbar} \right)^3, \gamma = \frac{m_2}{m_1}, \\
x &= \frac{g_{12}^2}{g_{11} g_{22}}, y = \frac{g_{22} n_2}{g_{11} n_1}, \tilde{k} = \frac{\hbar k}{\sqrt{m_1 g_{11} n_1}}
\end{aligned} \tag{5.38}$$

using

$$f \left(\frac{m_2}{m_1}, \frac{g_{12}^2}{g_{11} g_{22}}, \frac{g_{22} n_2}{g_{11} n_1} \right) \tag{5.39}$$

replacing the tedious integral, we have

$$\mathcal{E}_{\text{LHY}} = \frac{8}{15\pi^2} \frac{m_1^{3/2} (g_{11} n_1)^{5/2}}{\hbar^3} f(\gamma, x, y) \tag{5.40}$$

Now, we calculate $f(\gamma, x, y)$ numerically for our Rb-Na Bose mixture system. First we do this integration and check its convergence. We plot $f(\gamma, x, y)$ with increasing upper bound of integration k_C to test its convergence, as shown in Fig. 5.2. We can say that integration up to order of 6 has converged. Then, we calculate $f(\gamma, x, y)$

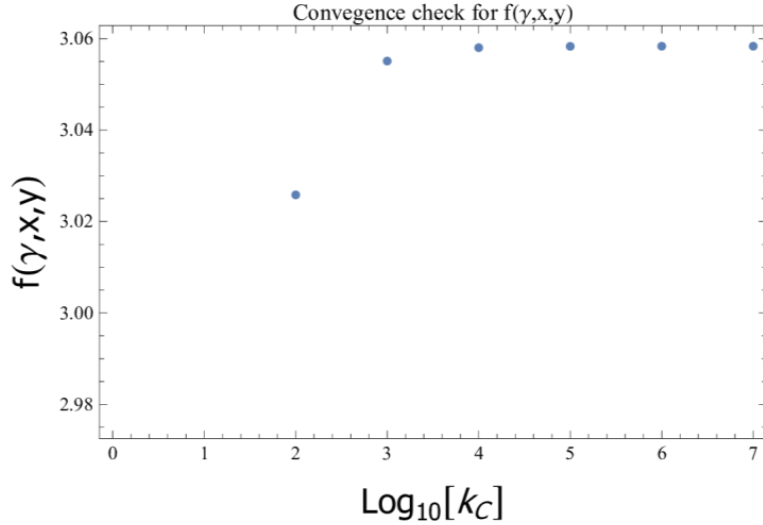


Figure 5.2: Convergence test of $f(\gamma, x, y)$

with different x , i.e. with different B-field. Compare with Minardi's approximation [Minardi et al., 2019], where they propose a analytical approximation which will be more convenient for deriving GPE with LHY correction. Here is the formula:

$$f(z, u = 1, x) \simeq (1 + z^{3/5}x)^{5/2} \quad (5.41)$$

where

$$z = m_2/m_1, x = \frac{g_{22}n_2}{g_{11}n_1}, u = \frac{g_{12}^2}{g_{11}g_{22}} \quad (5.42)$$

Here, u is set to be 1, because we only consider the case with near-zero MF energy, i.e. $g_{12} \approx \sqrt{g_{11}g_{22}}$. Now, we compare the numerical solution with the Minardi's approximation. Plot of List of $f(\gamma, x, y)$ for numerical one and Minardi's approximation. we can see that, there are mainly several percentage error by using this formula. And the maximum error is about 15%. So, keep this error in mind about the LHY energy. (as show in Fig. 5.3)

The subsequent GPE calculation requires a considerable amount of calculation. For example, for a 3D sample, if we split 2^7 in each direction, then the calculation

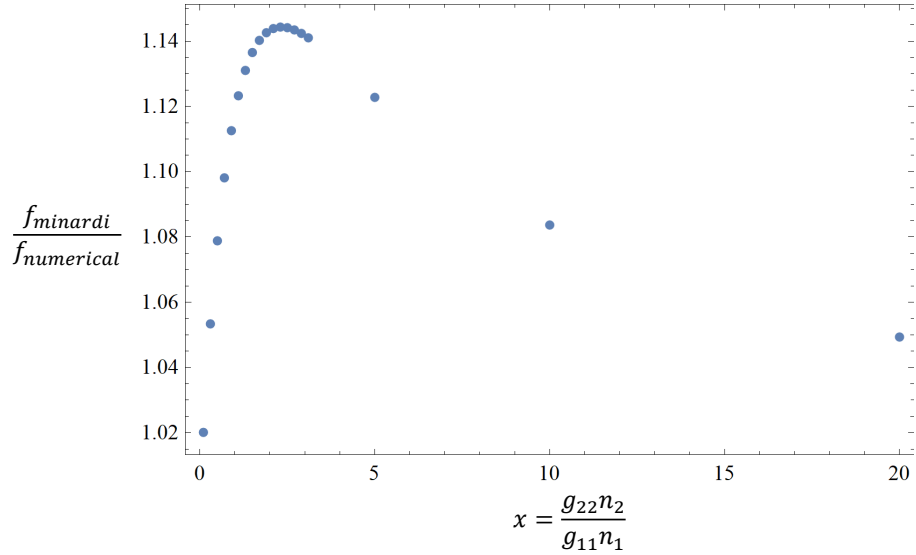


Figure 5.3: Compare the numerical solution and Minardi's approximation of $f(\gamma, x, y)$. The maximum deviation is about 15% when $g_{22}n_2/g_{11}n_1$ is around 2.

amount is to give an estimate. If the above infinite integral method is used to calculate the local of each grid LHY correction, then the amount of calculation will be huge. Therefore, if there is an analytical expression that can calculate the LHY correction, the amount of calculation will be significantly reduced. So Minardi approximation is a good starting point.

5.3.1 Derivation of GPE for single species BEC

First, we assume the many-body wave function is a product state

$$\Psi\left(\vec{r}_1, \vec{r}_2, \dots, \vec{r}_N\right) = \sum_{i=1}^N \psi\left(\vec{r}_i\right) \quad (5.43)$$

Then, we have

$$E(\psi, \psi^*) = N \int dr^3 \left(\frac{\hbar^2}{2m} |\nabla \psi(r)|^2 + V(r) |\psi(r)|^2 + \frac{1}{2} Ng |\psi(r)|^4 \right) \quad (5.44)$$

define the Variation

$$X(\psi, \psi^*) = E(\psi, \psi^*) - \mu N \int dr^3 |\psi(r)|^2 \quad (5.45)$$

take the variation of $X(\psi, \psi^*)$, we have

$$\begin{aligned} \delta X(\psi, \psi^*) &= N \int dr^3 \left[\frac{\hbar^2}{2m} (\nabla \psi^*(r) \nabla \delta \psi(r) + \nabla \psi(r) \nabla \delta \psi^*(r)) \right. \\ &\quad + (V(r) - \mu) (\psi^*(r) \delta \psi(r) + \psi(r) \delta \psi^*(r)) \\ &\quad \left. + Ng (\psi^2(r) \delta \psi^*(r) + \psi^{*2}(r) \delta \psi(r)) \right] \\ &= N \int dr^3 \left[\frac{\hbar^2}{2m} (\nabla \psi(r) \nabla \delta \psi^*(r)) + (V(r) - \mu) (\psi(r) \delta \psi^*(r)) \right. \\ &\quad \left. + Ng (\psi^2(r) \psi^*(r) \delta \psi^*(r)) \right] + c.c. \end{aligned} \quad (5.46)$$

for the first part, by using integrating by part method:

$$\begin{aligned} \int dr^3 (\nabla \psi(r) \nabla \delta \psi^*(r)) &= \delta \psi^*(r) \nabla \psi(r) |_0^\infty - \int dr^3 (\nabla^2 \psi(r) \delta \psi^*(r)) \\ &= \int dr^3 (-\nabla^2 \psi(r)) \delta \psi^*(r) \end{aligned} \quad (5.47)$$

Then, take the variance to be zero, we have GPE

$$\begin{aligned} -\frac{\hbar^2}{2m} (\nabla^2 \psi(r)) + (V(r) - \mu) \psi(r) + Ng (\psi^2(r) \psi^*(r)) &= 0 \\ -\frac{\hbar^2}{2m} (\nabla^2 \psi^*(r)) + (V(r) - \mu) \psi^*(r) + Ng (\psi^{*2}(r) \psi(r)) &= 0 \end{aligned} \quad (5.48)$$

5.3.2 Derivation of extended GPE for double species

First, we assume the many-body wave function is a product state

$$\Psi(\vec{r}_1, \vec{r}_2, \dots, \vec{r}_N) = \sum_{i=1}^N \psi(\vec{r}_i) \quad (5.49)$$

Then, we have

$$\begin{aligned} E(\psi, \psi^*) = & N \int dr^3 \left[\frac{\hbar^2}{2m} (\nabla \psi^*(r) \nabla \psi(r)) + V(r) (\psi^*(r) \psi(r)) \right. \\ & \left. + \frac{1}{2} N g (\psi^*(r) \psi(r))^2 + C (\psi^*(r) \psi(r))^{5/2} \right] \end{aligned} \quad (5.50)$$

define the Variation

$$X(\psi, \psi^*) = E(\psi, \psi^*) - \mu N \int dr^3 (\psi^*(r) \psi(r)) \quad (5.51)$$

take the variation of $X(\psi, \psi^*)$, we have

$$\begin{aligned} \delta X(\psi, \psi^*) = & N \int dr^3 \left[\frac{\hbar^2}{2m} (\nabla^2 \psi(r) \delta \psi^*(r)) + (V(r) - \mu) (\psi(r) \delta \psi^*(r)) \right. \\ & \left. + N g (\psi^2(r) \psi^*(r) \delta \psi^*(r)) + \frac{5C}{2} (\psi(r))^{5/2} (\psi^*(r))^{3/2} \delta \psi^*(r) \right] + c.c. \end{aligned} \quad (5.52)$$

where C is constants which already expressed the Last Part. thus, we have eGPE

$$-\frac{\hbar^2}{2m} \nabla^2 \psi(r) + (V(r) - \mu) \psi(r) + N g |\psi(r)|^2 \psi(r) + \frac{5C}{2} |\psi(r)|^3 \psi(r) = 0 \quad (5.53)$$

First, we assume the many-body wave function is a product state

$$\Psi(\vec{r}_1, \vec{r}_2, \dots, \vec{r}_N) = \sum_{i=1}^N \psi_1(\vec{r}_i) \sum_{i=1}^N \psi_2(\vec{r}_i) \quad (5.54)$$

Then, we have

$$E(\psi_1, \psi_1^*, \psi_2, \psi_2^*) = \int dr^3 \begin{pmatrix} \psi_1^* & \psi_2^* \end{pmatrix} \cdot \begin{pmatrix} \mathcal{H}_{11} & \mathcal{H}_{12} \\ \mathcal{H}_{21} & \mathcal{H}_{22} \end{pmatrix} \cdot \begin{pmatrix} \psi_1 \\ \psi_2 \end{pmatrix} + E_{\text{LHY}} \quad (5.55)$$

where \mathcal{H}_{ij} represent the Hamiltonian density of fields

$$\begin{aligned}\mathcal{H}_{11} &= N_1 \left(\frac{\hbar^2}{2m_1} (\nabla)^2 + V_1(r) + \frac{1}{2} N_1 g_{11} (\psi_1^*(r) \psi_1(r)) \right) \\ \mathcal{H}_{22} &= N_2 \left(\frac{\hbar^2}{2m_2} (\nabla)^2 + V_2(r) + \frac{1}{2} N_2 g_{22} (\psi_2^*(r) \psi_2(r))^2 \right) \\ \mathcal{H}_{12} &= \mathcal{H}_{21}^\dagger = N_1 N_2 g_{12} (\psi_1^*(r) \psi_1(r)) (\psi_2^*(r) \psi_2(r))\end{aligned}\quad (5.56)$$

and LHY term has been expressed in the last part. define the Variation

$$X(\psi, \psi^*) = E(\psi, \psi^*) - \mu_1 N_1 \int dr^3 (\psi_1^*(r) \psi_1(r)) - \mu_2 N_2 \int dr^3 (\psi_2^*(r) \psi_2(r))\quad (5.57)$$

Finally, we have eGPE for

$$\begin{aligned}i\hbar \frac{\partial \psi_1}{\partial t} &= \left(-\frac{\hbar^2 \nabla^2}{2m_1} + V_1 + g_{11} n_1 + g_{12} n_2 + \frac{\delta \mathcal{E}_{\text{LHY}}}{\delta n_1} \right) \psi_1 \\ i\hbar \frac{\partial \psi_2}{\partial t} &= \left(-\frac{\hbar^2 \nabla^2}{2m_2} + V_2 + g_{22} n_2 + g_{12} n_1 + \frac{\delta \mathcal{E}_{\text{LHY}}}{\delta n_2} \right) \psi_2\end{aligned}\quad (5.58)$$

5.3.3 eGPE for GPELAB with Minardi approximation

$$\begin{aligned}i\hbar \frac{\partial \psi_1}{\partial t} &= \left(-\frac{\hbar^2 \nabla^2}{2m_1} + V_1 + g_{11} n_1 + g_{12} n_2 + \frac{\delta \mathcal{E}_{\text{LHY}}}{\delta n_1} \right) \psi_1 \\ i\hbar \frac{\partial \psi_2}{\partial t} &= \left(-\frac{\hbar^2 \nabla^2}{2m_2} + V_2 + g_{22} n_2 + g_{12} n_1 + \frac{\delta \mathcal{E}_{\text{LHY}}}{\delta n_2} \right) \psi_2\end{aligned}\quad (5.59)$$

where $n_i = N_i \psi_i^* \psi_i = N_i |\psi_i|^2$ and

$$\frac{\delta \mathcal{E}_{\text{LHY}}}{\delta n_1} = \frac{8}{15\pi^2} \frac{m_1^{3/2} (g_{11})^{5/2} n_1^{1/2}}{\hbar^3} \left(\frac{5}{2} n_1 f(\gamma, x, y) - \frac{g_{22} n_2}{g_{11}} \frac{\partial f(\gamma, x, y)}{\partial y} \right)\quad (5.60)$$

$$\frac{\delta \mathcal{E}_{\text{LHY}}}{\delta n_2} = \frac{8}{15\pi^2} \frac{m_1^{3/2} (g_{11})^{3/2} g_{22} n_1^{3/2}}{\hbar^3} \frac{\partial f(\gamma, x, y)}{\partial y}\quad (5.61)$$

if we using the approximation formula, we have

$$\mathcal{E}_{\text{LHY}} = \frac{8}{15\pi^2} \frac{m_1^{3/2} (g_{11} n_1)^{5/2}}{\hbar^3} (1 + \gamma^{3/5} y)^{5/2}\quad (5.62)$$

Then,

$$\begin{aligned}\frac{\delta \mathcal{E}_{\text{LHY}}}{\delta n_1} &= \frac{8}{15\pi^2} \frac{m_1^{3/2} (g_{11})^{5/2} n_1^{1/2}}{\hbar^3} \left(\frac{5}{2} n_1 (1 + \gamma^{3/5} y)^{5/2} - \frac{5}{2} \frac{g_{22} n_2}{g_{11}} (1 + \gamma^{3/5} y)^{3/2} \gamma^{3/5} \right) \\ &= \frac{4}{3\pi^2} \frac{m_1^{3/2} (g_{11})^{5/2} n_1^{3/2}}{\hbar^3} (1 + \gamma^{3/5} y)^{3/2}\end{aligned}\quad (5.63)$$

$$\begin{aligned}\frac{\delta \mathcal{E}_{\text{LHY}}}{\delta n_2} &= \frac{8}{15\pi^2} \frac{m_1^{3/2} (g_{11})^{3/2} g_{22} n_1^{3/2}}{\hbar^3} \frac{5}{2} (1 + \gamma^{3/5} y)^{3/2} \gamma^{3/5} \\ &= \frac{4}{3\pi^2} \frac{\gamma^{3/5} m_1^{3/2} (g_{11})^{3/2} g_{22} n_1^{3/2}}{\hbar^3} (1 + \gamma^{3/5} y)^{3/2}\end{aligned}\quad (5.64)$$

Finally, we have extended GPE as

$$\begin{aligned}i\hbar \frac{\partial \psi_1}{\partial t} &= \left(-\frac{\hbar^2 \nabla^2}{2m_1} + V_1 + g_{11} n_1 + g_{12} n_2 + \frac{4}{3\pi^2} \frac{g_{11} m_1^{3/5}}{\hbar^3} \left(g_{11} n_1 m_1^{3/5} + g_{22} n_2 m_2^{3/5} \right)^{3/2} \right) \psi_1 \\ i\hbar \frac{\partial \psi_2}{\partial t} &= \left(-\frac{\hbar^2 \nabla^2}{2m_2} + V_2 + g_{22} n_2 + g_{12} n_1 + \frac{4}{3\pi^2} \frac{g_{22} m_2^{3/5}}{\hbar^3} \left(g_{11} n_1 m_1^{3/5} + g_{22} n_2 m_2^{3/5} \right)^{3/2} \right) \psi_2\end{aligned}\quad (5.65)$$

Now, we need do Dimension-Reduction,

$$\begin{aligned}i \frac{\partial \Psi_1}{\partial T} &= \left[-\frac{m \nabla^2}{2m_1} + \frac{V_1}{\hbar \omega} + 4\pi \frac{m}{m_1} \frac{N_1 a_{11}}{a} \Psi_1^* \Psi_1 + 2\pi \frac{m}{m_{12}} \frac{N_2 a_{12}}{a} \Psi_2^* \Psi_2 \right. \\ &\quad + \frac{128\pi^{1/2}}{3} \frac{a_{11}}{a} \left(\frac{m}{m_1} \right)^{2/5} \left(\frac{N_1 a_{11}}{a} \left(\frac{m}{m_1} \right)^{2/5} \Psi_1^* \Psi_1 \right. \\ &\quad \left. \left. + \frac{N_2 a_{22}}{a} \left(\frac{m}{m_2} \right)^{2/5} \Psi_2^* \Psi_2 \right)^{3/2} \right] \Psi_1 \\ i \frac{\partial \Psi_2}{\partial T} &= \left[-\frac{m \nabla^2}{2m_2} + \frac{V_2}{\hbar \omega} + 4\pi \frac{m}{m_2} \frac{N_2 a_{22}}{a} \Psi_2^* \Psi_2 + 2\pi \frac{m}{m_{12}} \frac{N_1 a_{12}}{a} \Psi_1^* \Psi_1 \right. \\ &\quad + \frac{128\pi^{1/2}}{3} \frac{a_{22}}{a} \left(\frac{m}{m_2} \right)^{2/5} \left(\frac{N_1 a_{11}}{a} \left(\frac{m}{m_1} \right)^{2/5} \Psi_1^* \Psi_1 \right. \\ &\quad \left. \left. + \frac{N_2 a_{22}}{a} \left(\frac{m}{m_2} \right)^{2/5} \Psi_2^* \Psi_2 \right)^{3/2} \right] \Psi_2\end{aligned}\quad (5.66)$$

where we set V_1 and V_2 as harmonic trap, and it gives the characteristic length and

time. Actually, this characteristic length and time can be arbitrary.

$$\begin{aligned} g_{11} &= \frac{4\pi\hbar^2 a_{11}}{m_1}, g_{22} = \frac{4\pi\hbar^2 a_{22}}{m_2}, g_{12} = \frac{2\pi\hbar^2 a_{12}}{m_{12}}, m_{12} = \frac{m_1 m_2}{m_1 + m_2} \\ T &= \omega t, \vec{R} = \vec{r}/a, \Psi = \psi a^{3/2}, a = \sqrt{\frac{\hbar}{m\omega}} \end{aligned} \quad (5.67)$$

By the way, we can calculate the Nonlinear-Energy function. (Just for fun, not for GPELAB) Recall LHY energy term

$$\begin{aligned} \mathcal{E}_{\text{LHY}} &= \frac{8}{15\pi^2} \frac{m_1^{3/2} (g_{11} n_1)^{5/2}}{\hbar^3} \left(1 + \left(\frac{m_2}{m_1} \right)^{3/5} \frac{g_{22} n_2}{g_{11} n_1} \right)^{5/2} \\ &= \frac{256\sqrt{\pi}\hbar^2}{15} \left(m_1^{-2/5} a_{11} n_1 + m_2^{-2/5} a_{22} n_2 \right)^{5/2} \end{aligned} \quad (5.68)$$

Do Dimension-Reduction, we have

$$\frac{\mathcal{E}_{\text{LHY}}}{\hbar\omega/a^3} = \frac{256\pi^{1/2}}{15} \left(\frac{N_1 a_{11}}{a} \left(\frac{m}{m_1} \right)^{2/5} \Psi_1^* \Psi_1 + \frac{N_2 a_{22}}{a} \left(\frac{m}{m_2} \right)^{2/5} \Psi_2^* \Psi_2 \right)^{5/2} \quad (5.69)$$

5.4 Na-Rb Hetero-nuclear quantum droplet

This section¹ demonstrates our experiment study on the quantum droplet made of Na-Rb BEC mixture. Our experiment starts from an optically trapped double BEC of ²³Na and ⁸⁷Rb (denoted as species 1 and 2 hereafter, respectively) both prepared in their lowest-energy hyperfine Zeeman level $|F = 1, m_F = 1\rangle$ [Wang et al., 2015b]. To reveal the LHY effects, we focus on the near-zero MF region with $\delta g = g_{12} + \sqrt{g_{11}g_{22}} \approx 0$. Here $g_{ij} = 2\pi\hbar^2 a_{ij}/M_{ij}$ are the two-body interaction constants, with a_{ij} the scattering lengths and M_{ij} the reduced masses. To reach this regime, we use the Na-Rb Feshbach resonance at $B_0 = 347.648$ G to tune the Na-Rb scattering length. The scattering length is represented as $a_{12} = a_{\text{bg}}(1 - \Delta/(B - B_0))$ [upper panel of Fig. 5.4(a)], with background scattering length $a_{\text{bg}} = 76.33a_0$ and resonance width $\Delta = 4.255$ G [Wang et al., 2013]. Near B_0 the intraspecies scattering lengths $a_{11} =$

¹This section is mainly from our paper [Guo et al., 2021a].

$60.05a_0$ [Knoop et al., 2011] and $a_{22} = 100.13a_0$ [van Kempen et al., 2002] remain almost constant.

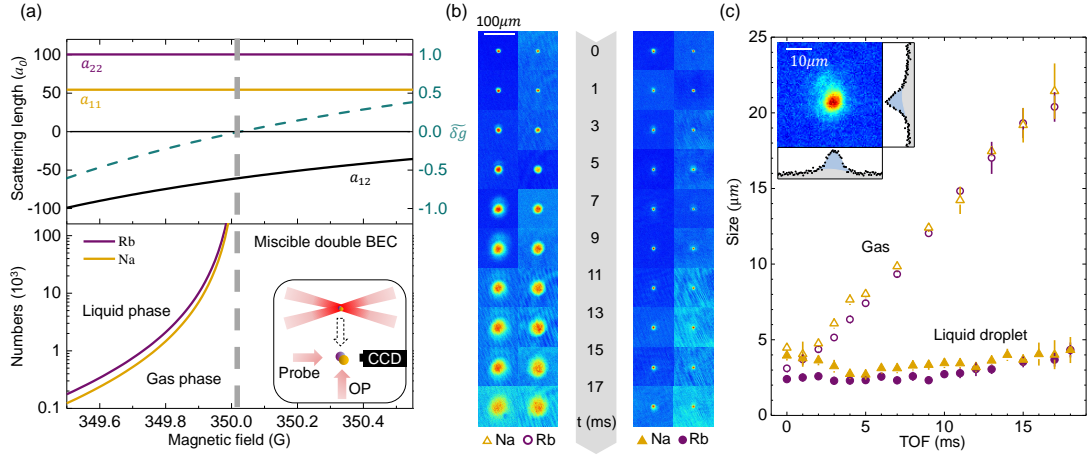


Figure 5.4: Creation and detection of Na-Rb mixtures for investigating LHY effects. (a) In the upper panel, the purple, yellow, and black solid lines are scattering lengths between Na-Na(a_{11}), Rb-Rb(a_{22}) and Na-Rb(a_{12}), respectively. The dashed green curve is $\tilde{\delta}g$. The dashed vertical line indicates the magnetic field for $\tilde{\delta}g = 0$. In the lower panel, the phase diagrams at different atomic numbers and magnetic fields are shown. Inset: schematic detection method of the droplet in free space. (b) Images of the mixture during the TOF expansion in the gas phase at 350.451 G (left) and the droplet phase at 349.849 G (right). (c) Cloud sizes obtained from (b) reveal the very different behaviors of the two phases. Data points for ⁸⁷Rb are shown in purple, while those for ²³Na are in yellow. Inset: in the droplet phase, bimodal distributions are observed for the cloud with excess atoms. A double Gaussian fitting is used to extract the droplet size in this case.

For convenience, we define a dimensionless parameter $\tilde{\delta}g \equiv \delta g / \bar{g}$ to characterize the total E_{MF} , with $\bar{g} = (g_{11} + g_{22})/2$. For the current system, the critical magnetic field for $\tilde{\delta}g = 0$ (and also $\delta g = 0$) is $B_c = 349.978$ G, which corresponds to a critical interspecies scattering length $a_{12}^c = -63.1a_0$. As shown in Fig. 5.4(a) (lower panel), for each value of $\tilde{\delta}g < 0$, the double BEC will undergo a transition from gas phase to droplet phase as the atom numbers are increased. With our atom numbers around 10^4 for both species, the theory predicts an observation window for the droplet phase for

$\tilde{\delta}g$ from -0.061 to -0.189 (349.910 G to 349.780 G). For $\tilde{\delta}g$ from 0 to -0.061 , droplet formation is still possible but atom numbers much larger than currently available are needed.

5.4.1 Experiment method and time sequence

In the first experiment, we study the Na-Rb quantum droplet in free space by releasing the sample from the optical trap. We probe the system during the time of flight (TOF), as depicted in the inset of Fig. 5.4(a). To probe the atoms *in situ* at each TOF, we implement a two-species high-field detection protocol which consists of a partial optical pumping process followed by standard absorption imaging on the cycling transitions [Jia et al., 2020]. This partial imaging method is necessary as the droplets have very high optical depth and are difficult to detect directly [Ramanathan et al., 2012; Semeghini et al., 2018]. Both the partial optical pumping and the absorption imaging are calibrated using standard methods [Reinaudi et al., 2007; Hueck et al., 2017]. The measured resolutions ($1/\sqrt{e}$ half Gaussian widths) of our imaging system are $0.6\ \mu\text{m}$ and $0.8\ \mu\text{m}$ for ^{23}Na at 589 nm and ^{87}Rb at 780 nm, respectively, which are just enough to resolve the droplet. To maintain the imaging resolutions, we mount the objective and the probe light optics on high-precision vertical translational stages to keep the optical axis of the imaging system always aligned with the droplet.

Figure 5.5 shows the time sequence we produce quantum droplet. While shutting down the optical trap provides a direct way of probing the droplet in free space, the non-adiabatic nature of the process can cause problems. Due to the confinement, the in-trap sample is smaller in size than the free-space droplet in its ground state, while the total energy of the system is much larger. In the worst scenario, the energy of the initial state upon release from the trap is larger than the energy barrier of the expansion and a stable droplet can never be formed. To mitigate this problem, the crossed optical dipole trap is configured in a nearly spherical shape with measured

trap oscillation frequencies of 78 Hz (86 Hz) for ^{87}Rb (^{23}Na). This is in accordance with the understanding that a quantum droplet with isotropic short-range interactions should be spherical in free space. In addition, a carefully designed magnetic field control sequence is used to improve the mode matching. These steps allow us to observe droplet formation reliably for $\tilde{\delta}g$ from -0.094 to -0.189 . However, for $\tilde{\delta}g$ from -0.061 to -0.094 , due to the smaller binding energy, droplets can be observed only by a more sophisticated mode-matching method, aided by fast magnetic field quenching at the instant of releasing the samples from the trap. For this method to work, the starting magnetic field must be selected carefully so that the size of the in-trap sample matches that of the free-space droplet at the end of the magnetic field quenching.

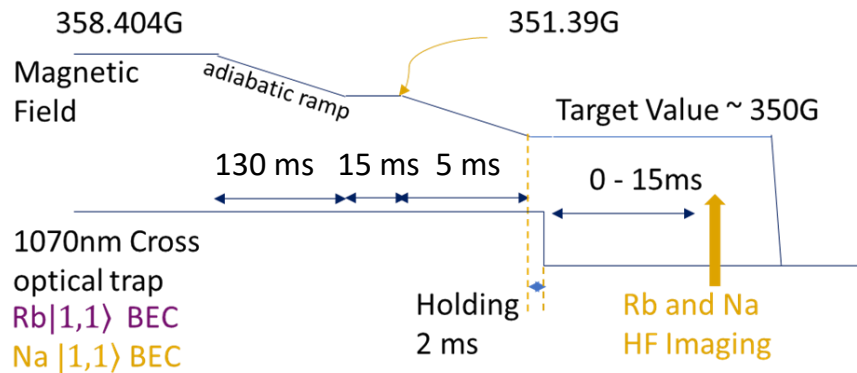


Figure 5.5: Time sequence for producing quantum droplet.

5.4.2 observing non-expansion signal

Figure 5.4(b) shows a side-by-side comparison of the ^{23}Na and ^{87}Rb clouds in the gas phase and the droplet phase following the TOF. The signature self-bound behavior of the droplet can be observed clearly by comparing its dramatically different TOF expansion with that in the gas phase. For $\tilde{\delta}g = -0.119$ (349.849 G), where the droplet

phase is expected, the sizes of both clouds stay nearly the same during the TOF. For $\tilde{\delta}g = +0.344$ (350.451 G), by contrast, the system remains in the gas phase, and the sizes increase steadily with TOF.

To extract quantitative information, we fit the images with 2D Gaussian functions. In the droplet, the size should be the same for the two species; their densities and thus numbers should follow the ratio $N_2/N_1 = \sqrt{g_{11}/g_{22}} = 1.51$ [Petrov, 2015]. When this ratio is not maintained, the droplet part shows up as a dense central peak, and the excess atoms of one species appear as a much larger-sized and expanding gaseous background surrounding the droplet [inset of Fig. 5.4(c)]. For this kind of “bimodal” distribution, the droplet parameters are extracted with a double 2D Gaussian fitting. Fig. 5.4(c) shows the starkly different expansion behaviors in the droplet and the gas phases obtained from the images in Fig. 5.4(b).

For the droplets formed by direct trap release from $\tilde{\delta}g = -0.094$ to -0.189 , we observe two distinctively different dynamics in the evolution of the ^{23}Na and ^{87}Rb samples during the TOF. As an example, Fig. 5.6(a), (b) and (c) show the sizes, atom numbers, and number ratio of the droplet sample for $\tilde{\delta}g = -0.116$ (349.852 G). During the first 10 ms, the ^{23}Na and ^{87}Rb sizes increase very little, while atom losses are observed for both species. Bimodal distributions are observed from 0 ms to 5 ms as the initial number ratio is far from 1.51. After 5 ms expansion, the gaseous atoms surrounding the droplet are already too dilute to be detected.

After about 10 ms, the sample sizes start to increase while the atom numbers stay nearly constant. This is consistent with a phase transition from droplet to gas when the atom numbers are reduced to below the critical values [see Fig. 5.4(a)]. We fit the size evolution empirically with $\sigma(t > t_0) = \sqrt{\sigma_0^2 + v^2(t - t_0)^2}$ and $\sigma(t < t_0) = \sigma_0$, and obtain a lifetime in the droplet phase of about $t_0 = 7$ ms. Here v is the expansion velocity of the gas-phase sample. Similarly, as illustrated in Fig. 5.6(b), the critical atom numbers for the phase transition can be obtained by fitting the ^{23}Na and ^{87}Rb

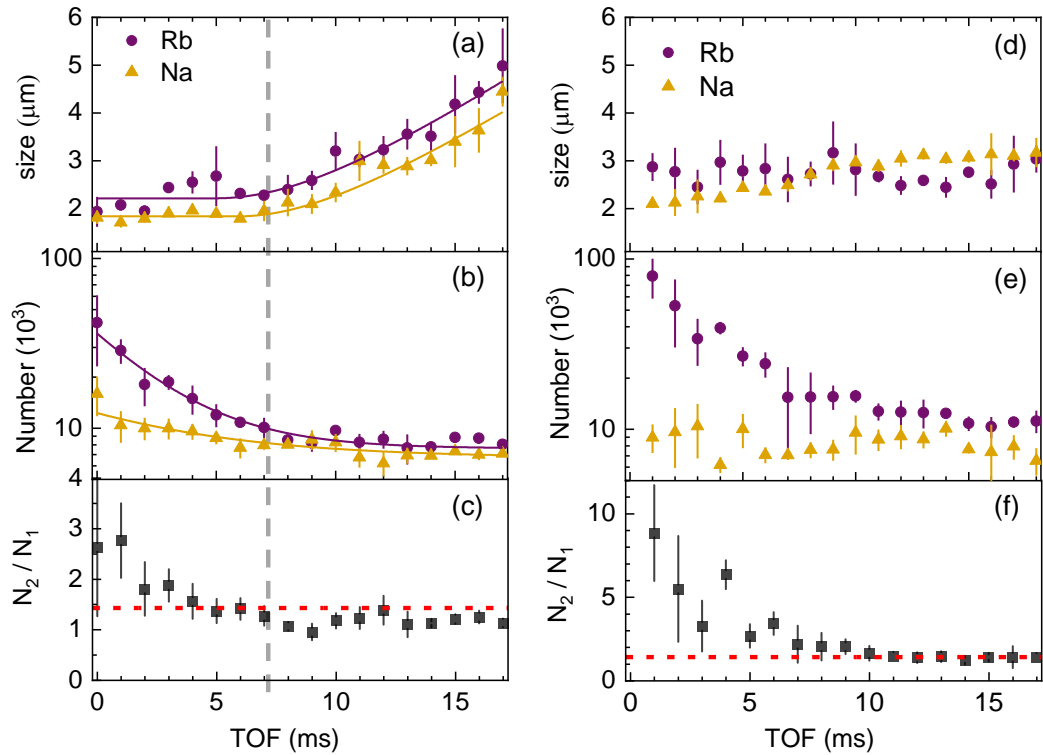


Figure 5.6: Evolution of the Na-Rb droplet in free space. (a), (b), and (c) show the size, atom numbers, and the ^{87}Rb to ^{23}Na number ratio at $\tilde{\delta}g = -0.116$ (349.852 G) following the TOF. The droplet is created by directly releasing the sample from the trap. The vertical bar marks the approximate time of the liquid-to-gas phase transition. (d), (e), and (f) show the evolution for the droplet created with the additional magnetic field quenching for $\tilde{\delta}g = -0.089$ (349.880 G). The red dashed lines in (c) and (f) mark the theoretical number ratio $N_2/N_1 = 1.51$.

number evolution data with an exponential decay function with the critical number as the offset.

For several values of $\tilde{\delta}g$ between -0.061 and -0.094 , we have created longer-lived droplets by the magnetic field quenching method. As shown in Fig. 5.6(d), (e) and (f), during the accessible TOF, the droplet size stays nearly the same although number losses are still observed. After 10 ms, the number ratio becomes close to 1.51 and the number loss slows down significantly. As the lifetime is longer than the usable TOF

of 18 ms, we have not been able to measure the real lifetime and the critical numbers in this range of $\tilde{\delta}g$. More detailed investigations, e.g., by levitating the droplet, are warranted in the near future.

5.4.3 Characterization of liquid-gas phase transition

Figure 5.7 shows the critical ^{23}Na and ^{87}Rb atom numbers for $\tilde{\delta}g$ from -0.146 to -0.247 . Although the range of $\tilde{\delta}g$ is small, a four-fold change in the measured critical numbers is observed. The critical numbers calculated using coupled eGPEs with the LHY term included (dashed curves) show large discrepancies with the measurements. The agreement is greatly improved by also including the small post-compensation residual magnetic field gradient in the eGPEs (solid curves); the additional term nearly doubles the critical numbers. This can be understood from the different magnetic dipole moments and masses of ^{23}Na and ^{87}Rb , which cause their centers of mass to separate in a magnetic field gradient. This decreases the density overlap and lowers the attractive interspecies mean-field energy while leaving the intraspecies energy nearly intact. Effectively, this increases the critical numbers compared to the ideal case of zero gradient.

A major cause of the atom losses is three-body recombination as a result of the high number densities in the droplet [Cabrera et al., 2018; Semeghini et al., 2018; D’Errico et al., 2019]. For droplets with $\tilde{\delta}g$ from -0.094 to -0.189 , another possible loss mechanism is self-evaporation due to the imperfect matching between in-trap and free-space modes [Ferioli et al., 2020]. The short lifetimes in this region are the combined result of these loss mechanisms. In contrast, the droplet at $\tilde{\delta}g = -0.089$ [see Fig. 5.6(d), (e), and (f)] has relatively lower number densities and is formed with nearly optimal mode matching, and is thus longer lived. Nevertheless, for both cases, the stabilized number ratios after 10 ms TOF are very close to 1.51 despite the different creation procedures and the large initial number mismatches [Fig. 5.6(c) and (f)].

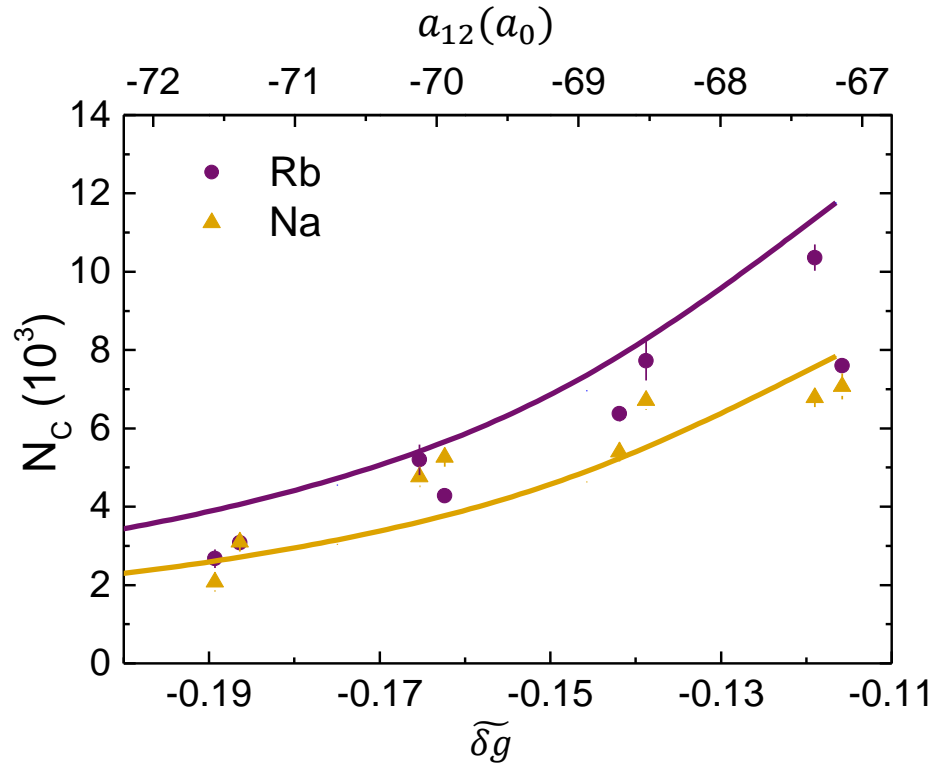


Figure 5.7: Critical atom numbers for the liquid-to-gas phase transition as a function of $\tilde{\delta}g$. The solid lines are calculated from coupled eGPEs with the residual magnetic field gradient included.

5.5 Lee-Huang-Yang gas

We now turn to the gas-phase double BEC and release the sample directly from the trap (without the additional magnetic field quenching) for $\tilde{\delta}g$ from $+0.344$ to -0.094 . To characterize the LHY effect, we measure the release energy $E_{\text{rel}} = E_{\text{kin}} + E_{\text{int}}$ from the TOF expansion [Holland et al., 1997; Mewes et al., 1996]. Here E_{kin} is the quantum pressure and $E_{\text{int}} = E_{\text{MF}} + E_{\text{LHY}}$ is the total interaction energy. When E_{MF} is tuned to zero, E_{LHY} becomes the only interaction term in E_{rel} . For negative E_{MF} , the fact that the sample expands rather than collapses is also a direct manifestation of the LHY effect.

When we using TOF measurement on condensate from a harmonic trap, we lose the trap energy suddenly and the kinetic energy (quantum pressure) and the interaction energy converts to kinetic energy of motion after long-time evolution. So, we have the release energy

$$E_{\text{release}} = E_{\text{kin}} + E_{\text{MF}} = N\hbar\omega_0 \left(\frac{3}{4} \frac{1}{w^2} + \frac{1}{\sqrt{2\pi}} \frac{a_s N}{a_{\text{ho}}} \frac{1}{w^3} \right) \quad (5.70)$$

put the numerical solution of w into the release energy, we have for $g = 0$ case, we have $E_{\text{release}} = \frac{3}{4}\hbar\omega_0$. With increasing χ , we have larger size (larger w), and finally, when reach $\chi \gg 1$ limit, we turn to the Thomas-Fermi limit.

5.5.1 Expansion of gas phase sample and Release energy

In the previous sections, we describe a liquid phase droplet sample made of ^{23}Na - ^{87}Rb BEC mixture. Now we turn to study the gas phase (LHY gas) of this mixture, in which the Lee-Huang-Yang effects still play an important role. The mainly difference between a droplet and a LHY gas sample is whether the kinetic energy dominates the Hamiltonian. For droplet sample, the competition mainly comes from the attractive mean-field term and the repulsive LHY term. When the atomic number drops down, and both mean-field and LHY energy goes down, finally the kinetic energy gets not negligible. After the balance point of density disappeared, as we describe about the liquid-gas phase transition, the sample turns to a gas-phase sample.

by directly releasing the sample from the trap for \tilde{g} from +0.322 to -0.146. To characterize the LHY effect in this situation, we measure the release energy $E_{\text{rel}} = E_{\text{kin}} + E_{\text{int}}$ from the TOF expansion [Holland et al., 1997; Mewes et al., 1996]. Here E_{kin} is the quantum pressure and $E_{\text{int}} = E_{\text{MF}} + E_{\text{LHY}}$ is the total interaction energy. When E_{MF} is tuned to zero, E_{LHY} becomes the only interaction term in E_{rel} . For negative E_{MF} , the expansion of the sample, instead of collapsing, is also a direct manifestation of the LHY effect.

We prepared the trapped double BEC and measured E_{rel} for both species from their TOF expansion velocities [Holland et al., 1997] for several different $\tilde{\delta}g$. The resulting total E_{rel} is shown as open squares in Fig. 5.8. In general, E_{rel} depends on $\tilde{\delta}g$, N_1 and N_2 , and the density overlap between the two species. However, within the range of $\tilde{\delta}g$, the densities of the double BEC are still rather high even in the gas phase, and significant three-body losses are still observed during the TOF. Thus, it is difficult to maintain constant N_1 and N_2 during the TOF for different $\tilde{\delta}g$, even though great efforts have been taken to keep the initial atom numbers in the trap fixed. However, since E_{rel} is a measure of the energy per atom, it is not affected severely by the loss.

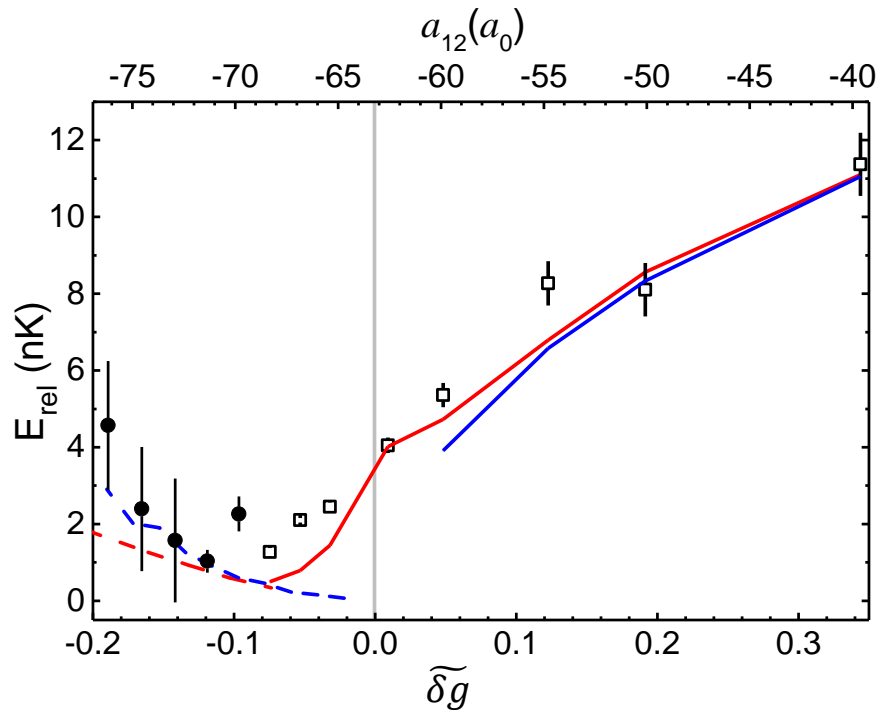


Figure 5.8: Measurement of the release energy as a function of $\tilde{\delta}g$. The open squares represent E_{rel} of the gas phase mixtures released from the trap directly, while the solid circles are E_{rel} of the gas samples formed following the liquid-gas phase transition. The red solid (blue solid) curve is the calculated E_{rel} with (without) the LHY terms for the first case with GPEs and the red dashed curve is E_{rel} for the second case from variational theory.

We calculated the E_{rel} with the eGPEs for the corresponding atom numbers at the end of the TOF and found a good match for both the $E_{\text{MF}} \gg E_{\text{LHY}}$ and the $E_{\text{MF}} \approx 0$ regions (red solid curve in Fig. 5.8). We note that without the LHY term, the calculation fails for $\tilde{\delta}g < 0$ due to the collapse (blue solid curve in Fig. 5.8). At the $\tilde{\delta}g \approx 0$ point with E_{MF} almost canceled, the energy difference between the two calculations is about 1 nK. This is essentially the magnitude of E_{LHY} , if we assume E_{kin} does not change dramatically in these two cases.

The gas phase mixture formed following the liquid-to-gas phase transition is also of great interest. As shown in Fig. 5.6(a), its expansion velocity can be measured and converted into another E_{rel} even though there is no trap involved. These results are shown in Fig. 5.8 as solid circles for $\tilde{\delta}g$ from -0.146 to -0.247. Compared with the gas phase mixture released from the trap, the E_{rel} here has a completely opposite dependence on $\tilde{\delta}g$.

This behavior can be qualitatively understood from the change of the total energy of the droplet (E_{tot}) during the phase transition. For large enough atom numbers, E_{tot} has a negative minimum, and the system is in the droplet phase. Following the number loss, E_{tot} increases gradually. The droplet becomes meta-stable when E_{tot} is above zero, and the system eventually enters the gas phase when the energy minimum disappears. The measured E_{rel} here reflects E_{tot} at the phase transition point which also includes contributions from E_{LHY} , E_{MF} , and E_{kin} .

For more negative $\tilde{\delta}g$, the critical atom numbers at the phase transition point are smaller, but the sample size $\propto |\tilde{\delta}g|^{-3/2}$ shrinks much steeper. As result, the increase of the positive E_{LHY} and E_{kin} terms are faster than the decrease of the negative E_{MF} term. E_{tot} is thus positive and the measured E_{rel} also follows the same trend and increases for more negative $\tilde{\delta}g$. We note that without E_{LHY} , the magnitude of E_{MF} is larger than E_{kin} and the system will collapse. This picture is confirmed by the variational calculation as depicted by the red dashed curve in Fig. 5.8.

5.6 Mode matching when producing droplet sample

5.6.1 In-trap vs. free-space sample

During the release of the double BEC sample from the optical trap, the trap energy suddenly is removed suddenly but the size of the sample has no time to adapt to the new value. As shown in Fig. 5.9, in general the in-trap size is smaller than the size of the ground-state free-space droplet at the energy minimum. The sample size will thus start to expand after released from the trap and its total energy (per particle) $E_{\text{tot}} = E_{\text{kin}} + E_{\text{int}}$ will also start to evolve following the red curves. For the cases with very small $|\tilde{\delta}g|$ [Fig. 5.9(a)], E_{tot} is higher than the energy barrier at the right hand side. In this case, the sample will just keep expanding after crossing the maximum point and never forms the droplet. While in Fig. 5.9(b), with $|\tilde{\delta}g|$ large enough, the negative E_{tot} of the released sample is not enough to overcome the energy barrier and the droplet can be formed, but its size will undergo a small-amplitude oscillation.

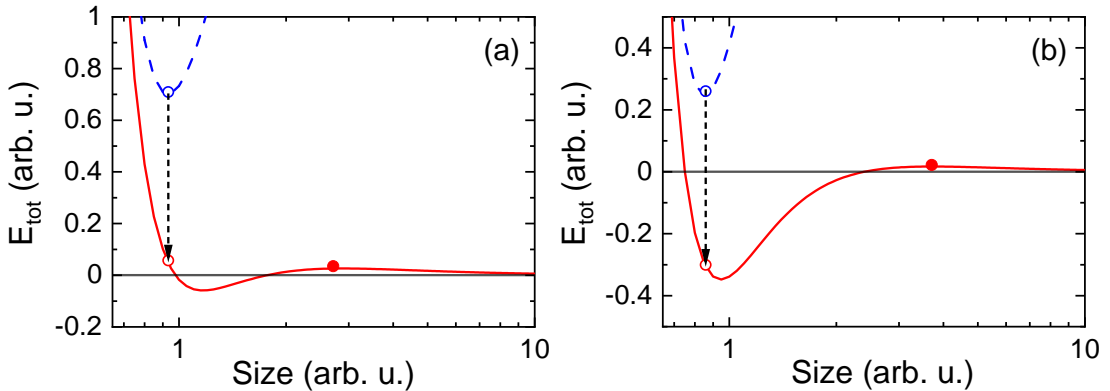


Figure 5.9: Droplet formation by directly releasing the trapped sample. The blue dashed curves represent $E_{\text{tot}} = E_{\text{kin}} + E_{\text{pot}} + E_{\text{int}}$ of the trapped double BEC, and the red solid curves are E_{tot} in free space (i.e., $E_{\text{kin}} + E_{\text{int}}$). (a) For very small $|\tilde{\delta}g|$, the free-space E_{tot} (the red open circle) is higher than the barrier height on the large size side (the red solid dot). In this case, the sample will keep expanding and never forms the droplet. (b) For $|\tilde{\delta}g|$ large enough, the sample does not have enough energy and will be confined near the energy minimum to form the droplet.

5.6.2 producing weak bound droplet by quenching B-field

To improve the mode matching, we used a nearly spherical shape trap for matching the sphere shape of the quantum droplet. In addition, as the in-trap size of the double BEC also depends strongly on $\tilde{\delta}g$, the magnetic field is controlled in a carefully designed sequence. After the double BEC is created, the magnetic field is first ramped up quickly across the Feshbach resonance to 358.4 G where a_{12} has a small positive value of $46.1a_0$. After 350 ms for the system to stabilize, the magnetic field is ramped down to 350.451 G in 130 ms. This is just 0.424 G above B_c and the corresponding a_{12} is $-39.5a_0$ ($\tilde{\delta}g = +0.322$). Here the double BEC is miscible and the attractive interaction increases the spatial overlap of the two condensates and also increases the in-trap densities substantially. Both effects significantly improve the mode matching and facilitate the free-space droplet formation. At this point, rapid atom losses are already observed; thus, the magnetic field holds here for only 10 ms. Afterwards, the magnetic field is ramped to a target value within 5 ms before the droplet is detected in free space. As depicted in Fig. 5.9(b), although droplet can be observed after these improvements for $|\tilde{\delta}g|$ large enough, the mode matching is not perfect. For $\tilde{\delta}g$ from 0 to -0.146, with the current atom numbers, the droplet cannot be observed by simply releasing the double BEC from the trap. As shown in Fig. 5.10(a), even better mode matching can be achieved by finding a $\tilde{\delta}g$ value where the in-trap size matches with the target droplet size and quenches $\tilde{\delta}g$ at the same time when the trap is shut off. To achieve the fast magnetic field quenching necessary for this method, we added a small magnetic coil which is capable of covering the magnetic field range in less than 10 μ s. Fig. 5.10(b) and (c) show two droplets formed with this method. For case (b) with $\tilde{\delta}g = -0.141$, the droplet lifetime is longer than the available observation time. For case (c) with $\tilde{\delta}g = -0.110$, the liquid-to-gas phase transition is observed after about 7 ms. This short lifetime is probably limited by the atom numbers since at this $\tilde{\delta}g$, the critical atom numbers are much larger.

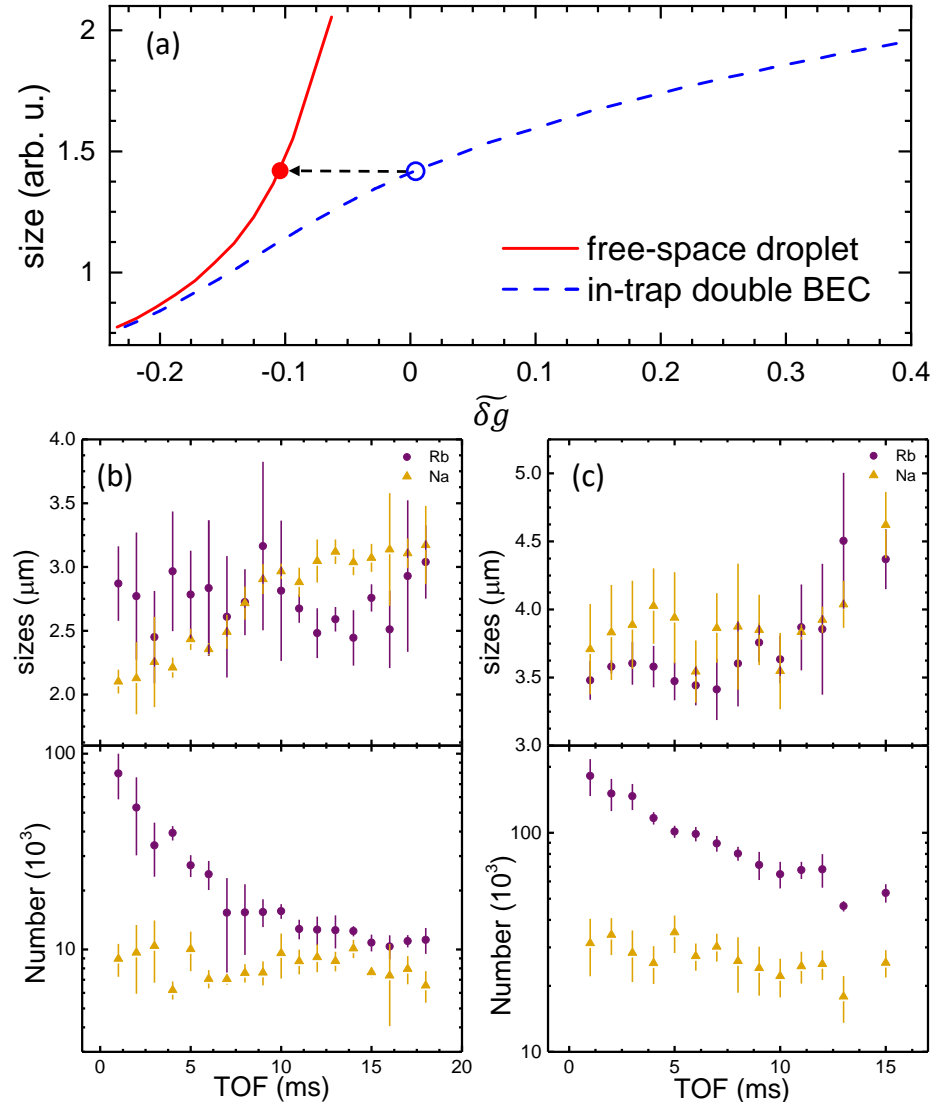


Figure 5.10: Producing long-lived droplet by magnetic field quench. (a) For some weakly bound droplet, it is possible to find a $\delta\tilde{g}$ value where the in-trap gas-phase sample size (blue dashed curve) is the same as the size of the free-space droplet (red solid curve). Quenching $\delta\tilde{g}$ at the instant of releasing the sample, as depicted by the black dashed arrow, will lead to a near perfect mode matching. (b) and (c) show the experimentally measured droplet signals for $\delta\tilde{g} = -0.141$ (349.880 G) and $\delta\tilde{g} = -0.110$ (349.910 G) created with this method. At these magnetic fields, no droplet can be observed without the quench as they fall in the situation as described in Fig. 5.9(a).

5.7 producing Feshbach molecule from droplet

Chapter 6

Conclusion and Outlooks

Historians may re-examine the mistakes of the past in the hope of providing warning for the future, but at the same time caution their readers to preserve what is of value. [Huang, 1981]

— Ray Huang
1587, a Year of No Significance (1981)

Section 6.1 summarize what we have done: 1. Detect the quantum droplet made of hetero-nuclear BEC mixture. 2. Characterize the LHY correction by studying the gaseous LHY gas sample. 3. Re-calibration of the 347.64 G Na-Rb Feshbach resonance due to requirement from droplet experiment. In Sec. 6.2, I review my research journey in these two years, trying to retrieve a storyline of our struggling instead of only the developed results and ending. Finally comes the outlooks (Sec. 6.3), where I try to describe the ongoing research direction in this field.

6.1 Conclusion

In this thesis, we build the hetero-nuclear quantum droplet made of Na and Rb BEC mixtures. We experimentally study the new phase of matter and investigate the LHY correction, which is vital for liquid droplet formation. With Na-Rb Feshbach resonance at 347.64 G, the interspecies interaction can be manipulated while remaining the intraspecies interaction. We observe the stabilization and formation of the quan-

tum droplet by detecting the smoking-gun self-binding behaviour, i.e. maintaining a finite volume even without any confinement. Our method is free-falling the mixture BEC sample and making an in-situ image at a high magnetic field, directly imaging the sample's density profile. Furthermore, we experimentally study the phase transition diagram of the quantum liquid droplet to a gaseous sample, which provides a quantitative characterization of the LHY effect.

To characterize the LHY correction further, we study the gaseous sample by measuring the expansion behaviour and thus its release energy. This release energy can reveal quantum pressure and interaction energy (including MF and LHY energy) in the original sample. By tuning the MF energy to zero, we can extract the information of LHY energy which provides another way to characterize this pure quantum effect. By carefully modelling the expansion process, we explain the abnormal expansion velocity of the gaseous sample near-zero mean-field energy region as a complementary study to the liquid phase.

Because of quantum droplets' sensitivity to the inter-particle interactions, we need an accurate map of the scattering length as a function of the magnetic field. Therefore, we measured the binding energy accurately by dissociating the Na-Rb Feshbach molecules. Then, fitting by the coupled-channel method, we obtained a highly accurate molecular potential curve. Finally, we achieved a refined map of the scattering length to the magnetic field. This calibration lay a solid foundation for further researches about the mixture of Na and Rb.

6.2 Thesis Overview

In this section, instead of demonstrating our research result of the heteronuclear droplet, I try to tell the story of how we were stuck in each step and how we solved problems. I summarize what we learnt from the research process, such as “be wary of every unverified number”. I hope this complementary material can serve as a lesson

for myself and the readers.

Our experiment of the droplet started in February of 2018. We first test the miscibility and immiscibility of a mixture BEC sample near the 347 G Feshbach resonance. Ref. [Wang et al., 2015b] tested this feature after time-of-flight (ToF) in a low magnetic field, which introduces deviation on the measurement of phase separation boundary. The ToF in a low magnetic field changes the scattering length between Na and Rb from the target value (such as $-50 a_0$) to the background one (i.e. $76 a_0$). This renders the mixture BEC immiscible, whatever its original miscibility in the high magnetic field, and causes a shift of the separation boundary. So, we tried to test the miscibility of the BEC mixture with different duration (Δ ms) between quenching the magnetic field down and releasing the optical trap (as shown in Fig. 6.1). By controlling this duration, we test the dynamics of the BEC mixture in the ToF process with different interspecies interactions. For example, we hold the magnetic field at 354.1 G, where the scattering length between Na and Rb is $26 a_0$. The sample is in a miscible phase. However, as shown in Fig. 6.1, with $\Delta < 4$ ms, an unmistakable immiscible signal shows up.

Then we try to approach the mean-field (MF) collapse region in the mixture BEC sample. With the above mentioned ToF method under a high magnetic field, the detection can reflect unaffected miscibility of the mixture sample. We use $\Delta = 10$ ms ToF inside the high magnetic field, which lowers down the density of the sample and releases its interaction energy. Then it is safe to switch off the magnetic field and take the image in a low field. The imaging timing for Na(Rb) is 13(18) ms after switching off the optical trap. By scanning the interspecies interaction, as shown in Fig. 6.2, we test the behaviour of the sample from $+12.45 a_0$ to $-63.75 a_0$. When gradually lower down the scattering length, the sample's size suddenly shrinks at about $-44 a_0$. Loss of atoms number also increases as the Optical depth of the sample get shallower. At that time, we only know about the collapse of the BEC, such as observed in Li [Donley

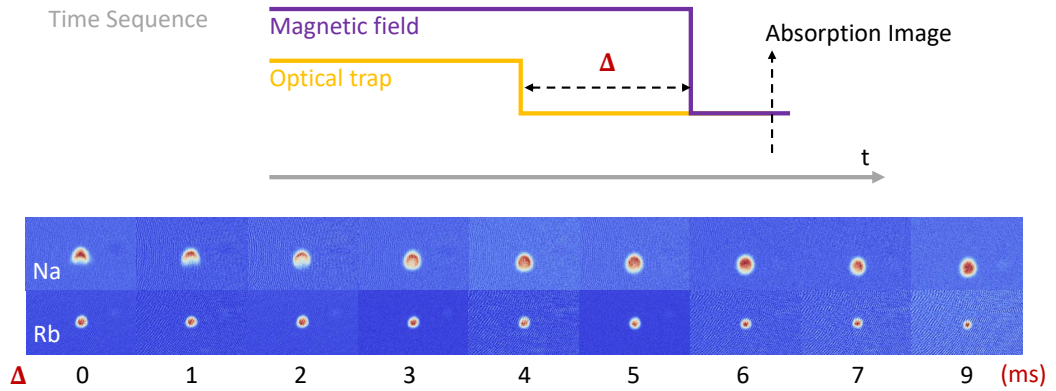


Figure 6.1: The upper panel shows the time sequence of testing the dynamic of a mixture BEC sample ToF under a high magnetic field. We first shut down the optical dipole trap, and the sample will free fall in the free space. Then, we hold the magnetic field for Δ ms, where the interspecies interaction is unchanged. Finally, to do a typical absorption image, we quench the magnetic field to several Gauss. We test different Δ , however, keep duration between image and the timing we turn off the optical trap. The bottom panel shows the absorption images of Na and Rb. The magnetic field is held at 354.1 G ($a_{\text{Na}-\text{Rb}} = 26a_0$) for different duration Δ ms. With a shorter duration, the immiscibility becomes more severe.

et al., 2001]. For the Na-Rb mixture, the MF collapse point is about -60 a₀. So, we thought that should be a collapse of the mixture sample. This collapse increases the density of the sample and causes a severe three-body loss.

Then, we notice Petrov's paper [Petrov, 2015], in which he described a stabilization mechanism that could avoid the MF collapse by the so-called LHY correction. Meanwhile, we found Leticia's paper [Cabrera et al., 2018] showing the experimental study of the ³⁹K droplet. This work encourages us to re-do the experiment mentioned above again and try to find the droplet signal. So, that is the start point of our experiment. Our goal is to build the first hetero-nuclear droplet made of a mixture Na-Rb BEC.

At the very beginning, we only have absorption image in the low magnetic field, which considerably limit our ability to detect the droplet signal. Because quantum

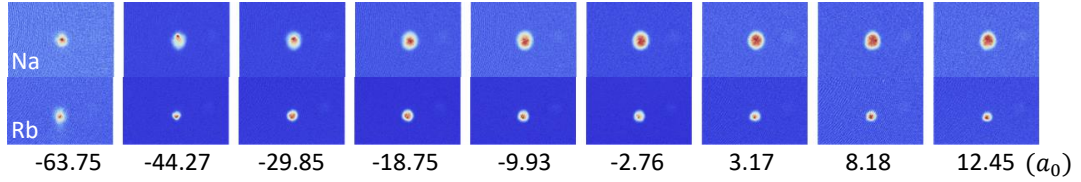


Figure 6.2: With method introduced in Fig. 6.1, we scan the interspecies interaction to probe the miscibility of mixture BEC sample. The ToF duration in free space for Na(Rb) is 13(18) ms. From right to left, with $a_{\text{Na}-\text{Rb}}$ gradually decreasing, the size of both Na and Rb shrinks. Moreover, a severe loss is detected for $a_{\text{Na}-\text{Rb}} = -63.8a_0$

droplet's size is relatively small, typically less than $2\text{-}3 \mu\text{m}$. With this limited image method, we have to detect the signal after a long ToF. As we already know, the dynamics during the ToF would severely affect the sample's shape and size. We thus choose to do the ToF under 350 G magnetic field for 5 ms first, then switch down the magnetic field. After 8(13) ms ToF in the low magnetic field, we do a Na(Rb) absorption image. As shown in Fig. 6.3, we measure the sample's size and number. When the magnetic field is higher than 352 G, i.e. around $a_{\text{Na}-\text{Rb}} = 0$, both Na and Rb show a constant size and number. When the magnetic field gradually decrease to 350.4 G, i.e. about $-40 a_0$, the size of Na decreases; meanwhile, Rb size is almost unchanged. This phenomenon can be understood that Na has absorbed into Rb thanks to the miscible and attractive interaction. When the magnetic field decreases further, a severe loss shows up for both Na and Rb, mainly due to the three-body loss happening when the density gets high. Then when the magnetic field is across 350 G, sizes of both Na and Rb increase sharply upon the magnetic field. Here, we already find this abnormal expansion velocity of the sample. However, the explanation could be either three-body loss(heating) in a droplet sample or just BEC collapsing, which is hard to distinguish them.

With this measurement, we cannot make conclusion that we catch the signal of droplet. Whatever, we spent only two weeks doing the fast test and making the deci-

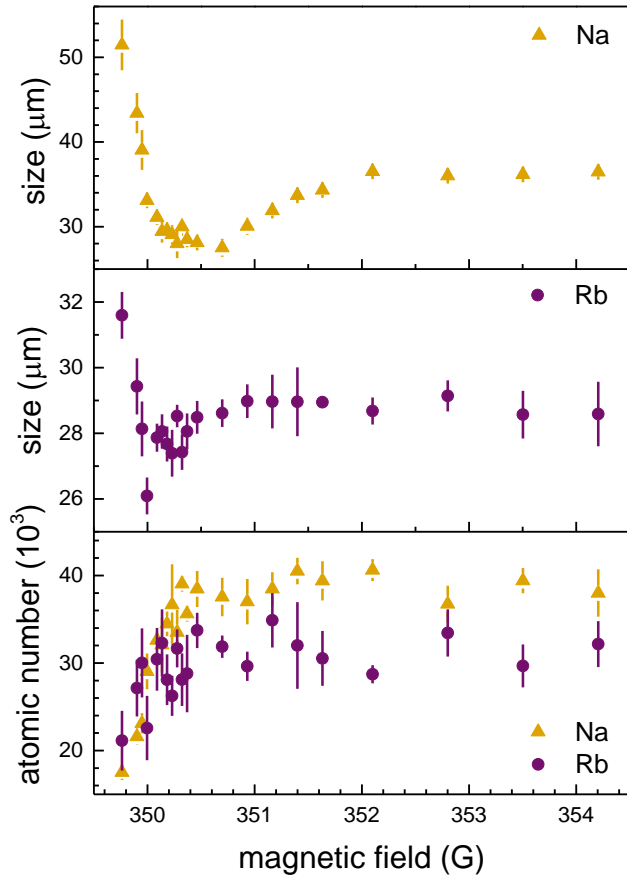


Figure 6.3: This figure shows our try at detecting droplet signals with a low-magnetic field absorption image. With the magnetic field decrease from 352 G to 350 G, we can see an apparent decrease in the size of both Na and Rb. This is thanks to the inter-species attractive interaction. Then, with a further decrease of the magnetic field, we see steep inflation of sample size and severe loss.

sion, which is judicious from the current point of view. Besides the above mentioned reasons, we have to suspect the destructive dynamics of the sample during the ToF when the magnetic field switching down. Because the droplet sample have a density even 10 times larger than a typical BEC sample, we have to treat this ToF process very carefully. So, what we need is a new image method which can directly capture the sample under a high magnetic field (around 350 G). We stop our experiment and try to design a image method working under high magnetic field. First, we want to try the Faraday image. We do the calculation, trying to find the rotation angle for our sample. However the calculation shows that we need an EMCCD to get enough SNR, which is out of our afford. So we turn back to try the absorption image under a high magnetic field. There were two problems: we need to find a cycling (or almost-cycling) transition under 350 G; another is we need to handle the sample with extremely high optical density (OD), around 10 to 50 for the Rb sample. We calculate and conceive all possible image scheme, such as two examples shown in Fig. 6.4. We first try a 90% almost-cycling transition (shown in (a) of Fig. 6.4), then we turn to the other one since even the 10% leakage cause hard calibration of the sample's OD. For another problem, we use the partial transferring [Ramanathan et al., 2012]. We will detailly discuss then in the apparatus chapter (Chap. 3).

In July 2018, We first chose the non-cycling transition with 90% probability back to the original state. With this imaging method on Na, we get the first signal of a droplet. Even though we know it is not a droplet (since the magnetic field is 350.089G, which is higher than the mean-field collapse boundary 349.978 G). We are very close to the collapse bound. However, due to the limited ToF duration and image resolution, we thought that was the droplet. As shown in Fig. 6.5, this deep attractive double BEC already shows its tiny expansion property. Then, we are encouraged and build the Rb high-magnetic-field (HF) image with the beat locking method. We found it hard to use scheme (a) since the high OD cause the sensitivity of the OD we obtain upon the

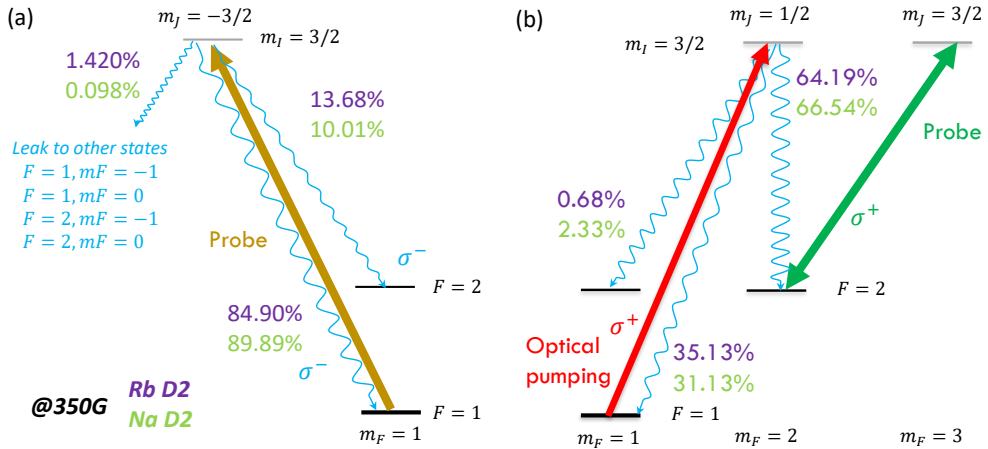


Figure 6.4: (a) non-cycling image scheme for Na(Rb) $|F = 1, m_F = 1\rangle$ state. (b) After partially pumping the $|F = 1, m_F = 1\rangle$ atoms to the cycling transition for $|F = 2, m_F = 2\rangle$ state. The calculation is under 350 G magnetic field.

image duration. So we switch to image scheme (b).

Thanks to images for both species, we discover the magnetic gradient affecting the droplet sample. As shown in Fig. 3.18, the gradient applies on Na and Rb generate different forces due to different mass and dipole. The mixture sample tends to be torn apart. So, for observing a better droplet signal without the effect of a gradient, we compensate the gradient with another single-coil (right panel of Fig. 3.18). By measuring the accelerations of both Rb and Na, we can choose the best compensation point. After solving this problem, we obtain the non-expansion signal of the droplet clearly, as shown in Fig. 6.6. We use an imbalanced number case; the Na number is much larger than Rb. A clear, bright spot shows up at the centre of the Na BEC, which shows the smoking-gun signal for the droplet.

After the detection we made in Fig. 6.6, we find that the image resolution is limited since the original image system with 3x magnification has a resolution of $4 \mu\text{m}$ and pixel corresponding size $2.1 \mu\text{m}$. Both parameters are comparable to the size of the droplet and even larger than it. So, we determined to upgrade our image system.

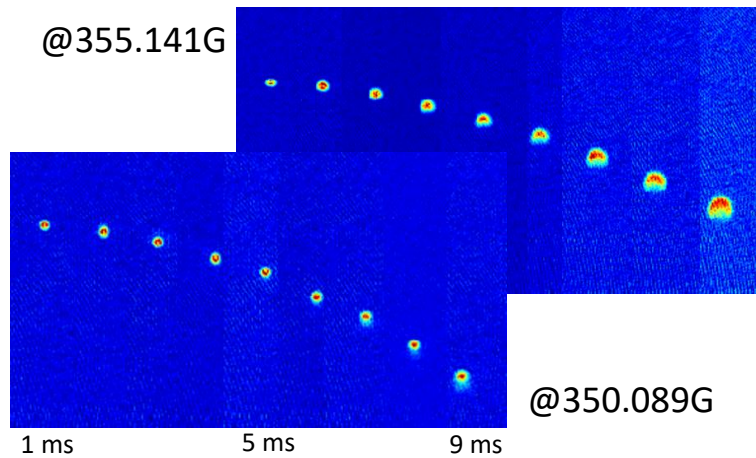


Figure 6.5: Na absorption image with non-cycling scheme. Signal at 350 G show clear size shrinking and shape turning to sphere.

We first choose the set-up of the microscope and the zoom lens system from Navitor. This system offers a magnification changing from 0.8 to 12 times, which is enough for our measurement. Meanwhile, we use a Mitutoyo long-working distance microscope to upgrade the image resolution. After all these upgrades, we achieve a 15x image system with a resolution of around $2 \mu\text{m}$. Details can be found in Sect. 3.5.

In June of 2019, after finishing all the technical problems, we started to take data for the droplet sample. We measured the non-expansion signal and studied the phase diagram. Besides the liquid droplet phase, we also study the gas phase, trying to understand the abnormal expansions. Details can be found in Chap. 5. Then, we meet the big problem that the experimental measurement of the phase diagram has a 300 mG discrepancy compared to the theoretical calculation. Even we do a more careful compensation of the magnetic field and number calibration, the discrepancy is still there. Finally, we doubt the accuracy of our Feshbach resonance parameter, so we re-do the FR calibration [Guo et al., 2021b]. This is an individual story as depicted in Chap. 4.

I summarize the journey of studying quantum droplets as follows: first, the goal

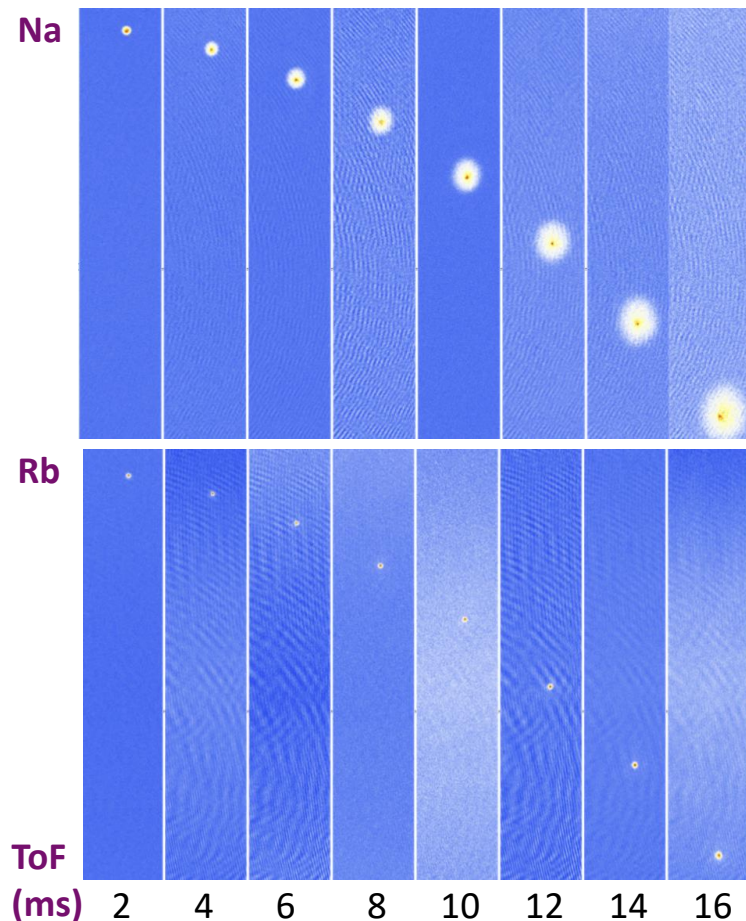


Figure 6.6: Na and Rb droplet signal under 349.826 G. atomic number for Na(Rb) is 9×10^4 (3×10^4). A clear, bright spot shows up inside the BEC surrounding of Na sample.

of this study is passive since we did not figure out what we want to study at the very beginning. A clear goal is vital to guide and push the following movement, such as technique upgrading or numerical simulation. Second, the review work done at the first phase is not broad enough. We only focus on the already existing experimental works and theories. Actually, finding the connection between other fields is essential and could guide the following working direction. Third, my attitude to the *numbers* is not serious that caused using of the unverified parameters. This pulled our leg for a long time and finally causing the degrading of this work. In all, it is a good lesson to not only my research career but also to my daily life, from the attitude to details to the way of thinking and doing.

6.3 Outlooks

The biggest difficulty and problem of our experiment is that it is impossible to obtain a sample with a sufficient and stable lifespan. Because the experiment uses the ToF method, if the atomic group flies too far, both the gradient of the magnetic field and the resolution of the imaging will be further affected, thereby limiting the detection time. The improved scheme can refer to the Italian paper and adopt the method of light well levitation. It should be noted that the trap effect of levitation needs to be evaluated, so as to avoid the unwanted effect of additional traps. Another problem is the excessively high three-body loss rate. Because the density of the droplet is generally much higher than the gaseous BEC, about one to two orders of magnitude. Therefore, the three-body loss rate is higher by 10^2 to 10^3 . For such a serious loss, it can only be achieved by preparing a droplet with a weaker bond to reduce the density of its equilibrium state. The negative effect of this is that the requirements for the number of atoms are correspondingly increased. Our new device uses 2D-MOT to increase the atomic number of Na, which may have the opportunity to prepare quantum droplets with more atomic numbers.

On the existing experimental devices, the experiments we may explore mainly include the study of low-dimensional quantum droplets. Refer to petrov and other papers, for 2D or 1D systems, it is relatively easier to implement droplets, which stems from the fact that the quantum fluctuation of low-dimensional systems is more important than the MF part. For example, the formation conditions of 2D droplets will be more relaxed than 3D. δg does not need to be less than 0, it can also form a droplet phase. In addition, 2D is more abundant, and there are many interesting research content waiting to be discovered.

From the theoretical point of view, Petrov's theory [Petrov, 2015] has a loophole, which was discussed by [Hu and Liu, 2020b; Hu et al., 2020]. As we present in Chap. 2, the integral of the low-momentum imaginary region of the excitation spectrum is ill. This may hide a more profound physics. The problem can be severe when we tune δg to be even negative, finally deviating from the weak attractive MF condition. Then, we must quest the microscope formation mechanism of the quantum droplet. One theory proposes the Bose pairing mechanism, which imitates the BCS theory providing a new field of pair of Boson. For a low dimension system, the Bose-pairing can form naturally. However, for the 3D case, the bound state formation is subtle. How to design an experiment to verify these new theories is essential. For example, for the theory of Bose pairing, it may be possible to use brag spectroscopy to detect the excitation of the pair to verify.

In addition, starting from the already formed droplet, we can also consider its improvement or inspiration for other experiments. For example, droplet leads to a very good overlap of Na Rb. Considering this, we try to use this as a starting point to improve the formation rate of Feshbach molecule. Our experiments show that this effect is not very obvious. In addition to the limitations of experimental methods, theoretically it may be related to a multi-body system such as sample itself is condensate. Then this system can be used as a good platform to detect the transition from few to

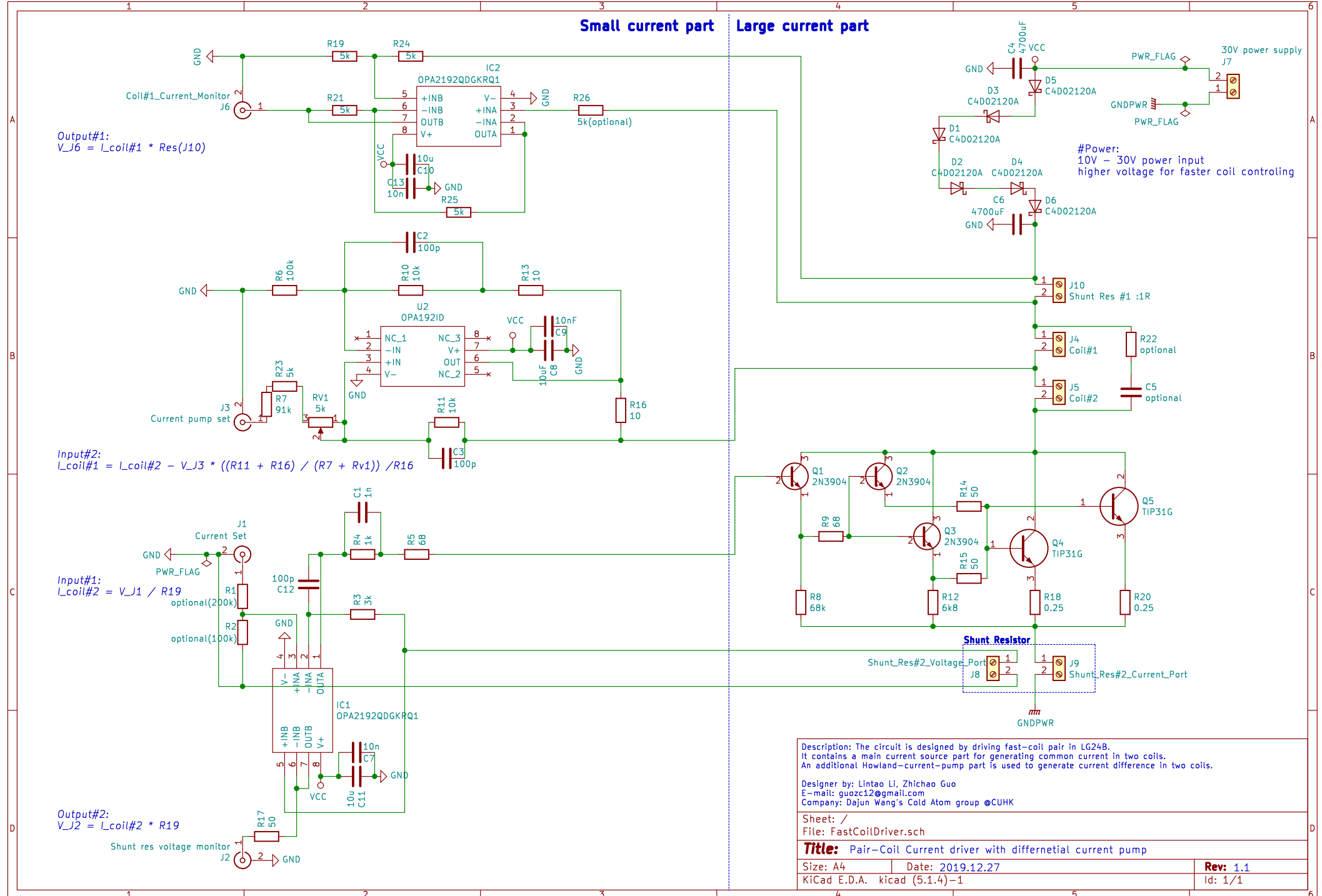
many bodies.

In short, quantum droplet is a small branch that studies many-body physics. Its significance is to raise the status of LHY correction to a dominant position, not just a correction. Compared with the measurement of other previous experiments, this has a very extraordinary significance. Then, for such a new phase, dig out more characteristics, so that it can become a very meaningful platform for in-depth study of pure quantum effect such as LHY or above LHY. The unique cleanliness and easy control of the cold atom experimental system will bring excellent solutions for the study of many-body physics and further quantum simulations.

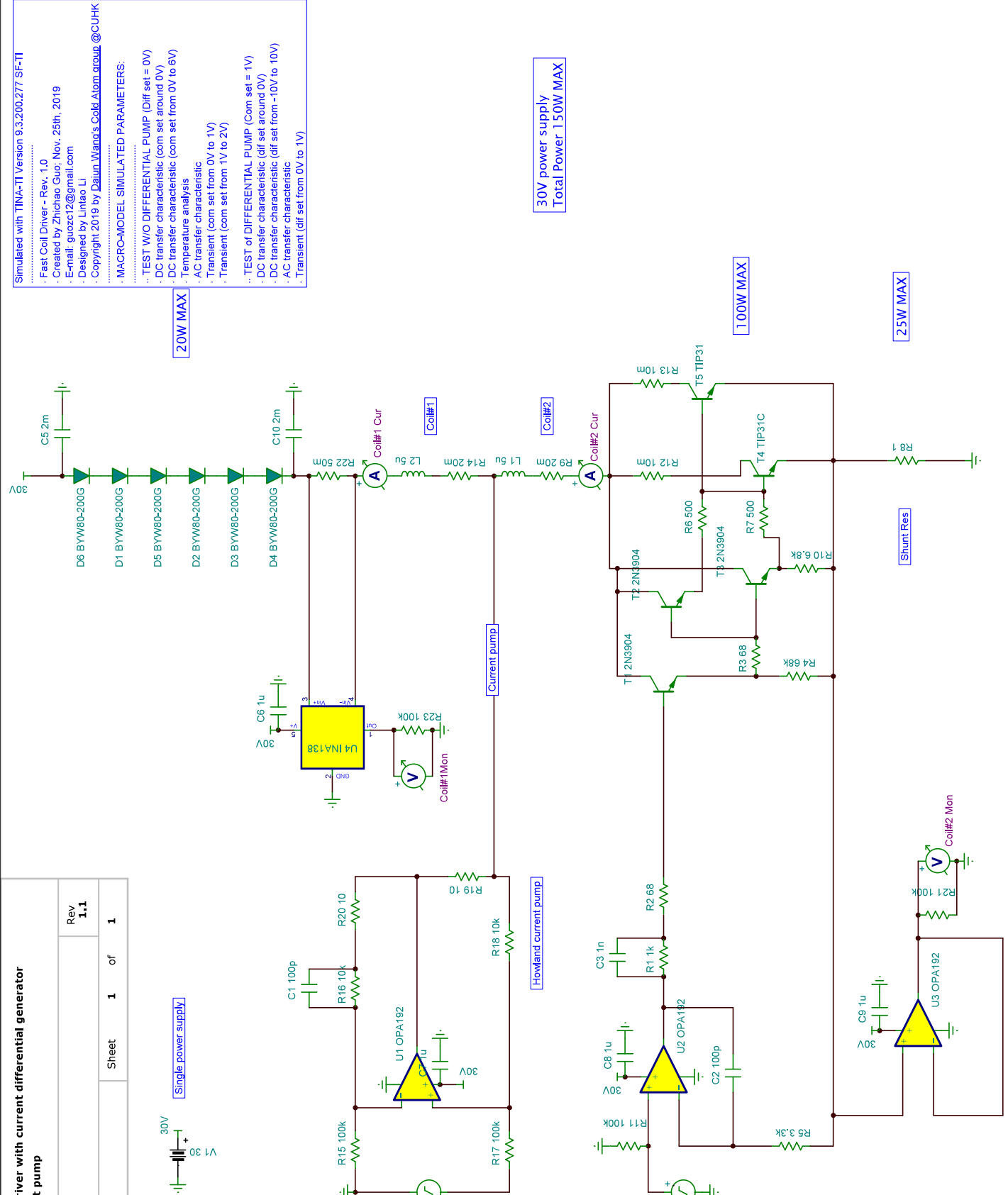
End of chapter.

Appendix A

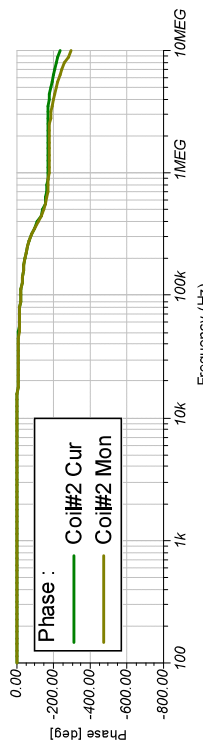
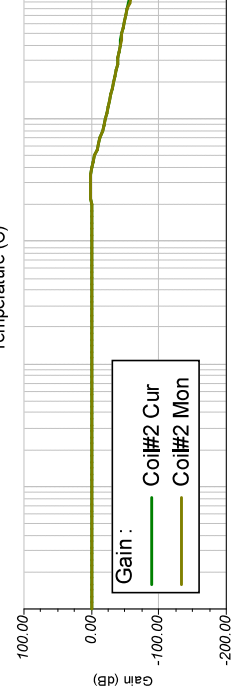
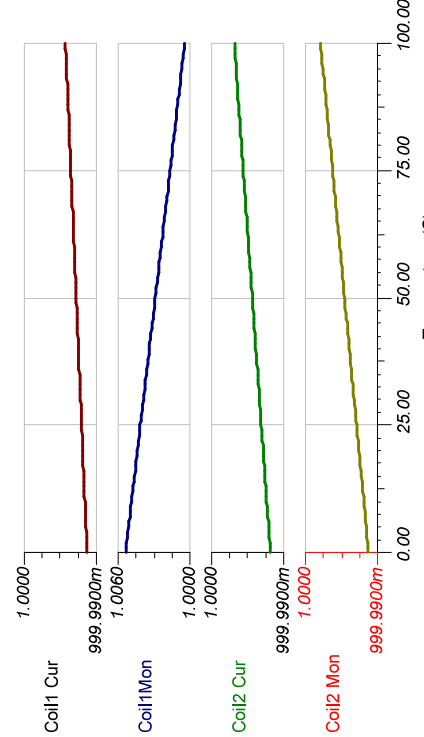
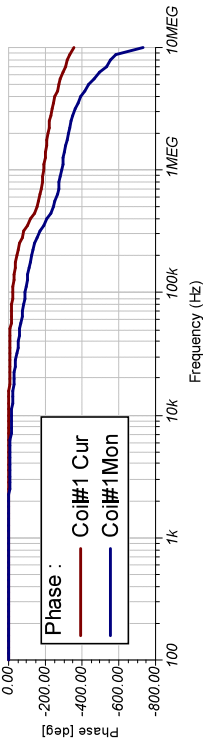
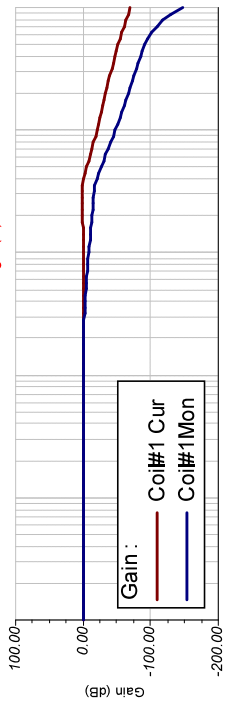
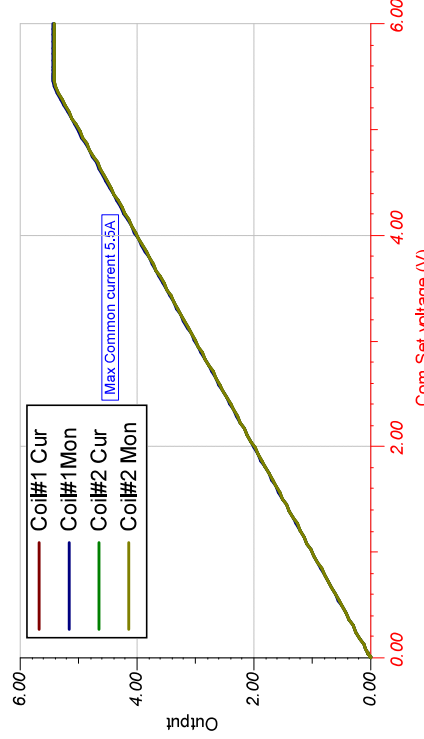
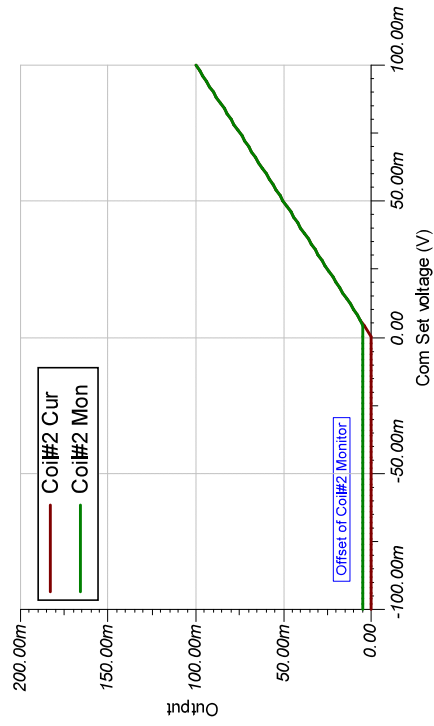
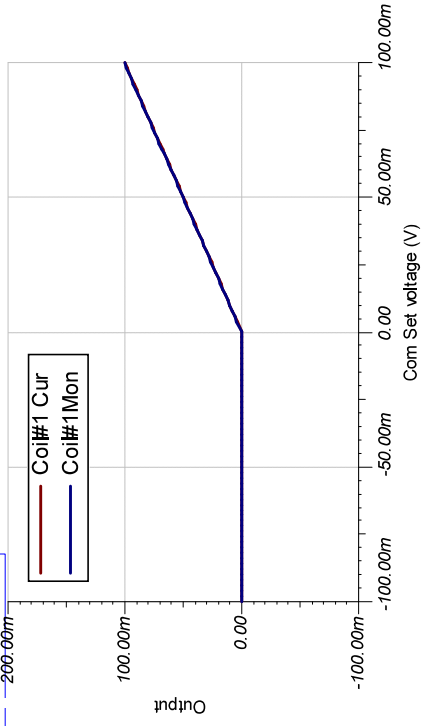
Mechanics and electronics schematic

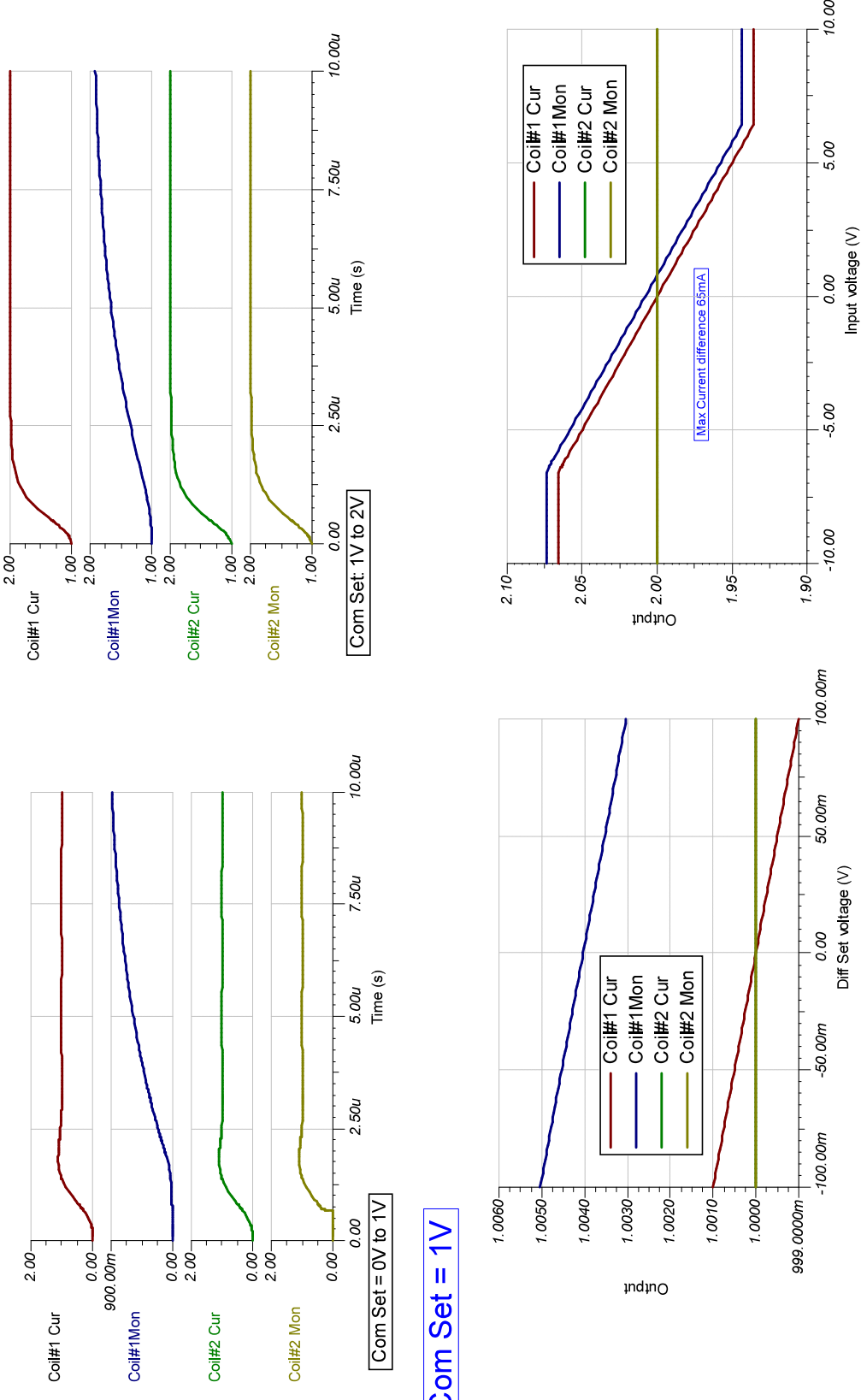


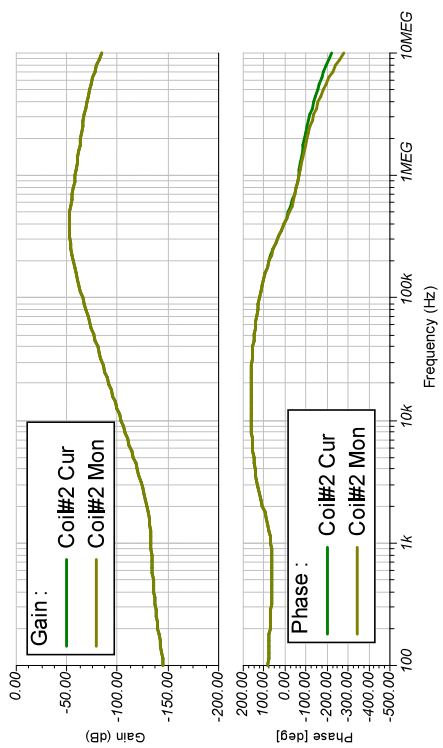
Title	Fast-Coil current driver with current differential generator by Howland current pump		
Size	Document No.	C5001	Rev. 1.1
Date	2019.12.05 Sheet 1 of 1		



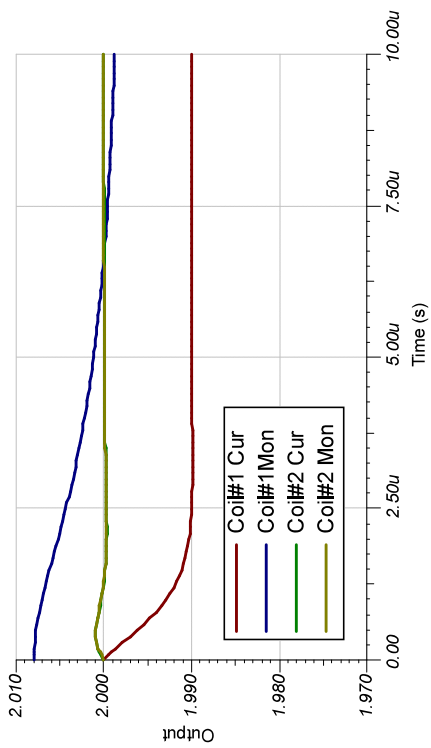
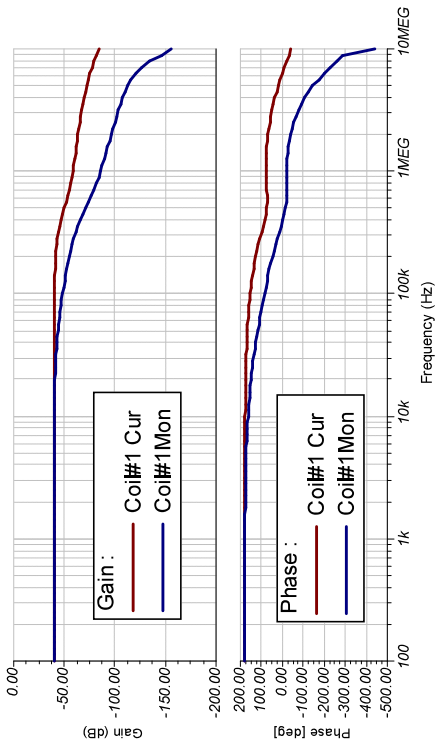
Diff Set = 0V

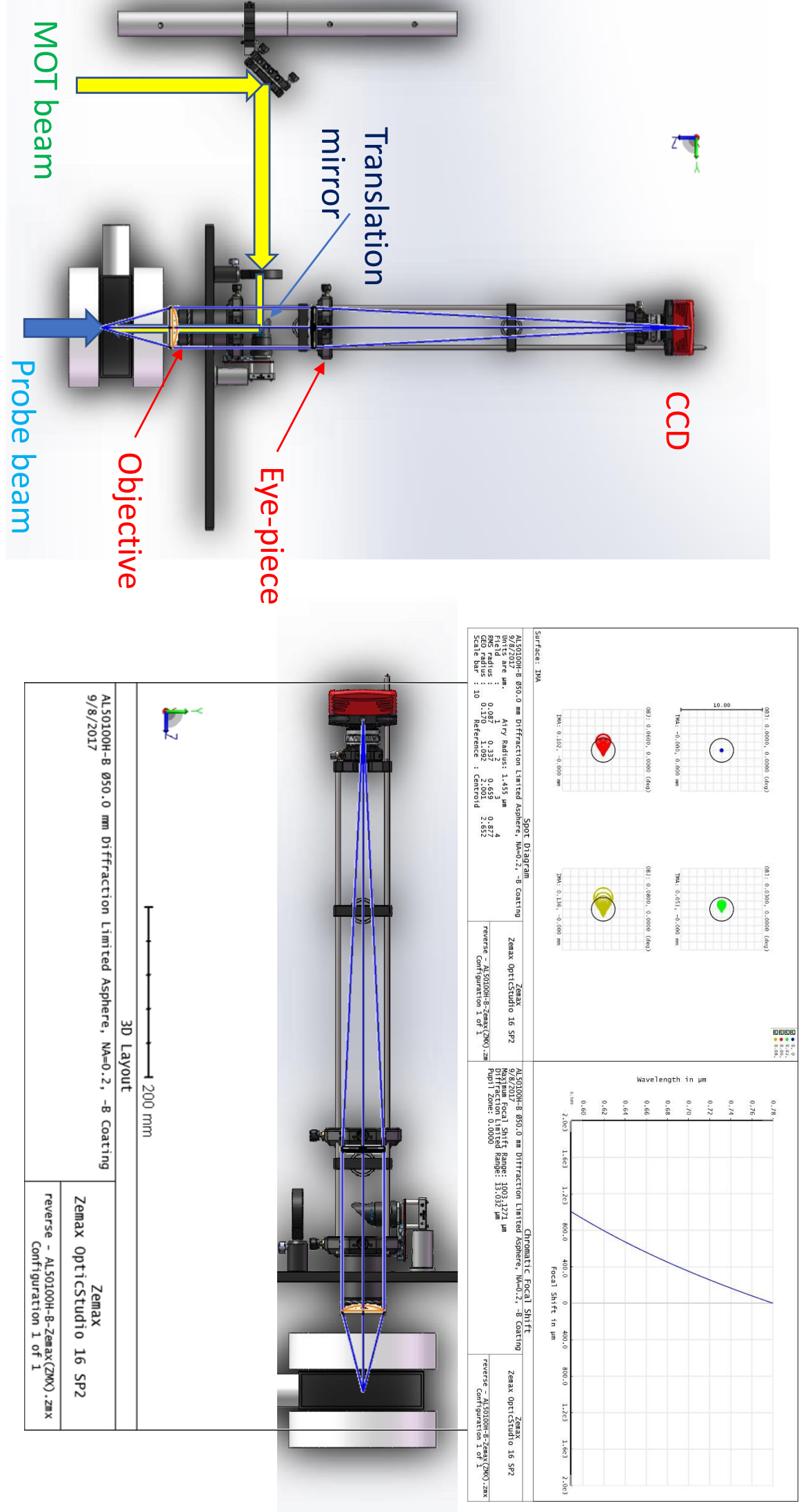






Differential Pump only affect coil#1 current, no changing coil#2 current





Appendix B

Camera comparison and absorption image SNR analysis

B.1 Absorption SNR analysis

When doing absorption image, we typically take three images, noted as:

- $C_{\text{in}}(x, y)$ as input light distribution on the atom
- $C_{\text{out}}(x, y)$ as output(after absorption) light
- $C_{\text{bg}}(x, y)$ as the background

formula of OD is

$$\text{OD}(x, y) = n_{\text{col}}(x, y)\sigma_0^* = \text{Log} \left[\frac{C_{\text{in}}(x, y) - C_{\text{bg}}(x, y)}{C_{\text{out}}(x, y) - C_{\text{bg}}(x, y)} \right] + \frac{C_{\text{in}}(x, y) - C_{\text{out}}(x, y)}{C_{\text{sat}}^{\text{eff}}} \quad (\text{B.1})$$

where

- $C(x, y) = I(x, y) \times \frac{A_{\text{pix}}}{M^2} \times \frac{\lambda}{hc} \times T \times \text{QE} \times \tau \times \frac{1}{\text{ADC}}$
- $I(x, y)$ is the intensity distribution of light on atom
- A_{pix} is the pixel size of camera, $\frac{A_{\text{pix}}}{M^2}$ is the real pixel size with counting magnification of image system.
- λ is the probe light wavelength
- T is the transmission rate of the image system
- QE is the quantum efficiency of the camera

- ADC is the ADC conversion efficiency of the camera
- τ is the exposure time

The Noise is

$$\begin{aligned}\sigma_{OD}^2 &= \left(\frac{\partial OD}{\partial C_{in}} \right)^2 \sigma_{C_{in}}^2 + \left(\frac{\partial OD}{\partial C_{out}} \right)^2 \sigma_{C_{out}}^2 + \left(\frac{\partial OD}{\partial C_{bg}} \right)^2 \sigma_{C_{bg}}^2 \\ &= \left(\frac{1}{C_{sat}^{eff}} + \frac{1}{C_{in} - C_{bg}} \right)^2 \sigma_{C_{in}}^2 + \left(\frac{1}{C_{sat}^{eff}} + \frac{1}{C_{out} - C_{bg}} \right)^2 \sigma_{C_{out}}^2 \\ &\quad + \left(\frac{1}{C_{in} - C_{bg}} - \frac{1}{C_{out} - C_{bg}} \right)^2 \sigma_{C_{bg}}^2\end{aligned}\quad (B.2)$$

Then, The Signal to Noise ratio is

$$\begin{aligned}SNR &= \frac{\text{Log} \left[\frac{C_{in} - C_{bg}}{C_{out} - C_{bg}} \right] + \frac{C_{in} - C_{out}}{C_{sat}^{eff}}}{\sqrt{\alpha^2 + \beta^2 + \gamma^2}} \\ \alpha^2 &= \left(\frac{1}{C_{sat}^{eff}} + \frac{1}{C_{in} - C_{bg}} \right)^2 \sigma_{C_{in}}^2 \\ \beta^2 &= \left(\frac{1}{C_{sat}^{eff}} + \frac{1}{C_{out} - C_{bg}} \right)^2 \sigma_{C_{out}}^2 \\ \gamma^2 &= \left(\frac{1}{C_{in} - C_{bg}} - \frac{1}{C_{out} - C_{bg}} \right)^2 \sigma_{C_{bg}}^2\end{aligned}\quad (B.3)$$

Put noise formula into the above SNR, we have

$$\begin{aligned}
\text{SNR} &= \frac{\text{Log} \left[\frac{C_{\text{in}} - C_{\text{bg}}}{C_{\text{out}} - C_{\text{bg}}} \right] + \frac{C_{\text{in}} - C_{\text{out}}}{C_{\text{sat}}^{\text{eff}}}}{\sqrt{X^2 + Y^2 + Z^2 + W^2}} \\
X^2 &= \left[\left(\frac{1}{C_{\text{sat}}^{\text{eff}}} + \frac{1}{C_{\text{in}} - C_{\text{bg}}} \right)^2 + \left(\frac{1}{C_{\text{sat}}^{\text{eff}}} + \frac{1}{C_{\text{out}} - C_{\text{bg}}} \right)^2 \right. \\
&\quad \left. + \left(\frac{1}{C_{\text{in}} - C_{\text{bg}}} - \frac{1}{C_{\text{out}} - C_{\text{bg}}} \right)^2 \right] \sigma_{\text{readout}}^2 \\
Y^2 &= \left(\frac{1}{C_{\text{sat}}^{\text{eff}}} + \frac{1}{C_{\text{in}} - C_{\text{bg}}} \right)^2 \sigma_{\text{in-signal}}^2 \\
Z^2 &= \left(\frac{1}{C_{\text{sat}}^{\text{eff}}} + \frac{1}{C_{\text{out}} - C_{\text{bg}}} \right)^2 \sigma_{\text{out-signal}}^2 \\
W^2 &= \left(\frac{1}{C_{\text{in}} - C_{\text{bg}}} - \frac{1}{C_{\text{out}} - C_{\text{bg}}} \right)^2 \sigma_{\text{bg-signal}}^2
\end{aligned} \tag{B.4}$$

Table B.1: Camera parameter table

	PCO-Pixelfly	GS3-U3-15S5M-C	BFS-PGE-31S4	PCO-sCOS
Wavelength(nm)	589/780	589/780	589/780	589/780
QE(%) on datasheet	58/25	72/35	70/30	61/35
QE(%) measured	-/22.0	56.6/-	47.2/27.0	
Readout noise(e) on datasheet	6	8.31	2.29	1.1
Readout noise(e) measured			0.53	
Dark noise rate on datasheet	1 e/s			0.8 e/s
Dark noise rate measured			0.59 e/s	
A/D conversion(e/count) on datasheet	1	tunable	tunable	0.46
A/D conversion(e/count) measured			1/0.53	

Bibliography

- Antoine, X. and Duboscq, R. (2014). Gpelab, a matlab toolbox to solve gross-pitaevskii equations i: Computation of stationary solutions. *Computer Physics Communications*, 185(11):2969–2991.
- Bartenstein, M., Altmeyer, A., Riedl, S., Geursen, R., Jochim, S., Chin, C., Denschlag, J. H., Grimm, R., Simoni, A., Tiesinga, E., Williams, C. J., and Julienne, P. S. (2005). Precise determination of ${}^6\text{Li}$ cold collision parameters by radio-frequency spectroscopy on weakly bound molecules. *Phys. Rev. Lett.*, 94:103201.
- Bartenstein, M., Altmeyer, A., Riedl, S., Jochim, S., Chin, C., Denschlag, J. H., and Grimm, R. (2004). Collective excitations of a degenerate gas at the bcs-bcs crossover. *Phys. Rev. Lett.*, 92:203201.
- Berninger, M., Zenesini, A., Huang, B., Harm, W., Nägerl, H.-C., Ferlaino, F., Grimm, R., Julienne, P. S., and Hutson, J. M. (2013). Feshbach resonances, weakly bound molecular states and coupled-channel potentials for cesium at high magnetic field. *Phys. Rev. A*, 87:032517.
- Bourdel, T., Khaykovich, L., Cubizolles, J., Zhang, J., Chevy, F., Teichmann, M., Tarruell, L., Kokkelmans, S. J. J. M. F., and Salomon, C. (2004). Experimental study of the bcs-bcs crossover region in lithium 6. *Phys. Rev. Lett.*, 93:050401.
- Cabrera, C. R., Tanzi, L., Sanz, J., Naylor, B., Thomas, P., Cheiney, P., and Tarruell, L. (2018). Quantum liquid droplets in a mixture of bose-einstein condensates. *Science*, 359(6373):301–304.
- Chapurin, R., Xie, X., Van de Graaff, M. J., Popowski, J. S., D’Incao, J. P., Julienne, P. S., Ye, J., and Cornell, E. A. (2019). Precision test of the limits to universality in few-body physics. *Phys. Rev. Lett.*, 123:233402.
- Cheiney, P., Cabrera, C. R., Sanz, J., Naylor, B., Tanzi, L., and Tarruell, L. (2018). Bright soliton to quantum droplet transition in a mixture of bose-einstein condensates. *Phys. Rev. Lett.*, 120:135301.

- Cheung, S. N.-S. (1988). 卖桔者言. 走向未來叢書. Sichuan People's Publishing House.
- Chin, C., Grimm, R., Julienne, P., and Tiesinga, E. (2010). Feshbach resonances in ultracold gases. *Rev. Mod. Phys.*, 82:1225–1286.
- Chin, C. and Julienne, P. S. (2005). Radio-frequency transitions on weakly bound ultracold molecules. *Phys. Rev. A*, 71:012713.
- Chomaz, L., Baier, S., Petter, D., Mark, M. J., Wächtler, F., Santos, L., and Ferlaino, F. (2016). Quantum-fluctuation-driven crossover from a dilute bose-einstein condensate to a macrodroplet in a dipolar quantum fluid. *Phys. Rev. X*, 6:041039.
- Claussen, N. R., Kokkelmans, S. J. J. M. F., Thompson, S. T., Donley, E. A., Hodby, E., and Wieman, C. E. (2003). Very-high-precision bound-state spectroscopy near a ^{85}Rb feshbach resonance. *Phys. Rev. A*, 67:060701.
- Cowan, B. (2005). *Topics in Statistical Mechanics*. PUBLISHED BY IMPERIAL COLLEGE PRESS AND DISTRIBUTED BY WORLD SCIENTIFIC PUBLISHING CO.
- Cui, X. and Ma, Y. (2021). Droplet under confinement: Competition and coexistence with a soliton bound state. *Phys. Rev. Research*, 3:L012027.
- Cui, Y., Deng, M., You, L., Gao, B., and Tey, M. K. (2018). Broad feshbach resonances in ultracold alkali-metal systems. *Phys. Rev. A*, 98:042708.
- Cumby, T. D. (2012). *Exploring few-body scattering resonances in a Bose-Fermi mixture: from Feshbach dimers to Efimov trimers*. PhD thesis, University of Colorado at Boulder.
- D'Errico, C., Burchianti, A., Prevedelli, M., Salasnich, L., Ancilotto, F., Modugno, M., Minardi, F., and Fort, C. (2019). Observation of quantum droplets in a heteronuclear bosonic mixture. *Phys. Rev. Research*, 1:033155.
- Donley, E. A., Claussen, N. R., Cornish, S. L., Roberts, J. L., Cornell, E. A., and Wieman, C. E. (2001). Dynamics of collapsing and exploding bose-einstein condensates. *Nature*, 412(6844):295–299.
- Ferioli, G., Semeghini, G., Terradas-Briansó, S., Masi, L., Fattori, M., and Modugno, M. (2020). Dynamical formation of quantum droplets in a ^{39}K mixture. *Phys. Rev. Research*, 2:013269.
- Ferrier-Barbut, I., Kadau, H., Schmitt, M., Wenzel, M., and Pfau, T. (2016a). Observation of quantum droplets in a strongly dipolar bose gas. *Phys. Rev. Lett.*, 116:215301.

- Ferrier-Barbut, I., Schmitt, M., Wenzel, M., Kadau, H., and Pfau, T. (2016b). Liquid quantum droplets of ultracold magnetic atoms. *Journal of Physics B: Atomic, Molecular and Optical Physics*, 49(21):214004.
- Frye, M. D. and Hutson, J. M. (2017). Characterizing feshbach resonances in ultracold scattering calculations. *Phys. Rev. A*, 96:042705.
- Gribakin, G. F. and Flambaum, V. V. (1993). Calculation of the scattering length in atomic collisions using the semiclassical approximation. *Phys. Rev. A*, 48:546–553.
- Guo, M., Vexiau, R., Zhu, B., Lu, B., Bouloufa-Maafa, N., Dulieu, O., and Wang, D. (2017). High-resolution molecular spectroscopy for producing ultracold absolute-ground-state $^{23}\text{Na}^{87}\text{Rb}$ molecules. *Phys. Rev. A*, 96:052505.
- Guo, M., Zhu, B., Lu, B., Ye, X., Wang, F., Vexiau, R., Bouloufa-Maafa, N., Quéméner, G., Dulieu, O., and Wang, D. (2016). Creation of an ultracold gas of ground-state dipolar $^{23}\text{Na}^{87}\text{Rb}$ molecules. *Phys. Rev. Lett.*, 116:205303.
- Guo, Z. (2021). **Signal-to-Noise Ratio in Absorption Imaging**.
- Guo, Z., Jia, F., Li, L., Ma, Y., Hutson, J. M., Cui, X., and Wang, D. (2021a). Lee-huang-yang effects in the ultracold mixture of ^{23}na and ^{87}rb with attractive interspecies interactions.
- Guo, Z., Jia, F., Zhu, B., Li, L., Hutson, J. M., and Wang, D. (2021b). Tunable feshbach resonances and interaction potentials between ^{23}na and ^{87}rb atoms.
- Holland, M. J., Jin, D. S., Chiofalo, M. L., and Cooper, J. (1997). Emergence of interaction effects in bose-einstein condensation. *Phys. Rev. Lett.*, 78:3801–3805.
- Hu, H. and Liu, X.-J. (2020a). Collective excitations of a spherical ultradilute quantum droplet. *Phys. Rev. A*, 102:053303.
- Hu, H. and Liu, X.-J. (2020b). Consistent Theory of Self-Bound Quantum Droplets with Bosonic Pairing. *Phys. Rev. Lett.*, 125:195302.
- Hu, H., Wang, J., and Liu, X.-J. (2020). Microscopic pairing theory of a binary Bose mixture with interspecies attractions: Bosonic BEC-BCS crossover and ultradilute low-dimensional quantum droplets. *Phys. Rev. A*, 102:043301.
- Huang, R. (1981). *1587, a year of no significance : the Ming dynasty in decline*. Yale University Press, New Haven.
- Hueck, K., Luick, N., Sobirey, L., Siegl, J., Lompe, T., Moritz, H., Clark, L. W., and Chin, C. (2017). Calibrating high intensity absorption imaging of ultracold atoms. *Opt. Express*, 25(8):8670–8679.

- Hung, C.-L. (2011). *In situ probing of two-dimensional quantum gases*. The University of Chicago.
- Hutson, J. M. (2007). Feshbach resonances in ultracold atomic and molecular collisions: threshold behaviour and suppression of poles in scattering lengths. *New J. Phys.*, 9(5):152–152.
- Hutson, J. M. and Le Sueur, C. R. (2019). molscat: A program for non-reactive quantum scattering calculations on atomic and molecular collisions. *Computer Physics Communications*, 241:9–18.
- Hutson, J. M. and Le Sueur, C. R. (2020). MOLSCAT, BOUND and FIELD, version 2020.0. <https://github.com/molscat/molscat>.
- Ilg, T., Kumlin, J., Santos, L., Petrov, D. S., and Büchler, H. P. (2018). Dimensional crossover for the beyond-mean-field correction in bose gases. *Phys. Rev. A*, 98:051604.
- Jia, F., Guo, Z., Li, L., and Wang, D. (2020). Detection of narb feshbach molecules by photodissociation. *Phys. Rev. A*, 102:043327.
- Jørgensen, N. B., Bruun, G. M., and Arlt, J. J. (2018). Dilute fluid governed by quantum fluctuations. *Phys. Rev. Lett.*, 121:173403.
- Khaykovich, L., Schreck, F., Ferrari, G., Bourdel, T., Cubizolles, J., Carr, L. D., Castin, Y., and Salomon, C. (2002). Formation of a matter-wave bright soliton. *Science*, 296(5571):1290–1293.
- Knoop, S., Schuster, T., Scelle, R., Trautmann, A., Appmeier, J., Oberthaler, M. K., Tiesinga, E., and Tiemann, E. (2011). Feshbach spectroscopy and analysis of the interaction potentials of ultracold sodium. *Phys. Rev. A*, 83:042704.
- Köhler, T., Góral, K., and Julienne, P. S. (2006). Production of cold molecules via magnetically tunable feshbach resonances. *Rev. Mod. Phys.*, 78:1311–1361.
- Lange, A. D., Pilch, K., Prantner, A., Ferlaino, F., Engeser, B., Nägerl, H.-C., Grimm, R., and Chin, C. (2009). Determination of atomic scattering lengths from measurements of molecular binding energies near feshbach resonances. *Phys. Rev. A*, 79:013622.
- Lee, T. D. (1992). History of weak interactions. In *Summer School on Quantitative Particle Physics*.

- Lee, T. D., Huang, K., and Yang, C. N. (1957). Eigenvalues and eigenfunctions of a bose system of hard spheres and its low-temperature properties. *Phys. Rev.*, 106:1135–1145.
- Li, L. (2021). Bose polarons and tunable spin dynamics in an ultracold mixture of ^{87}rb and ^{23}na atoms.
- Li, X. (2015). Coherent heteronuclear spin dynamics in an ultracold spinor mixture.
- Ma, Y., Peng, C., and Cui, X. (2021). Borromean droplet in three-component ultracold bose gases. *Phys. Rev. Lett.*, 127:043002.
- Mewes, M.-O., Andrews, M. R., van Druten, N. J., Kurn, D. M., Durfee, D. S., and Ketterle, W. (1996). Bose-einstein condensation in a tightly confining dc magnetic trap. *Phys. Rev. Lett.*, 77:416–419.
- Minardi, F., Ancilotto, F., Burchianti, A., D'Errico, C., Fort, C., and Modugno, M. (2019). Effective expression of the lee-huang-yang energy functional for heteronuclear mixtures. *Phys. Rev. A*, 100:063636.
- Mohapatra, A. and Braaten, E. (2015). Harmonic and subharmonic association of universal dimers in a thermal gas. *Phys. Rev. A*, 92:013425.
- Molony, P. K., Gregory, P. D., Ji, Z., Lu, B., Köppinger, M. P., Le Sueur, C. R., Blackley, C. L., Hutson, J. M., and Cornish, S. L. (2014). Creation of ultracold $^{87}\text{Rb}^{133}\text{Cs}$ molecules in the rovibrational ground state. *Phys. Rev. Lett.*, 113:255301.
- Navon, N., Piatecki, S., Günter, K., Rem, B., Nguyen, T. C., Chevy, F., Krauth, W., and Salomon, C. (2011). Dynamics and thermodynamics of the low-temperature strongly interacting bose gas. *Phys. Rev. Lett.*, 107:135301.
- Ni, K.-K., Ospelkaus, S., de Miranda, M. H. G., Pe'er, A., Neyenhuis, B., Zirbel, J. J., Kotochigova, S., Julienne, P. S., Jin, D. S., and Ye, J. (2008). A high phase-space-density gas of polar molecules. *Science*, 322(5899):231–235.
- Park, J. W., Will, S. A., and Zwierlein, M. W. (2015). Ultracold dipolar gas of fermionic $^{23}\text{Na}^{40}\text{K}$ molecules in their absolute ground state. *Phys. Rev. Lett.*, 114:205302.
- Pashov, A., Docenko, O., Tamanis, M., Ferber, R., Knöckel, H., and Tiemann, E. (2005). Potentials for modeling cold collisions between na (3s) and rb (5s) atoms. *Phys. Rev. A*, 72:062505.
- Petrov, D. and Astrakharchik, G. (2016). Ultradilute low-dimensional liquids. *Physical review letters*, 117(10):100401.

- Petrov, D. S. (2015). Quantum mechanical stabilization of a collapsing bose-bose mixture. *Phys. Rev. Lett.*, 115:155302.
- Ramanathan, A., Muniz, S. R., Wright, K. C., Anderson, R. P., Phillips, W. D., Helmerson, K., and Campbell, G. K. (2012). Partial-transfer absorption imaging: A versatile technique for optimal imaging of ultracold gases. *Rev. Sci. Instrum.*, 83(8):083119.
- Regal, C. A., Greiner, M., and Jin, D. S. (2004). Observation of resonance condensation of fermionic atom pairs. *Phys. Rev. Lett.*, 92:040403.
- Reinaudi, G., Lahaye, T., Wang, Z., and Guéry-Odelin, D. (2007). Strong saturation absorption imaging of dense clouds of ultracold atoms. *Opt. Lett.*, 32(21):3143–3145.
- Semeghini, G., Ferioli, G., Masi, L., Mazzinghi, C., Wolswijk, L., Minardi, F., Modugno, M., Modugno, G., Inguscio, M., and Fattori, M. (2018). Self-bound quantum droplets of atomic mixtures in free space. *Phys. Rev. Lett.*, 120:235301.
- Skov, T. G., Skou, M. G., Jørgensen, N. B., and Arlt, J. J. (2021). Observation of a lee-huang-yang fluid. *Phys. Rev. Lett.*, 126:230404.
- Strecker, K. E., Partridge, G. B., Truscott, A. G., and Hulet, R. G. (2002). Formation and propagation of matter-wave soliton trains. *Nature*, 417(6885):150–153.
- Takekoshi, T., Reichsöllner, L., Schindewolf, A., Hutson, J. M., Le Sueur, C. R., Dulieu, O., Ferlaino, F., Grimm, R., and Nägerl, H.-C. (2014). Ultracold dense samples of dipolar rbcs molecules in the rovibrational and hyperfine ground state. *Phys. Rev. Lett.*, 113:205301.
- Thompson, S. T., Hodby, E., and Wieman, C. E. (2005). Ultracold molecule production via a resonant oscillating magnetic field. *Phys. Rev. Lett.*, 95:190404.
- Thomson, W. (2011). *ELECTRICAL UNITS OF MEASUREMENT*, volume 1 of *Cambridge Library Collection - Physical Sciences*, page 73–136. Cambridge University Press.
- van Kempen, E. G. M., Kokkelmans, S. J. J. M. F., Heinzen, D. J., and Verhaar, B. J. (2002). Interisotope determination of ultracold rubidium interactions from three high-precision experiments. *Phys. Rev. Lett.*, 88:093201.
- Voges, K. K., Gersema, P., Meyer zum Alten Borgloh, M., Schulze, T. A., Hartmann, T., Zenesini, A., and Ospelkaus, S. (2020). Ultracold gas of bosonic $^{23}\text{Na}^{39}\text{K}$ ground-state molecules. *Phys. Rev. Lett.*, 125:083401.
- Wang, F. (2016). Studies of an ultracold bose-bose mixture with tunable interspecies interactions.

- Wang, F., He, X., Li, X., Zhu, B., Chen, J., and Wang, D. (2015a). Formation of ultracold NaRb feshbach molecules. *New Journal of Physics*, 17(3):035003.
- Wang, F., Li, X., Xiong, D., and Wang, D. (2015b). A double species ^{23}Na and ^{87}Rb Bose-Einstein condensate with tunable miscibility via an interspecies feshbach resonance. *Journal of Physics B: Atomic, Molecular and Optical Physics*, 49(1):015302.
- Wang, F., Xiong, D., Li, X., Wang, D., and Tiemann, E. (2013). Observation of feshbach resonances between ultracold na and rb atoms. *Phys. Rev. A*, 87:050702.
- Wang, F., Ye, X., Guo, M., Blume, D., and Wang, D. (2019). Observation of resonant scattering between ultracold heteronuclear feshbach molecules. *Phys. Rev. A*, 100:042706.
- Xiong, D., Wang, F., Li, X., Lam, T.-F., and Wang, D. (2013). Production of a rubidium bose-einstein condensate in a hybrid trap with light induced atom desorption.
- Zürn, G., Lompe, T., Wenz, A. N., Jochim, S., Julienne, P. S., and Hutson, J. M. (2013). Precise characterization of ^6Li feshbach resonances using trap-sideband-resolved rf spectroscopy of weakly bound molecules. *Phys. Rev. Lett.*, 110:135301.
- Zwierlein, M. W., Stan, C. A., Schunck, C. H., Raupach, S. M. F., Kerman, A. J., and Ketterle, W. (2004). Condensation of pairs of fermionic atoms near a feshbach resonance. *Phys. Rev. Lett.*, 92:120403.